Tampere University

MARCELO RIZZO PITON

Development of Semiconductor Nanowire Materials for Electronic and Photonics Applications

Tampere University Dissertations 189

Tampere University Dissertations 189

MARCELO RIZZO PITON

Development of Semiconductor Nanowire Materials for Electronic and Photonics Applications

ACADEMIC DISSERTATION
To be presented, with the permission of
the Faculty of Engineering and Natural Sciences
of Tampere University, Finland
and the Center of Exact Sciences and Technology
of Federal University of São Carlos, Brazil
for public discussion in the Swieca Room
of the Physics Department Building,
at Federal University of São Carlos, Rodovia Washington Luís, s/n,
São Carlos-SP, Brazil
on 5th of December 2019, at 10 o'clock.

ACADEMIC DISSERTATION
Tampere University, Faculty of Engineering and Natural Sciences, Finland
Federal University of São Carlos, Center of Exact Sciences and Technology, Brazil

Responsible supervisors	Associate Professor Yara Galvão Gobato Federal University of São Carlos Brazil	Professor Mircea Guina Tampere University Finland
Supervisors	Senior Research Fellow Teemu Hakkarainen Tampere University Finland	D.Sc. (Tech) Soile Talmila Modulight Finland
	Professor Helder V. A. Galeti Federal University of São Carlos Brazil	
Pre-examiners	Senior Technologist Giorgio Biasiol Italian National Research Council Italy	Professor Erkki Lähderanta LUT University Finland
Examination committee	Professor Mohamed Henini University of Nottingham United Kingdom	Associate Professor Iouri Poussep University of São Paulo Brazil
	Researcher Luís Barêa Federal University of São Carlos Brazil	Adjunct Professor Fábio Aparecido Ferri Federal University of São Carlos Brazil
	Associate Professor Yara Galvão Gobato Federal University of São Carlos Brazil	Professor Mircea Guina Tampere University Finland

The originality of this thesis has been checked using the Turnitin OriginalityCheck service.

Cover design: Roihu Inc.

ISBN 978-952-03-1382-1 (print)
ISBN 978-952-03-1383-8 (pdf)
ISSN 2489-9860 (print)
ISSN 2490-0028 (pdf)
http://urn.fi/URN:ISBN:978-952-03-1383-8

PunaMusta Oy – Yliopistopaino
Tampere 2019

To my family: Elza, Osvaldo and Gabriela

ACKNOWLEDGEMENTS

Firstly, I express my gratitude to Prof. Dra. Yara G. Gobato for taking me in as doctoral student that was looking for a new adventure in the vast and interesting world of semiconducting materials. All the opportunities, teachings and counseling were without any doubt crucial for reaching this point where I stand. Little I knew at the time that returning to my beloved UFSCar for doctoral studies would open so many doors for me.

I am very grateful to Prof. Mircea Guina for accepting me initially as an exchange student at ORC research group in Tampere University and later as a doctoral student on a double-degree agreement between UFSCar and TUNI. To be involved in a high level research center was immeasurably valuable for my education and research skills acquired during my doctoral studies. My huge thanks to Dr. Teemu Hakkarainen to all the friendship, counseling and countless teachings during doctoral studies. Also part of our glorious nanowire team from ORC, I thank Eero Koivusalo for providing excellent nanowire samples, high-precision wafer cleaving and all the diverse tasks that we performed. I also thank Dr. Soile Talmila for all the early teachings and guidance during my learning process of nanowires processing. In general, I am very grateful for the complete work environment that was presented for me at ORC. I had a great and friendly working experience where I could discuss my current research issues with experts from different areas.

I also show my thanks to my co-supervisor Prof. Dr. Helder V. A. Galeti for all the patience and instructions during measurements, for taking great care of great part of the TEM imaging and always keeping everything calm. I thank all members from G.O.M.A. in UFSCar for the friendship and help during the endless struggles with properly aligning the optical components of the photoluminesnce setup and creating crazy designs for new laboratory equipment to be made by the physics department staff. I greatly acknowledge and thank all the collaborations partners that were of great importance for the results and publications that were a result of this thesis work. My special thanks for Prof. Dr. Ariano D. G. Rodrigues from the Physics Department at UFSCar for all the discussions and teachings regarding Raman spectroscopy of semiconductor materials in general and also for nanowires. Also my thanks for Dr. Turkka Salminen for the Microscopy Center at TUNI for the training

and support for SEM and Raman microscope. My humble appreciation for the technical and cleanroom staff from TUNI for keeping everything running smoothly: Ilkka, Mervi, Mariia, Pena and Jarno.

I acknowledge the research funding agencies from Brazil, CAPES and FAPESP, for the scholarship and exchange program funding during my doctoral studies. I also acknowledge the financial support from the Academy of Finland Project NESP and NanoLight for partially funding my research in Finland. Finally, I acknowledge the financial support from the Finnish Foundation for Technology Promotion (TES).

Now for the reader that had the curiosity to read the next page of this acknowledgements section, it comes the time for me to thank all my colleagues and friends that were directly or indirectly involved during my life as doctoral student. My cheers to all my great friends in São Carlos and all the mid-week or weekend barbeques: Alessandro, Pedrão, Quake, Roma, Alex, Ursão, Jacaré and anyone else I might have forgotten. Also my greetings to all my longer date friends from the cities of Jaú and Itapuí. I really miss all of those people on a daily basis and hope that life will bring us closer again one day.

In Finland I made very special and long-lasting friendships inside and outside university environment that are worth of a lot of thanks. At ORC I always felt friend of everyone that I somehow interacted or not, but my special thanks for Eero, Riku, Kostiantyn and Jarno for all the beers, memes, laughs and teachings of Finnish culture (although I definitely regret learning the existence of some sauna games but also happy of never taking part of them). My cheers to all my friends outside university that kept a broad range of topics and all the fun that we had either on amazing travels or simple board/electronic games nights: Deepak, Jobin, Biju, Philipp, Josh, Draupathy, Silvia and everyone else. Also for having the chance of being part of the greatest fully-foreign Pesapällo team: Perus-Ulkomaalaiset. At last but not least, I acknowledge Kultainen Apina, the best pub in Tampere, for being the stage of countless after-work Fridays beers (other mid-week days might have happened, it is classified) with funny and productive discussions covering all range of topics. Kippis! Cheers! Saúde!

ABSTRACT

The thesis is concerned with study of GaAs nanowires fabricated on Si substrate. The possibility of growing III-V semiconductor materials directly on silicon in the form of nanowires is an attractive route to the integration of microelectronic, photonic and optoelectronic technologies. To this end, development of functional heterostructure require effective and controllable doping but the dopant incorporation mechanisms involved in nanowire growth can be quite different from the well-established semiconductors thin film technology. The interplay of the different dopant incorporation mechanisms and the competition between axial and radial growth can result in dopant concentration gradients in the nanowires.

As a key technology development enabling the study of transport properties in nanowires, a method for fabricating electrical contacts on single NWs using electron-beam lithography is reported. On the other hand, the reduced dimensions and the quasi one-dimensional nanowire geometry are challenging factors for the fabrication of electrical contacts in the correct geometry for Hall effect measurement, which is traditionally used in planar film to determine the dopant concentration and carriers mobility. Therefore, alternative techniques were employed to gain an understanding of the dopant incorporation mechanisms. To this end, Raman spectroscopy and current-voltage analysis on single-nanowire were used to estimate the spatial distribution of the Be and Te dopants along the axial direction of GaAs nanowires. The study reveals that the dopant incorporation mechanisms are strongly affected by the growth conditions for both *p*-type and *n*-type GaAs nanowires, resulting in gradients of dopant concentration along the nanowires.

Besides the carrier transport properties, the waveguide properties of semiconductor nanowires were explored in the area of chiral sensing and emission of circularly polarized light. By fabricating asymmetric gold layers deposited on the nanowires sidewalls and under the adequate experimental conditions an extrinsic optical chirality configuration is achieved. The results show a strong chiral behavior in both absorption and emission of the partially Au-coated nanowires, and paves the way for applications such as chiral sensing and emitting devices.

RESUMO

Neste trabalho, realizamos um estudo sistemático das propriedades óticas, elétricas e estruturais de nanofios de GaAs dopados crescidos por epitaxia por feixes moleculares em substratos de Si. A possibilidade de crescer materiais semiconductores III-V na forma de nanofiosdiretamente sobre silício é uma rota de significativo interesse para a integração tecnológica nas áreas da microeletrônica, fotônica e optoeletrônica. Além disso, o desenvolvimento de heteroestruturas funcionais requer um processo de dopagem efetivo e controlável. No entanto, os mecanismos de incorporação de dopantes envolvidos no crescimento de nanofios podem ser diferentes dos mecanismos já conhecidos para filmes finos semicondutores. De forma geral, a combinação dos diferentes mecanismos de incorporação de dopantes e a competição entre crescimento axial e radial podem resultar em um gradiente de concentração de dopantes nesses nanofios.

O desenvolvimento de uma metodologia para fabricação de contatos elétricos em um único nanofio, utilizando litografia por feixe de elétrons, é um elemento chave para a investigação das propriedades de transporte eletrônico em nanofios. Por outro lado, as dimensões reduzidas e a quase uni-dimensionalidade dos nanofios são fatores desafiadores para a fabricação de contatos elétricos na geometria adequada para medidas de efeito Hall, tradicionalmente utilizada em filmes finos para determinar a concentração de dopantes e a mobilidade dos portadores de carga. Desta forma, nesta tese foram aplicadas técnicas experimentais alternativas para investigar os diversos mecanismos de incorporação de dopantes nesses sistemas. Dentre elas, utilizamos espectroscopia Raman e medidas de corrente elétrica em função da voltagem aplicada em nanofios individuais para estimar a distribuição espacial dos dopantes Be e Te ao longo da direção axial de nanofios de GaAs. Observamos que os mecanismos de incorporação de dopantes nesses sistemas são fortemente afetados pelas condições de crescimentos para ambos nanofios de GaAs, tipo-*p* e tip-*n*, levando à presença de um gradiente na concentração de dopantes ao longo do comprimento dos nanofios.

Além das propriedades de transporte eletrônico, as propriedades de guia-de-onda de nanofios semicondutores também foram exploradas para detecção quiral e emissão de luz circularmente polarizada nesses sistemas. Para isso, utilizamos camadas de Au assimétricas depositadas na superfície lateral dos nanofios, resultando na observação de quiralidade óptica extrínseca. Os resultados evidenciam um forte comportamento quiral tanto na absorção como na emissão de luz de nanofios parcialmente cobertos com Au, criando novas possibilidades para aplicações na área de dispositivos baseados em detecção e emissão quiral.

CONTENTS

ABBREVIATIONS

APT	Atom probe tomography
BF	Bright-field
CD	Circular dichroism
CPPM	Coupled phonon-plasmon mode
EBL	Electron beam lithography
FE	Field emission
FIB	Focused ion beam
HR-TEM	High-resolution transmission electron microscopy
IV	Current-voltage
LCP	Left-handed circular polarization
LO	Longitudinal optical
MBE	Molecular beam epitaxy
NW	Nanowires
PAS	Photo-acoustic spectroscopy
PIC	Photonic integrated circuit
PL	Photoluminescence
RCP	Right-handed circular polarization
RQ	Research questions
RTA	Rapid thermal annealing
SAED	Selected-area electron diffraction
SO	Surface optical
TE	Thermionic emission
TEM	Transmission electron microscopy
TF	Thin film
TFE	Thermionic field emission
TLM	Transmission line model
TO	Transverse optical
VLS	Vapor-liquid-solid
VS	Vapor-solid
WZ	Wurtzite

ZB	Zincblende

ORIGINAL PUBLICATIONS

Publication I. M. R. Piton, E. Koivusalo, T. Hakkarainen, H. V. A. Galeti, A. D. G. Rodrigues, S. Talmila, S. Souto, D. Lupo, Y. G. Gobato and M. Guina. (2019). Gradients of Be-dopant concentration in self-catalyzed GaAs nanowires. Nanotechnology 30:335709. DOI: 10.1088/1361-6528/ab1a97.

Publication II. T. Hakkarainen, M. R. Piton, E. M. Fiordaliso, E. D. Leshchenko, S. Koelling, J. Bettini, H. V. A. Galeti, E. Koivusalo, Y. G. Gobato, A. D. G. Rodrigues, D. Lupo, P. M. Koenraad, E. R. Leite, V. G. Drubrovskii and M. Guina (2019). Te incorporation and activation as n-type dopant in self-catalyzed GaAs nanowires. Phys Rev Mater 3:086001. DOI: 10.1103/PhysRevMaterials.3.086001.

Publication III. M. R. Piton, T. Hakkarainen, J. Hilska, E. Koivusalo, D. Lupo, H. V. A. Galeti, Y. G. Gobato and M. Guina (2019). Optimization of Ohmic contacts to p-GaAs nanowires. Nanoscale Res Lett 14, 344. DOI: 10.1186/s11671-019-3175-8.

Publication IV. G. Leahu, E. Petronijevic, A. belardini, M. Centini, C. Sibilia, T. Hakkarainen, E. Koivusalo, M. R. Piton, S. Suomalainen and M. Guina (2017). Evidence of Optical Circular Dichroism in GaAs-Based Nanowires Partially Covered with Gold. Adv Opt Mater **5**:1601063. DOI: 10.1002/adom.201601063.

Publication V. T. Hakkarainen, E. Petronijevic, M. R. Piton and C. Sibilia (2019). Demonstration of extrinsic chirality of photoluminescence with semiconductor-metal hybrid nanowires. Sci Rep 9:1–8. DOI: 10.1038/s41598-019-41615-1.

AUTHOR'S CONTRIBUTIONS

The results included in the thesis were obtained as part of a team effort. The nanowires investigated were grown by the molecular beam epitaxy experts Teemu Hakkarainen and Eero Koivusalo. The Author, Marcelo Rizzo Piton, was involved in the planning and discussion of the nanowire growth. The Author was responsible of planning and executing the Raman spectroscopy, fabrication of electrical contacts, current-voltage measurements, and fabrication of the asymmetric gold layers on the nanowires sidewalls. The majority of the scanning electron microscopy used in this thesis and publications were obtained by the Author. More specific details of the Author's contributions for each publications are described in the following:

Publication I

The Author was the main responsible for writing the manuscript. The Author planned and executed the Raman spectroscopy measurements and performed the fit procedures used in the manuscript. The Author was responsible for the design and fabrication of the electrical contacts used for transport analysis, in addition to developing the oxide removal, surface passivation and metallic multilayer. The scanning electron microscopy images used in the manuscript were obtained by the Author. The Author participated in the transmission electron microscopy measurements and interpreted the microscopy data.

Publication II

The Author was responsible for part of the writing of the manuscript. He planned and executed the Raman spectroscopy measurements and was the main responsible of the interpretation of the results. The Author was responsible for the design and fabrication of the electrical contacts and developed the processing parameters used. The current-voltage curves were measured by the Author and the main transport mechanisms presented were discussed between the Author and Teemu Hakkarainen. The results from Raman spectroscopy and current-voltage analysis were fundamental for proposing the existence of Te-dopant gradients on the GaAs nanowires. These results obtained by the Author were the motivation for international partners to take interest in collaborating with the transmission electron

microscopy, atom probe tomography, off-axis electron holography and theoretical model. The Author took a major role in devising the understanding of the Te-incorporation by combining and interpreting the results from several complementary experimental techniques.

Publication III

The Author was the main responsible for writing the manuscript. He planned, designed and fabricated the different processing parameters investigated in the publication. The Author defined the strategy for current-voltage analysis and interpretation of the results. All the scanning electron microscopy images were obtained by the Author. He also prepared the samples used for x-ray diffraction analysis. The Author was involved in the interpretation and correlation of the x-ray diffraction results with the current-voltage analysis from the nanowires.

Publication IV

The Author was responsible for the design, development, and deposition of the asymmetric gold layers partially covering the nanowire sidewalls, which were investigated by photo-acoustic spectroscopy by the collaboration partners. The Author took part in preparation of the manuscript.

Publication V

The Author was responsible for the design development of the asymmetric gold layers, optimized the gold deposition and deposited gold on the samples investigated by photoluminescence spectroscopy. He took part in preparation of the manuscript.

1 INTRODUCTION

1.1 III-V semiconductor nanowires and Si integration

Semiconductor nanowires (NWs) are a promising class of materials as building blocks for the next generation of electronic and optoelectronic devices [1]. The advanced growth techniques available for manufacturing semiconductor heterostructures and the diversity of device processing techniques are the key ingredients for obtaining novel sophisticated device nanostructures. Vigorous development in the various sub-field of nanotechnology led to development of several classes of nanostructures. In relation to the confinement type of the charge-carriers, semiconductor heterostructures can be classified as bulk (3D), quantum-wells (2D), quantum-wires (1D) and quantum dots (0D). In relation to their geometry, majority of the structure have a planar 2D geometry while NWs are classified as one-dimensional structures due to their high aspect ratio, i.e., the length of the NWs can be a few orders of magnitude larger than their diameter. However, the type of confinement will be dictated by the relation between the NW diameter and the exciton Bohr diameter. Therefore, it is possible to obtain one-dimensional NW structures while still keeping the bulk-like confinement behavior by growing NWs with a sufficiently large diameters.

Semiconductor NWs can offer a number of advantages over their bulk counterparts, for example the reduced dimensionality provides some mechanical flexibility for future devices applications [2]. In addition, the increased surface-to-volume ratio makes NWs attractive for sensing applications, while indeed bringing more challenges in terms of surface passivation required to avoid the loss of carrier at outside interface. Recently, NW-based optoelectronic devices have been exploited in applications such as LEDs [3, 4], solar cells [5, 6] and photodetectors [7].

The integration of III-V semiconductor materials with the Si-based technology platform dominating microelectronics and passive photonic integrated circuits (PICs) is a major trend aiming at exploiting the benefits of photonics by increasing the functionality of PICs. As an example of such integration, the work of Giuntoni

et al [8] proposed a direct interface of semiconductor nanowires and planar Si waveguides as show in Figure 1.1.

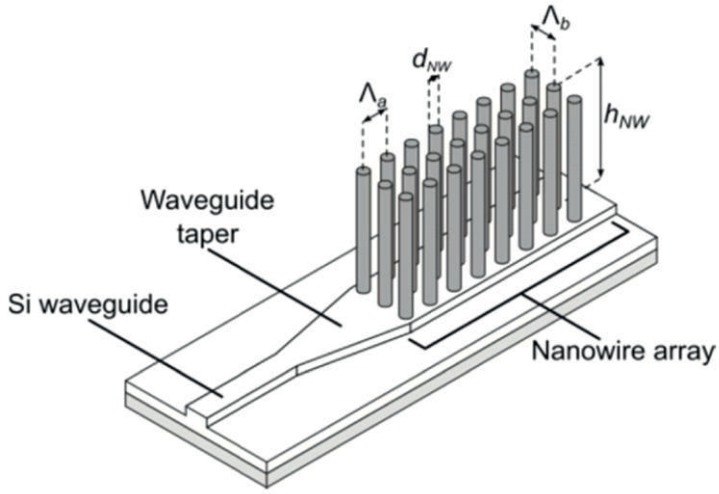

Figure 1.1: Periodic array of free-standing semiconductor nanowires on a planar Si waveguide. Reprinted with permission from [8]. © The Optical Society.

The main obstacle for effective integration of III-V and Si-based technologies is the lattice mismatch between Si and most typical III-V semiconductors, such as gallium arsenide (GaAs). The crystalline defects arising from the different lattice constants are highly detrimental for the optical and electronic transport of the resulting heterostructures. The difference in the coefficients of thermal expansion between the semiconductor materials also plays a detrimental role in the direct integration of Si and III-V semiconductor materials.

Owing to their reduced dimensionality, III-V NWs are able to overcome the lattice and thermal mismatches issues due to the strain relaxation in the first atomic layers at the interface between the growth substrate and the NW structure. Therefore, significantly progress has been made on the growth of III-V semiconductor NWs directly on Si substrate. Specifically to GaAs NWs, advances in the NW distribution and control of the length and diameter of the final structures have been reported [9–12]. Most electronic and optoelectronic applications require modifications of the semiconductor conductivity properties by incorporation of additional elements referred as dopants, as will be discussed in details later in this thesis. For example, a solar cell is based on a pn-junction formed by doping part of

the structure with p-type dopants and another part with n-type dopants. The device performance is largely defined by the charge carrier concentrations, mobilities and lifetimes in the pn-junction.

Therefore, one of the prior concerns regarding NW-based devices performance is a reliable doping procedure without compromising the material quality of the NWs. A handful of scientific publications involving several experimental techniques and approaches have emerged during the past years [13–18] with the common goal of estimating the dopant concentration and incorporation pathways of dopants into semiconductor NWs, but the results are usually highly-dependent on the growth method and dopant being used. It should be emphasized that the research methodology and knowledge of the dopant incorporation from traditional thin film epitaxy cannot be directly transferred to NWs. For example, Si is a common *n*-type dopant in MBE growth of GaAs(100) thin films but has a strong amphoteric behavior in NW growth [16]. From this general perspective, this thesis contributes to a systematic build-up of knowledge of dopant incorporation mechanisms during nanowire growth.

1.2 Research questions and structure of the Thesis

In terms of specific problems addressed, this thesis work is addressing the following fundamental research questions (RQ):

RQ1: How are the structural, optical and carrier transport properties of the NWs linked?

RQ2: How are the NW growth conditions linked to the incorporation mechanisms and efficiency of Te (*n*-type) and Be (*p*-type) dopants in self-catalyzed MBE GaAs NWs?

RQ3: How does the incorporation of Te and Be dopants affect the structural, optical and electrical properties of the NWs?

RQ4: To which extent can the traditional III-V semiconductor device processes be applied to the NW device fabrication and what kind of new challenges and possibilities result from the NW geometry?

The planning of the experiments used in the investigation of the Be and Te dopants incorporation in the self-catalyzed GaAs nanowires used in this thesis is based on the RQs 1-4. The main aspects of the changes in the structural properties due to

dopant incorporation were analyzed by scanning electron microscopy, transmission electron microscopy and Raman spectroscopy. In addition, Raman spectroscopy data were used to estimate the dopant concentration and carrier mobility via analysis of the coupling of the plasma associated to the free charge carriers and the phonons of the NW lattice. The charge carriers transport properties of Be and Te-doped NWs were investigating by fabricating electrical contacts on single NWs using electron-beam lithography (EBL). The main transport mechanisms were identified by analyzing the current-voltage (IV)characteristics of the NWs and correlating with the results obtained from Raman spectroscopy. Prior to transport characterization, the optimization of the steps involved in contacts manufacturing was a key research point (RQ4), enabling to obtain a repeatable process ensuring low contact resistance of the metal-semiconductor interface.

In terms of new applications exploiting the unique properties of the NW geometry, we have investigated the extrinsic optical chirality of the absorption and emission of semiconductor-metal hybrid nanostructures. To this end, GaAs/AlGaAs core-shell NWs had their sidewalls partially covered with gold by properly designing the tilt angle of the NWs axis and the metal flux direction during metal evaporation. This design and fabrication approach opens the way for chiral sensing and biochemistry applications.

2 GENERAL BACKGROUND

In this chapter, the main theoretical concepts underpinning the experimental work are presented. A brief section of III-V semiconductor materials is given at the start focusing on GaAs properties. The doping effects on the energy bands of intrinsic semiconductors is also presented in order to discuss the fabrication of electrical contacts onto semiconductor materials. The main aspects of metal-semiconductor junctions are presented to support the discussion of electronic transport properties of the nanowires. Then, a presentation of the main theoretical aspects of Raman spectroscopy applied to semiconductor materials is presented, including the Raman scattering phenomenon, selection rules for bulk and nanowires, surface optical modes as well as the coupling of the phonon modes to the plasma due to the presence of free carriers. The latter has been of great importance when evaluating the dopant concentration and carrier mobility of the *n* and *p*-type nanowires investigated in this thesis. At last, a brief description of extrinsic optical chirality of the Au-coated nanowires is presented.

2.1 III-V semiconductor compounds and GaAs

The III-V semiconductor compound gallium arsenide (GaAs) is one of the most investigated material of its class, present in a wide range of applications in electronics and optoelectronic devices. In particular, the direct nature of GaAs band-gap, which is a common feature among several III-V compounds, is essential for light emitters. At room temperature, undoped GaAs has an energy gap of 1.42 eV (~870 nm in wavelength) and therefore is widely used in near-infrared optoelectronic applications. Besides the direct nature of the bandgap of the most III-V compounds, another important benefit compared to indirect bandgap Si dominating microelectronics and photovoltaics, is the possibility to form alloys covering a broad spectrum region. For example, as it can be seen in Fig. 2.2, formation of ternary alloys such as GaAsP and GaInP makes the Si-III-V integration even more attractive. On the other hand, the difference in lattice constants between Si and III-V materials results in difficult to overcame challenges when aiming at monolithic integration

between these materials; lattice difference results in defects and dislocations, which results in degradation of device performance.

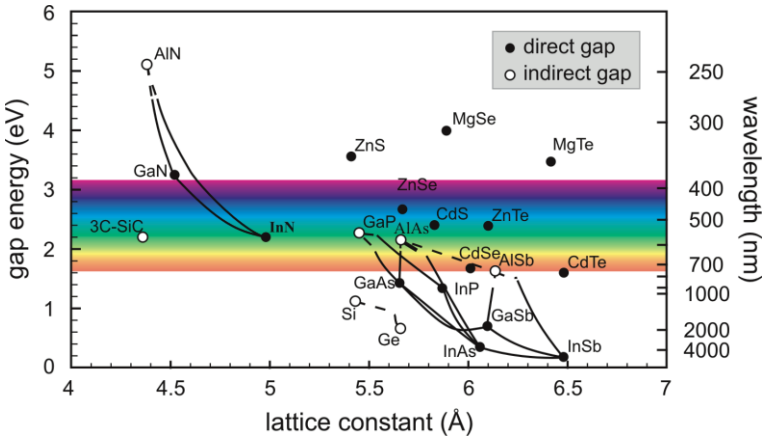

Figure 2.2: Bandgap *vs* lattice constants at room temperature of most important elemental and binary semiconductors. Adapted from [pending]

Most commonly, semiconductor materials exhibit diamond (in case of group IV semiconductors) or zincblende (compound materials) crystalline structures. The zincblende (ZB) crystalline structure can be seen as two interpenetrating face-centered cubic lattices [19]. In case of GaAs, one sub lattice is composed of Ga atoms and the other of As atoms. Another common crystalline structure for III-V semiconductor compounds is the wurtzite (WZ), which has hexagonal symmetry. The WZ structure can be seen as two interpenetrating hexagonal close-lacked lattices. Even though the WZ structure presents hexagonal symmetry, the four nearest neighboring atoms are arranged in a tetrahedral way similarly to the ZB structure. Some III-V semiconductors that are commonly observed in ZB structure can go through a phase transition to WZ structure, as for example GaAs under higher pressures and temperatures [20]. As it will be later discussed in this thesis, the possibility of growing III-V semiconductor materials in the NW form allows forming a metastable WZ phase of compounds which are naturally ZB.

Intrinsic semiconductor materials are grown without the presence of additional elements (or at least with a negligible amount of impurities), i.e. referred as dopants. In this case, for each electron that is excited from the valence to the conduction band there will a corresponding hole at the valance band, forming a so-called electron-hole pair. Each electron and hole generated this way are also referred as charge carriers. Therefore, the concentration n of electrons thermally excited in the

conduction band is equal to the concentration p of holes in the valence band which are equal to the intrinsic carrier concentration n_i. The energy distribution of the electrons in a semiconductor obeys the Fermi-Dirac statics, accounting for the indistinguishable nature of the electrons and the Pauli exclusion principle [21]. At equilibrium and finite temperatures, the carrier concentration in the conduction band (electrons) is equal to the carrier concentration in the valence band (holes), and the Fermi level of an intrinsic semiconductor lies very close to the middle of the bandgap.

For most practical applications in electronics and optoelectronics, it is usually required from the semiconductor material to have an excess of one type of charge carrier (electrons or holes) in order to change the semiconductor conductivity significantly. To this end, external impurities are introduced in such controlled way that will add or remove electrons from the semiconductor crystal – but still preserving the charge neutrality of the whole crystal. This procedure is known as doping of the semiconductor, and the dopants concentrations are usually 10^{16}-10^{19} atoms/cm^3. For example, beryllium (Be) impurities introduced in GaAs crystal will substitute Ga atoms which leaves a deficit of one electron per Be atom incorporated this way. In other words, each Be atom incorporated will contribute with one hole to the GaAs and the material is referred as *p*-type doped. Similarly, the introduction of tellurium (Te) in GaAs crystal will result in Te atoms occupying the some fraction of the As sites, thus leaving with one extra electrons per Te atom incorporated this way. Therefore, the material is referred as *n*-type doped. It is worth mentioning that the holes and electrons contributions by *p*-type and *n*-type impurities, respectively, are based for a crystal at room temperature. Some dopant atoms are known to have an amphoteric behavior, i.e., with probability of occupy lattice sites that would result in *p*-type or *n*-type doping. For example, Si is knows to have an amphoteric behavior in GaAs, which depends on the growth conditions and the crystal orientation of the growth surface orientation from which the dopants are being incorporated [22]. A semiconductor material with dopants intentionally incorporated is referred as *extrinsic*.

An extrinsic semiconductor material exhibits additional energy levels in the bandgap region: the acceptor levels are closer to the valence band, which can get filled by thermally-activated dopants. The donor levels are closer to the conduction band and thermally activated dopants will contribute to empty donor levels. The fact that the acceptor/donor levels are close to the valence/conduction bands facilitates the generation of free charge carriers when compared to the thermal excitation of electrons across the bandgap of the semiconductor material. [19, 21]. This concept

will be of importance when discussing the properties of metal-semiconductor junctions used for current-voltage (IV) analysis in the upcoming chapters.

2.2 Nanowire background

2.2.1 Vapor-liquid-solid growth

The usual growth mode of semiconductor nanowires is based on the vapor-liquid-solid (VLS) mechanism, which was first proposed already in 1964 by Wagner and Ellis [23] on the growth of Si structures assisted by metallic Au particles. In this method, a metal droplet is used as catalyst for the NW growth [24, 25]. In epitaxial growth, the substrate determines the crystal orientation of the growing structure (layers, NW, etc). In VLS growth, the catalyst can be either a foreign element (other than the constituent elements of the semiconductor) such as Au, Al, Ni or Ti [25] or a native element such as Ga in case of GaAs growth. In the latter case the VLS process is said to be self-catalyzed.

The main requirement for VLS growth of III-V semiconductor NWs is that the droplet can reach a supersaturation condition between the group III and group V elements used during NW growth regardless of the metal used as catalyst. The source material from the vapor phase is dissolved into the droplet. Once the supersaturation condition is reached in the liquid droplet, precipitation takes place at the liquid-solid interface of the catalyst droplet and NW body.

The NW growth takes place in a highly anisotropic fashion in a bottom-up form, and the catalyst droplet usually stays at the NW tip throughout the growth process. In self-catalyzed GaAs NW growth, the growth rate can be adjusted by the group V flux, but the control of the group III fluxes is important to keep the saturation conditions for VLS growth. If the V/III ratio is set too high, the catalyst droplet will shrink in size causing the liquid phase to disappear and thus terminating the VLS process. On the other hand, if the V/III ratio is not high enough, the increase in droplet size can result in formation of unwanted lattice defects along the NW axis such as twin planes. While the VLS mechanism is responsible for the axial growth of the NW, there can be also growth happening at the NW sidewalls through a mechanism known as vapor-solid (VS). This increase in the diameter is usually referred as radial growth and can be adjusted by the V/III ratio and temperature [25]. The VLS and VS growth modes will be important concepts when dopant

incorporation is discussed. In addition to NWs, parasitic growth structures and tilted NWs are observed to form during the NW growth. The parasitic structures often originate from failed NW nucleation, or parasitic nucleation in pinholes formed to the oxide during the NW growth. The main growth mechanisms during catalyst-assisted NW growth are illustrated in Figure 2.3.

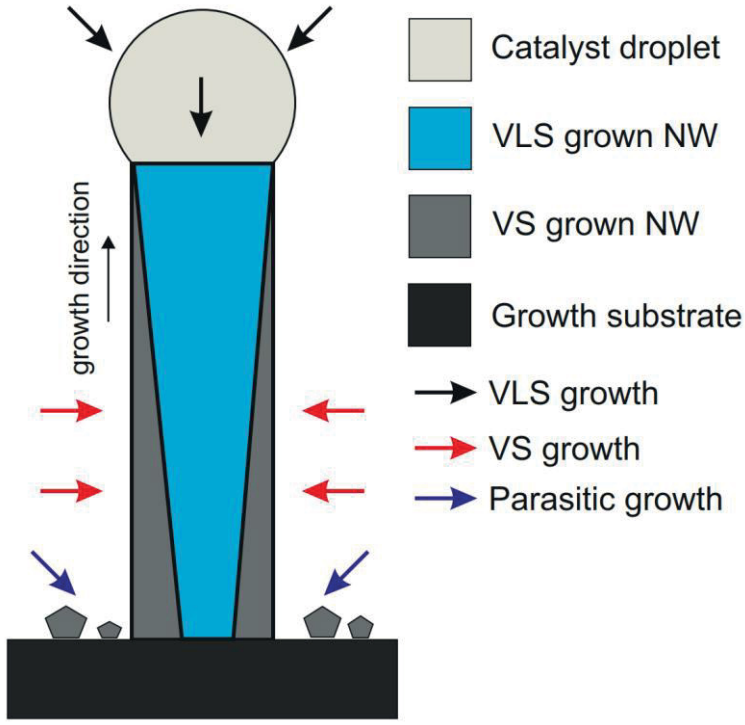

Figure 2.3: Schematics of the main mechanisms in catalyst-assisted NW growth.

2.2.2 Self-catalyzed growth mechanisms

The use of Au nanoparticles as catalyst for the growth of III-V semiconductor nanowires has been widely reported using both MBE and MOCVD fabrication techniques [1, 26]. However, it is usually preferred to avoid the use of Au due to its high diffusion coefficient in semiconductor materials and the tendency to induce deep level traps in the semiconductor bandgap, which will drastically decrease the performance of NW-based optoelectronic devices [24].

A straightforward solution to the harmful effects of Au diffusion (or any other foreign elements) into the semiconductor NW is to use a catalyst droplet of the same components of the NW composition. This approach is commonly referred as self-catalyzed growth, and the VLS growth kinetics are very similar to the Au-catalyzed in terms of droplet supersaturation requirements and axial/radial growth [25]. There is need of better control of the growth conditions in self-catalyzed NW growth when compared to Au-catalyzed, since the catalyst dimensions are more sensitive to temperature and V/III flux.

The self-catalyzed method is particularly successful for MBE growth of III-V NWs, owing to the high purity materials used and resulting in good crystal quality [10, 24]. The growth conditions can be tuned to crystallize the catalyst droplet and promote the VS growth, creating core-shell structures [9, 10]. In addition, the MBE technique allows the growth of complex heterostructures and obtaining abrupt doping interfaces in the semiconductor materials, which are essential, for example, for obtaining high-quality *pn*-junctions used in optoelectronic applications.

2.2.3 Dopant incorporation mechanisms

In order to have semiconductor NWs as competing nanostructures for practical applications in electronics and optoelectronics, it is essential to have an effective and controllable doping procedure without compromising the structural quality of the NWs. Owing to the unique growth mechanisms of III-V NWs discussed before, the dopants will also have a number of incorporation paths into the NWs and those can be quite different from the well-established dopant incorporation mechanisms in thin film (TF) planar epitaxy. Therefore, a large amount of efforts have been put to understand the dopant incorporation pathways and how it can be affected by the growth conditions [27, 28].

During NW growth, the dopants can incorporate by the VLS mechanisms (through the catalyst droplet), by the VS mechanism during radial growth of the NW, and also by diffusion from the surface [29, 30]. Even though the dopant incorporation mechanisms have been extensively investigated for Au-catalyzed NW growth, the conditions for the self-catalyzed growth can be significantly different. For instance, the growth temperature of self-catalyzed growth is significantly higher than Au-catalyzed and therefore affects the material deposition and incorporation kinetics [29]. The dopant incorporation mechanism can influence the atomic sites which the impurities will occupy, which can lead to amphoteric behavior. For

example, Si dopant is widely used as *n*-type dopant in VS growth of planar GaAs but it was observed that it can result in *p*-type doping when incorporated via the VLS mechanism in GaAs NWs [22, 31]. The dopant incorporation follow similar mechanisms that are presented in Figure 2.3 for catalyst-assisted NW growth.

In the case of *n*-type doping, Te is a promising alternative to the amphoteric behavior of Si in planar GaAs [32] and has been successfully used in the self-catalyzed growth of GaAs NWs [14, 16–18, 33]. In Publication II we showed that Te incorporates mainly by the VLS mechanism in self-catalyzed growth of GaAs NWs, but axial and radial dopant gradients were observed due to radial VS growth and possibly dopant diffusion from the VLS grown core to the VS-grown shell. Moreover, *p*-type doping during self-catalyzed growth has been successfully achieved using Be dopant and several incorporation mechanisms have been reported. Preferential VS incorporation of Be in the NWs sidewalls was observed by Casadei *et al* [15]. Preferential VLS incorporation of Be into GaAs NWs was proposed by Zhang *et al* [29] and Dastjerdi *et al* observed the Be dopants are predominantly incorporated via truncated facets at the NW-droplet interface and followed by diffusion into the NW core [30]. The dopant gradients could be avoided by carefully controlling the NW growth conditions.

2.3 Metal-semiconductor junction

Electronic transport characterization is a common way to obtain information of the dopant concentration and incorporation dynamics in semiconductor materials. For example, Hall Effect is a standard characterization method to obtain the dopant concentration and charge carrier mobility of doped semiconductor materials [21]. The fabrication of electrical contacts is an essential step in the transport characterization techniques, enabling to apply a voltage difference or to inject electrical current between two regions of a semiconductor sample. When a metal is put into contact with a semiconductor, the tendency to align the Fermi level of metal and semiconductor results in charge transfer between both materials [21]. This results in a depletion layer W and a contact potential V_0 formed at the junction region when equilibrium is established. In addition, the phenomenon of *band bending* [21] will occur in the region of the depletion layer. The band bending is influenced by the depletion layer width and is dependent on the dopant concentration. As will be later discussed, this will be an important factor determining the current transport mechanisms in semiconductors at the nanoscale regime.

The amount in energy that the Fermi levels are shifted when creating a junction will depend on the *work functions* of the metal ($q\phi_m$) and the semiconductor ($q\phi_S$), which are defined as the energy required to remove an electron at the Fermi level to the vacuum level [21]. The work function of a semiconductor material depends on the electron affinity χ (measured from the bottom of the conduction band to the vacuum level) and energy difference between the conduction band and the Fermi level, denoted by V_n. Therefore, the semiconductor work function can be written as $q\phi_S = q(\chi + V_n)$ and the contact potential is given by $qV_0 = q\phi_m - q\phi_S$ [19]. In general, the current transport mechanisms will depend on the properties of the metal-semiconductor junction, which are by their turn mostly dependent on the semiconductor properties such as doping levels and surface states [19].

The change in the work function of a semiconductor in contact to a metal is a result of the image forces induced at junction boundaries, and this phenomena is called the *Schottky effect* [21]. The minimum energy that the charge carriers (electrons or holes) must have to flow between the metal and semiconductors is usually referred as *Schottky barrier* (ϕ_B), and can be further lowered or increase by the presence of an external electric field [19]. For an *n*-type semiconductor, the Schottky barrier is the difference between the metal work function and the semiconductor electron affinity:

$$q\phi_{Bn} = q(\phi_{\mathrm{m}} - \chi) \tag{2.1}$$

And the Schottky barrier for a *p*-type semiconductor is:

$$q\phi_{Bp} = E_g - q(\phi_m - \chi), \tag{2.2}$$

where E_g is the semiconductor bandgap. The energy diagrams of Schottky barrier formation of metal-semiconductor junction for *n*-type and *p*-type semiconductors are shown in Figure 2.4. The formulation presented by equations (2.1) and (2.2) describes an ideal metal-semiconductor junction where the presence of *surface states* are not considered. The surface of a semiconductor is composed by incomplete bonds that leads to charges at the contact interface [19, 21]. In addition, a thin native oxide layer is often present at the semiconductor surface, which further contributes to the Schottky barrier formulation. The presence of interfacial layers in compound semiconductors leads to the formation of additional surface states localized at the semiconductor bandgap and causes the Fermi level to be pinned at a fixed energy.

Therefore, the Schottky barrier height ϕ_B will depend on the properties of the semiconductor surface and not only on the metal work function.

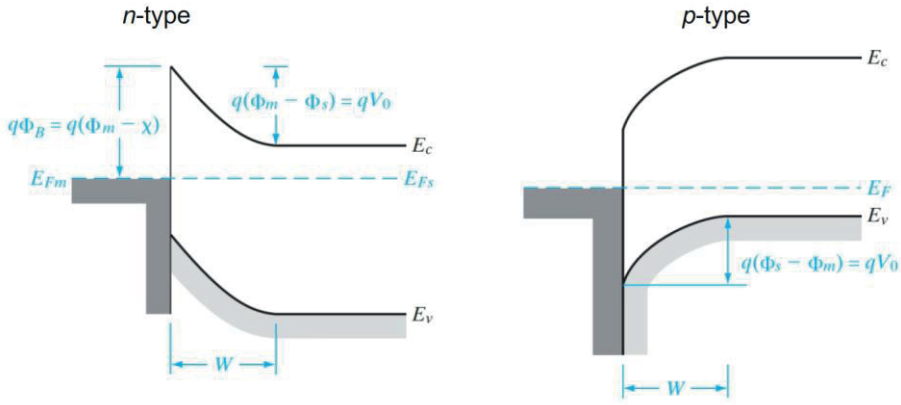

Figure 2.4: Band diagram at equilibrium for metal-semiconductor interface for n-type and p-type doping. Adapted from [21]

For a moderate dopant concentration, the current flow through a Schottky barrier under reversed bias is described by a diode equation based on the *thermionic emission model* [21]:

$$I = ABT^2 e^{-q\Phi_B/kT} e^{qV/nkT} \tag{2.3}$$

Where A is device cross-sectional area, B is a parameter depending on the junction properties and n is an analogue of a diode's ideality factor. Devices described by equation (2.3) are known as Schottky diodes and have rectifying characteristics for either *n* or *p*-type semiconductor materials. Usually, it may be preferred to have metal-semiconductor contacts with a linear IV behavior regardless the bias voltage polarity and with minimal electrical resistance associated to the contacts as possible. Such metal-semiconductor interfaces are called *Ohmic* contacts.

Ohmic contacts to semiconductor materials will often exhibit linear IV behavior at small voltages. However, at higher voltages the IV can become non-linear due to the existence of a depletion layer [34]. Therefore, a practical rule is that a contact can be considered Ohmic if it can provide an electrical current with a sufficiently small voltage drop when compared to the region across the device – even if the IV behavior of the contact is not strictly linear [34]. In Ohmic contact formation, the Fermi levels of the metal and semiconductor tend to align in such way that the charge carriers can flow through the contacts for any small external bias applied. In other

words, this means that there is virtually no barrier at the metal-semiconductor interface. For *n*-type semiconductors, the raise in the Fermi level relative to the metal results in an easier flow of electrons from the metal to the semiconductor, which is valid for metals with work function $\phi_m < \phi_S$. In the case of $\phi_m > \phi_S$ for *p*-type semiconductors, the lowering of the Fermi level in relation to the metal leads to a facilitated flow of holes across the junction. Figure 2.5 illustrates the band diagrams at equilibrium of a metal-semiconductor junction for *n*-type and *p*-type doping [21].

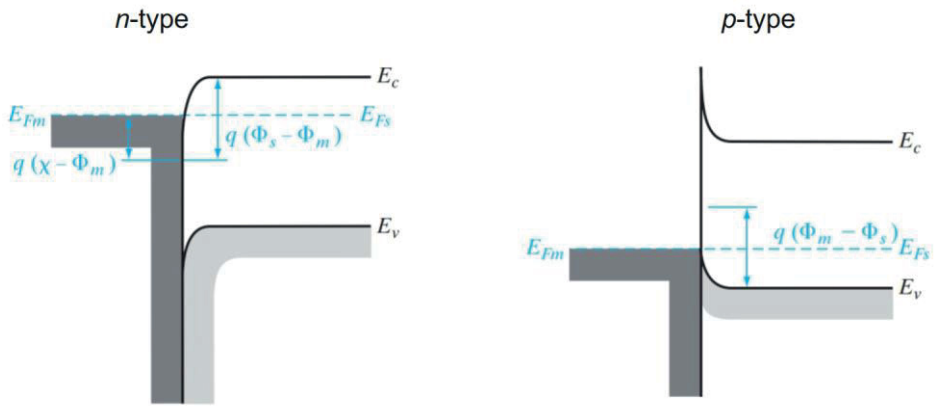

Figure 2.5: Equilibrium band diagram for Ohmic metal-semiconductor contacts to n-type and p-type semiconductor. Adapted from [21].

The Fermi level pinning is a well-known phenomenon in semiconductor materials with high number of surface states, such as GaAs and InAs [19, 21] and the mechanism of current transport will depend on the doping level of the semiconductor. At low to moderate doping concentrations, the current transport is due to thermionic emission (TE) over the barrier, resulting in typical Schottky diode behavior with saturation of the reverse current. Linear IV characteristics and low contact resistance are associated to Ohmic contacts and are obtained at high doping concentration, when the barrier width (depletion layer) is reduced. At high doping levels, an increase in the tunneling probability of electrons with energy close to the Fermi level of the semiconductor is ascribed to field emission (FE) mechanisms. In an intermediate doping level, where the barrier is still too wide for tunneling of the charge carriers at the Fermi level, the dominant current transport mechanism is known as thermionic field emission (TFE). The TFE involves tunneling of thermally excited electrons through the upper part of the barrier [35, 36].

2.4 Raman spectroscopy

Light traveling through a medium can be transmitted, absorbed and/or scattered. The first two phenomena follow the standard laws of reflection and refraction. The scattering of light due to inhomogeneities of a medium can be elastic (without change in frequency) due to static scattering centers, such as dislocations in a crystal, or inelastic, where there can be an increase or decrease of the scattered light frequency (i.e., energy) in respect to the incident radiation. Inelastic scattering of light is usually associated to dynamic changes of the medium, such as atomic vibrations (phonons), fluctuations of the electrical charge or spin density. Macroscopically speaking, the inelastic scattering of light is caused by an oscillation in the electric susceptibility χ of the medium induced by the atomic displacements caused by the incidence of the sinusoidal plane electromagnetic wave. This induces a polarization wave, or changes in the medium polarizability, which produces radiation from two components: a *Stokes* shifted wave (with energy *smaller* than the incident wave) and an *anti-Stokes* shifted wave (with energy *larger* than the incident wave). The difference between the frequencies of the incident and scattered radiations are equal to the phonon frequency associated to the lattice vibrations, and is usually referred as *Raman shift* [37]. Therefore, the measurement of the intensity of scattering radiation *versus* the Raman shift values is called Raman spectroscopy.

Owing to its versatility, Raman spectroscopy is a widely-used characterization tool for minerals, organic, ceramic, semiconductor materials etc. It can be used to obtain information on the crystalline structure, composition, phonon dispersion and electronic states of the investigated material. In particular for semiconductor materials, Raman spectroscopy can be applied to investigate the composition, crystalline and electronic structure, defects, strain and electron-phonon interaction, for example providing information on lattice dynamics and phonon dispersion in GaAs [38].

GaAs usually crystallizes in cubic ZB structure in its bulk form, but can also be intentionally obtained in hexagonal WZ phase when in NW form [39, 40]. In its ZB phase, GaAs has a $T_d^2(F\bar{4}3m)$ symmetry and therefore presents a two-atom based face-centered cubic Bravais lattice [21, 37]. The phonon branches in ZB GaAs are divided into three acoustic and three optical, where the optical phonons at the Γ point are split into a transverse optical (TO) and longitudinal optical (LO) mode [41] at ~269 cm^{-1} and ~291 cm^{-1} respectively, as illustrated in Figure 2.6 adapted from Refs [39, 41]. The phonon dispersion of WZ GaAs can be obtained from the ZB GaAs phonon dispersion by considering the crystallographic relation between both

structures. The difference between ZB and WZ is only at the stacking of the Ga-As layers to the $(111)_{ZB}/(0001)_{WZ}$ planes [39], therefore the phonon dispersion of WZ can be interpreted as folding the ZB phonon dispersion curve along the [111] direction [39], as illustrated in Figure 2.6 [42]. The TO and LO modes from ZB and WZ have the same frequencies and an additional WZ-related E_2^H mode at ~259 cm^{-1} is usually used to identify the presence of WZ phase in GaAs NWs. This crystallographic similarities between ZB and WZ phases will be very useful when analyzing the Raman spectra of ZB NWs with high density of twin planes along the growth direction. A twin plane in ZB phase can be seen as a mirror plane with the stacking of the ZB planes (ABCABC) is changed to ABCACBA, and a periodic array of twin planes can result in hexagonal symmetry to the NW [43]. Therefore, it is important to have additional knowledge of the crystalline structure of the material under investigation to avoid misinterpretation of the Raman spectra.

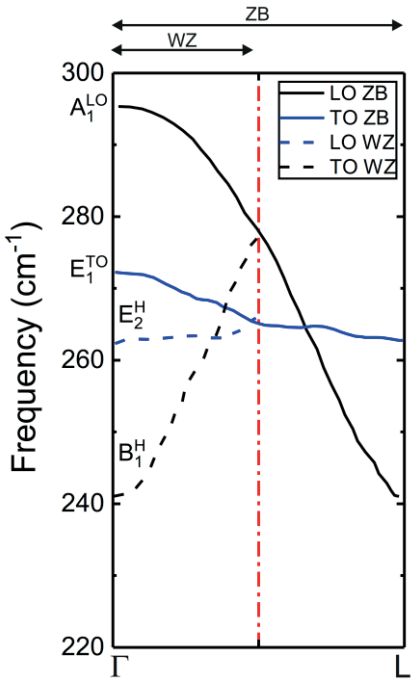

Figure 2.6: Optical phonons dispersion of ZB GaAs (solid lines) and schematic representation of the optical phonons dispersion of WZ GaAs (dashed lines) that results from folding the ZB dispersion along the $\Gamma \rightarrow L$ crystallographic directions. Adapted from [39]

2.4.1 Raman selection rules

The atomic displacements (Q) during the inelastic scattering of light causes a change in the electric susceptibility χ of the medium. A *Raman tensor* (R) can be defined as the derivative of the susceptibility in respect to the atomic displacements Q, in the form [37]:

$$\boldsymbol{R} = \left(\frac{\partial \chi}{\partial \boldsymbol{Q}}\right) \widehat{\boldsymbol{Q}}(\omega_0) \tag{2.4}$$

As an example, a crystal with ZB crystalline structure have the following Raman tensors in the main crystal axis system (x = [100], y = [010] and z = [001]) [44]:

$$\boldsymbol{R}\,(x) = \begin{bmatrix} 0 & 0 & 0 \\ 0 & 0 & d \\ 0 & d & 0 \end{bmatrix}; \quad \boldsymbol{R}(y) = \begin{bmatrix} 0 & 0 & d \\ 0 & 0 & 0 \\ d & 0 & 0 \end{bmatrix}; \tag{2.5}$$

$$\boldsymbol{R}(z) = \begin{bmatrix} 0 & d & 0 \\ d & 0 & 0 \\ 0 & 0 & 0 \end{bmatrix}$$

Where d is the only non-zero, linearly independent component of the derivative $\partial\chi/\partial\boldsymbol{Q}$. The intensity of the Raman scattering will depend on the polarization of the incident ($\boldsymbol{e_i}$) and scattered ($\boldsymbol{e}_s$) radiation in the form [37]

$$I \propto |\boldsymbol{e}_i \cdot \boldsymbol{R} \cdot \boldsymbol{e}_S|^2 \tag{2.6}$$

The symmetries of the medium and the allowed vibrational modes involved in the scattering process implies that the scattered radiation intensity might be zero for certain combinations of the polarization of incident and scattered radiation, as well as the scattered geometries involved. These combinations are known as the *Raman selections rules* for a determined crystalline structure. In semiconductors with ZB crystalline structure, such as GaAs, the optical phonons at the Γ point of the Brillouin zone are split in a transverse optical (TO) and longitudinal optical (LO) modes and may or may not be allowed by the Raman selection rules depending on the scattering

geometry. Therefore, it is important to have the Raman scattering geometry well defined and planned according to the selection rules and optical phonon modes that are of interest. Usually, the Raman scattering geometry is defined by four vectors: two are the direction of the incident and scattered photons ($\boldsymbol{k}_i$ and $\boldsymbol{k}_S$ respectively) and the other two are the polarization of the incident and scattered photons ($\boldsymbol{e}_i$ and $\boldsymbol{e}_S$ respectively). In the Porto notation, the scattering geometry is written as $\boldsymbol{k}_i(\boldsymbol{e}_i, \boldsymbol{e}_S)\boldsymbol{k}_S$.

The most common and simple scattering geometry used in semiconductors characterization is the backscattering, where the $\boldsymbol{k}_i$ and $\boldsymbol{k}_S$ are antiparallel to each other. The Raman tensors in Equation (2.5) can be used to describe the selection rules for backscattering from GaAs (100) surface, with the consideration that the LO and TO modes have different, non-zero, Raman polarizability elements [44], so that $d_{LO} \neq d_{TO}$. In backscattering of ZB GaAs (100), the LO is the only mode allowed by the Raman selection rules [37] and the observance of TO mode is usually associated to disorder effects, such as the presence of dopants or other defects causing the break of the crystalline periodicity.

Self-catalyzed GaAs NWs grow usually on the [111] direction and exhibit hexagonal cross-section with {110}-orientation sidewalls [12, 29, 30, 45]. The Raman tensors and selection rules for backscattering of high crystalline indexes surfaces of ZB semiconductors have been previously reported [44] and it was shown that in backscattering of (110) surfaces the LO mode is forbidden and TO mode is an allowed mode, in the case of plane waves incidence. Usually the NWs are harvested from the growth substrate and transferred to other substrate for micro-Raman experiments and measured in the backscattering geometry. This means that 2 out of 6 facets will be measured in backscattering of the {110} facets while the remaining facets will contribute to the Raman spectrum with different scattering geometry configuration [39]. It was previously reported that the remaining four NW sidewalls that are not perpendicular to the laser excitation will contribute to the LO spectra and that the remaining two facets will contribute to the TO spectra observed in GaAs NWs [46]. This partial relaxation of the Raman selection rules for NW geometry are from the fact that in micro-Raman experiments the scattered light is collected with a high NA objective. In this case, there are different propagation directions in the tightly focused beam, which is composed from several components of plane waves.

As an example, Figure 2.7 shows normalized Raman spectra measured in the backscattering geometry of GaAs (100) and (110) thin films. In addition, the Raman spectrum of a GaAs NW transferred to a SiO_2 substrate is shown. In this

configuration, the (110) NW sidewalls are measured in backscattering geometry as previously discussed. As is predicted by the Raman selection rules of backscattering of ZB crystals, only the LO mode is observed in the Raman spectrum of the GaAs (100) thin film while only the TO mode is observed for the GaAs (110) thin film. As a result of the NW sidewalls geometry, both TO and LO modes are observed in the Raman spectra of the GaAs NW. In addition, a surface optical (SO) mode is also observed as result of the increased surface-to-volume ratio of the NWs; this will be further discussed in the next section.

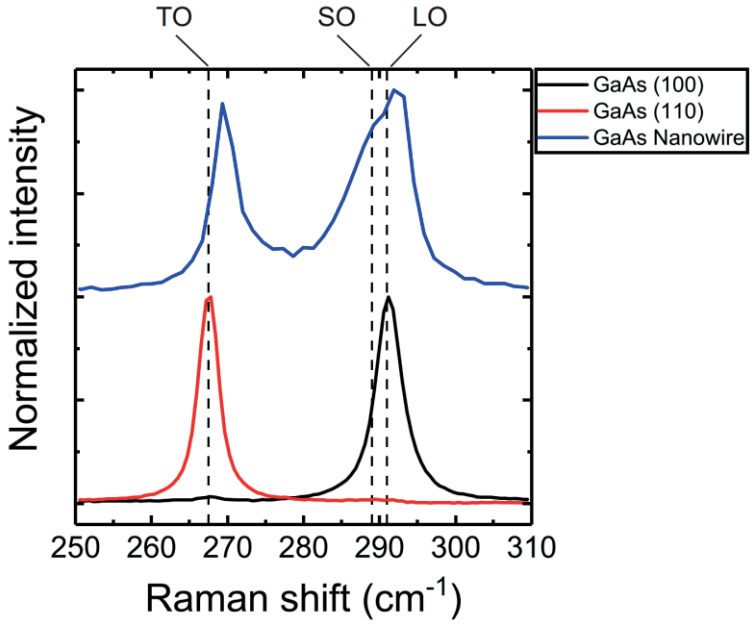

Figure 2.7: Raman spectra of GaAs thin film samples with (100) (black line) and (110) (red line) surface orientations and GaAs nanowire sample grown on Si substrate (blue line). The spectra were obtained at room temperature using a 532 nm laser. The backscattering geometry was used and the linear polarization of the excitation and scattered light were set with similar configuration for each surface orientation. The Raman spectra were measured by the Author (not published).

2.4.2 Surface optical phonons in nanowires

Low-dimensional structures such as NWs enables the investigation of a handful of new phenomena related to confinement effects that would not be possible in their bulk form. For example, in addition to Raman spectroscopy, the high surface-to-volume ratio favors the measurement of surface optical (SO) phonon modes. The

SO modes arise from interfaces between different dielectric functions, and their frequency lies between the TO and LO phonons [47]. Besides the dimensions and properties of the surrounding medium [46], the SO frequency can also depend on the density of defects such as twin planes [48].

In addition, the geometry of the system can also affect the SO properties since at the nanoscale, the boundary conditions can give rise to different electric and polarization properties [47]. In the case of an infinite semiconductor with flat surface, the SO frequency is given by [47]:

$$\omega_{SO} = \omega_{TO}\sqrt{\frac{\epsilon_0 + \epsilon_m}{\epsilon_\infty + \epsilon_m}} \tag{2.7}$$

Where ϵ_0 and ϵ_∞ are the static and high-frequency dielectric constants and ϵ_m is the hard dielectric constant for GaAs . For a cylindrical shaped semiconductor the SO is given by [47]:

$$\omega_{SO}^2 = \omega_{TO}^2 + \frac{\widetilde{\omega_p^2}}{\epsilon_\infty + \epsilon_m f(x)}\ , x = qr \tag{2.8}$$

With

$$f(x) = \frac{I_0(x)K_1(x)}{I_1(x)K_0(x)} \tag{2.9}$$

where $I(x)$ and $K(x)$ are Bessel functions, r is the cylinder radius, $\widetilde{\omega_p^2}$ is the screened ion plasma frequency given by $\omega_{LO}^2 = \omega_{TO}^2 + \widetilde{\omega_p^2}/\epsilon_\infty$. Therefore, Equation (2.8) relates the SO frequency to the surrounding medium dielectric constant and to the NW diameter. Although a cylindrical shape is used for the calculations in Equation (2.8) and the NWs usually have hexagonal shape, it was previously reported a good agreement between experimental points and theoretical data [46]. As illustrated in Figure 2.7, the SO mode centered at 289 cm^{-1} is only present in the Raman spectra of the ~100 nm diameter GaAs NWs analyzed, which is in good agreement with Equation (2.8) as reported in [46].

2.4.3 Coupled Phonon-Plasmon Modes

In doped polar semiconductors, the LO mode couples to the oscillations of the free-carriers producing a coupled phonon-plasmon mode (CPPM) [49–55]. The line-shape analysis of the CPPM provides information on the free-carriers concentration and mobility for *p*- and *n*-type semiconductor materials. In the long-wavelength limit, the total dielectric function of the coupled system is given by [53]

$$\epsilon(\omega) = \epsilon_\infty \left[1 + \frac{\omega_L^2 - \omega_T^2}{\omega_T^2 - \omega^2 - i\gamma\omega} - \frac{\omega_p^2}{\omega^2 + i\Gamma\omega}\right] \tag{2.10}$$

where $\omega_p = 4\pi ne^2/m^*\epsilon_\infty$ is the plasma oscillation frequency of the free-carriers (electrons or holes) with concentration n and effective mass m^*. The fit parameter $\Gamma = e/\mu m^*$ is the damping constant of the plasma oscillation and is related to the relaxation time of the free charge-carriers averaged over all scattering mechanisms. Therefore, the carrier mobility can be calculated from the parameter Γ providing a careful analysis of the CPPM lineshape, as will be later described. The Raman scattering intensity of the CPPM mode can be described by [53]:

$$I(\omega) = A\omega\Gamma_p\omega_p[\omega_{TO}^2(1 + C) - \omega^2]^2/D \tag{2.11}$$

with:

$$\begin{aligned} D = {} & \left[\omega^2(\omega_{LO}^2 - \omega^2) - \omega_p^2(\omega_{TO}^2 - \omega^2) + \gamma\Gamma_p\omega^2\right]^2 \\ & + \left[\Gamma_p\omega(\omega_{LO}^2 - \omega^2) + \gamma\omega\left(\omega_p^2 - \omega^2\right)\right]^2 \end{aligned} \tag{2.12}$$

where ω_{TO} and ω_{LO} are respectively the TO and LO wavenumbers of an undoped reference sample, A is a frequency independent parameter, C is the Faust-Henry coefficient which depends on the material and excitation wavelength [56] and γ is the natural LO mode damping constant. The position and linewidth of the CPPM is strongly influenced by the free-carriers concentration (given by the plasma oscillation frequency) and by the carriers mobility (given by the plasma damping constant).

Figure 2.8 (a) and (b) show the peak positions of the CPPM for *n*-GaAs and *p*-GaAs respectively, calculated using Equations (2.11) and (2.12). The CPPM peak

positions were calculated as a function of the free-carrier concentration (plasma frequency) and obtained for several values of carrier mobility. Two branches of the CPPM are usually observed in *n*-type GaAs: an L+ peak with wavenumber above the LO mode and an L- peak with wavenumber smaller than the TO mode [51, 52]. With increasing free-carrier concentration, the L- branch shifts towards the TO mode while the L+ branch shifts to higher wavenumbers. In *p*-type semiconductors additional features have to be considered on the CPPM analysis and interpretation due to the different nature of the charge carriers. For example, the values of the plasma oscillation frequency in *p*-GaAs is affected by both heavy and light holes which have a combined effective hole mass given by [53]:

$$m_h^* = \frac{{m^*}_{lh}^{3/2} + {m^*}_{hh}^{3/2}}{{m^*}_{lh}^{1/2} + {m^*}_{hh}^{1/2}} \tag{2.13}$$

The different effective masses of the free-carriers contributing to the plasma oscillation in *n* and *p*-type GaAs ($m_e^* = 0.079m_0$ for *n*-GaAs and $m_h^* = 0.385m_0$ for *p*-GaAs) are the main responsible for the changes of the dependence of the CPPM branches with the plasma frequency observed in Figure 2.8. In *p*-type semiconductors, only one overdamped branch of the CPPM is observed with its frequency being in between the TO and LO modes. The way the CPPM shifts from TO to LO with increasing free-hole concentration strongly depends on the hole mobility [50], which is associated to the coupling strength of the free-carrier plasma and the LO mode. In *n*-type GaAs, the effects of the electrons have not been deeply investigated or reported, and a short discussion will be presented later in the Results chapter.

It is clear from the results shown in Figure 2.8 that the peak position of the CPPM is more influenced in the case of *p*-type doping than for *n*-type semiconductors. It is important to note that for small values of Γ (high hole mobility) the CPPM also exhibits two branches L+ and L- but becomes one single branch that shifts from LO to TO mode with increasing free-carrier concentration for higher damping constant values (i.e. smaller mobility). This point will be of high importance when interpreting the fit results of the Raman spectra measured from the *n* and *p*-type GaAs NWs.

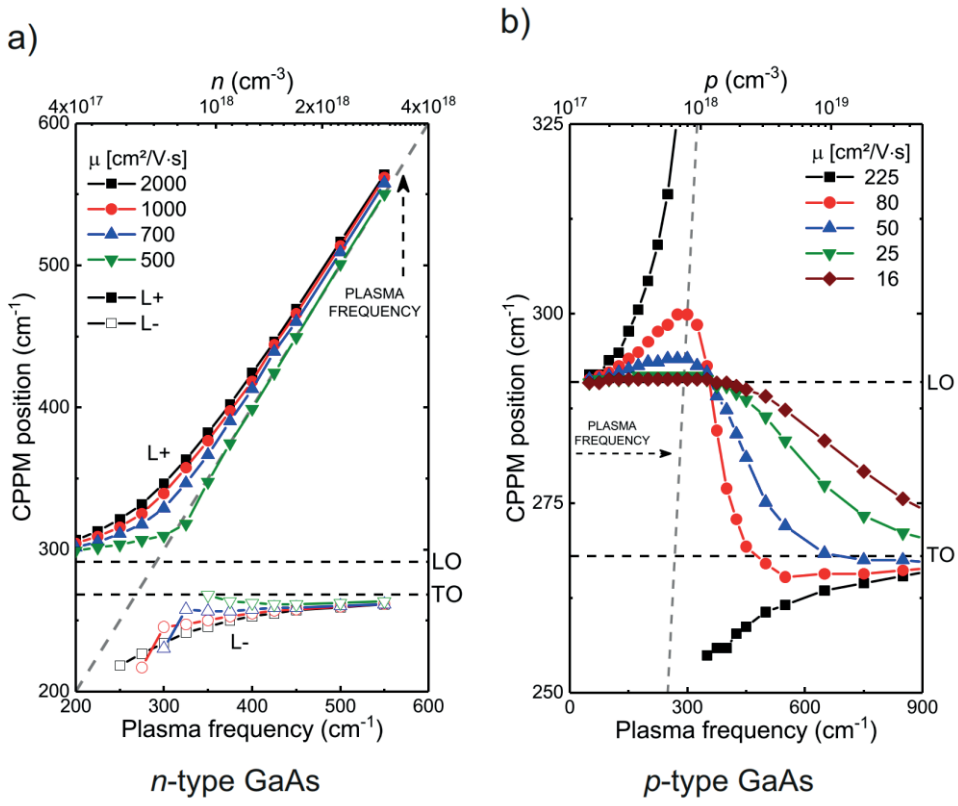

Figure 2.8: Calculated CPPM peak position as a function of the free-carrier concentration and obtained for several values of carrier mobility for (a) n-GaAs and (b) p-GaAs. The gray dashed lines represent the plasma oscillation frequency and the horizontal dashed lines represent the peak position of the LO and TO modes of ZB GaAs.

2.5 Extrinsic optical chirality and circular dichroism

The research carried out in this thesis work involved also the fabrications of new photonic structures based on partially Au-coated NWs, which exhibit extrinsic chirality of optical response. A structure is called to be chiral when it cannot be superimposed with its mirror image. The chiral properties of structures are observed in several natural-occurring systems such as molecules (DNA, proteins, biological organisms) [57]. The geometry of a chiral molecule can determine its physical, chemical and biological properties since it affects the molecular symmetry, length and bond formation. In particular to the optical properties, chiral molecules will exhibit different responses depending on the circular polarization of light [57], which

opens opportunity for the development of applications in the chiral sensing areas. Generally speaking, the figure of merit to quantify the different interaction of a chiral system with left and right-handed circular polarization of light (LCP and RCP, respectively) is called circular dichroism (CD) and can be represented by [57]:

$$CD[\%] = \frac{A_{LCP} - A_{RCP}}{A_{LCP} + A_{RCP}} \times 100 \tag{2.14}$$

where A_{LCP} and A_{RCP} in Equation (2.14) are the optical signals measured in the experiment arising from LCP and RCP light respectively, such as absorption or emission spectra. Often artificial nanostructures are used to replicate the chiral response of natural molecules, but their fabrication might involve rather complex techniques to obtain chiral structures at the nanoscale [57]. However, an overall break of the mirror symmetry can be achieved under the specific experiment geometry, providing a valuable freedom of design for nanoscale structures. This particular concept is known as extrinsic optical chirality. It is important to stress out the fact that extrinsic chiral systems do not have an intrinsic break of symmetry from the material but rather a combined effect of the experiment and the sample geometries.

III-V semiconductor NWs offer waveguide properties with good confinement and manipulation possibilities of electromagnetic fields in the visible and infra-red range. The resonant absorption of NWs is enhanced due to the coupling of incident light to the discrete waveguide modes above the bandgap. In this thesis, the extrinsic chiral properties in the absorption [Publication IV] and photoluminescence emission [Publication V] of GaAs NWs partially covered with Au are discussed.

3 MATERIALS AND METHODS

In this chapter the main experimental techniques used in the thesis are described. A brief introduction of the nanowires growth method used is presented, followed by a description of the nanowire samples investigated. The main aspects of the Raman scattering experiments are presented, such as scattering geometry, excitation wavelength and sample preparation. A description of the main steps for manufacturing of electrical contacts by electron beam lithography is provided. At last, the design and fabrication of the Au-coated NWs samples for extrinsic optical chirality experiments is presented.

3.1 Molecular Beam Epitaxy

All the NWs investigated in Publications I – V were grown using MBE, a physical growth technique of semiconductor materials. The ultra-high vacuum environment achieved inside the MBE growth chamber minimizes the amount of impurities and enables the growth of complex semiconductor heterostructures with atomic layer precision. In MBE growth of semiconductors, optioning sharp interfaces between different compositional layers is enabled by using molecular beams, which can be modulated via fast shutters. In addition, the incorporation of dopant elements can be achieved *in situ*, and with continuous or abrupt changes [21, 25]. The main parameters to be adjusted during MBE growth are the substrate temperature and beam fluxes. The temperature influences the sticking probability and diffusion lengths of the atoms on the growth substrate. The material fluxes mainly dictate the growth rates but also influence on the composition of ternary and quaternary alloys.

3.1.1 Template fabrication for nanowire growth

The NWs used in this thesis were grown by the self-catalyzed VLS mode, as discussed in Chapter 2, on p-Si (111) substrates. The nucleation sites on the Si substrate where NW growth begins are defined by a self-assembled method based

on droplet epitaxy followed by spontaneous oxidation [9]. In this method, Ga droplets are deposited on the oxide-free Si substrate with the possibility to control the density by adjusting the substrate temperature, as shown in step 1 of Figure 3.9. Typical droplets density range from 10^7 to 10^9 cm^{-2} [10, 11], which will determine the NW density after growth depending on the yield [9]. The Ga droplets are then crystallized into GaAs nanocrystals by providing an As_2 flux (step 2). Subsequently, the substrate is then let to oxidize overnight in air atmosphere (step 3). By properly cleaving the Si (111) substrate, it is possible to grow 6 different NW samples from the same template. This means that any effect related to NW density or catalyst droplets morphology can be excluded since they will be the same for all set of samples.

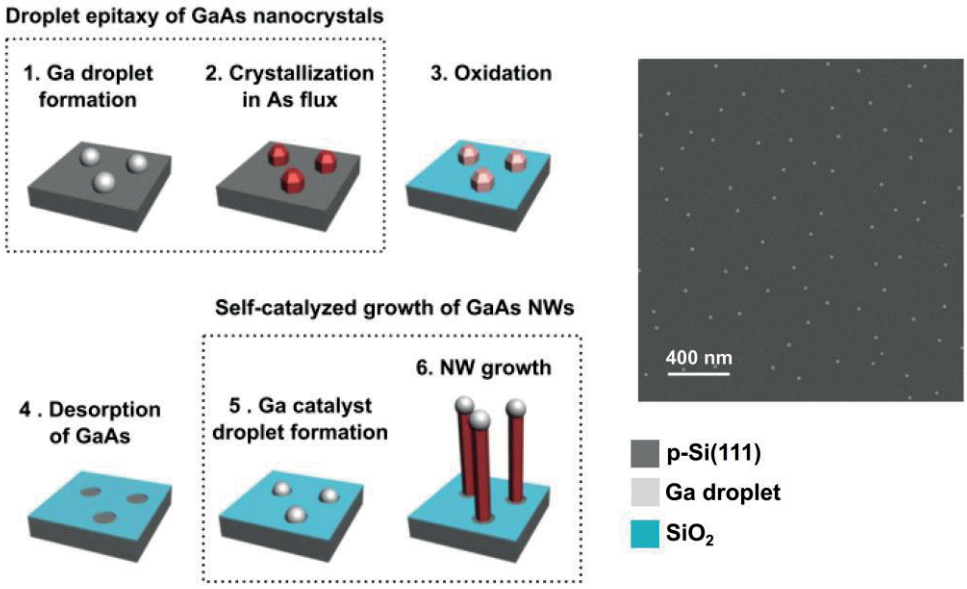

Figure 3.9: Steps of NW growth by self-catalyzed mode on lithography-free oxide patterns. The SEM figure shows the Ga droplets deposited on Si substrate. Adapted from [9].

3.1.2 Nanowire growth

After the template fabrication on Si substrates described in the previous section, the next step is to load the Si substrates back to the MBE chamber and perform a heat treatment to evaporate the GaAs nanocrystals, which leaves exposed Si substrate areas in the oxide layer (step 4 of Figure 3.9). These patterns will act as the nucleation

sites for the NW growth, where the catalysts droplets will be formed by deposition of Ga with size limited by the opening diameter (step 5). The NW growth (step 6) is initiated by providing As_2 with the proper V/III beam equivalent pressure (BEP) depending on the targeted NW properties (growth rate, composition, etc.). It is very important to keep a good knowledge and control of the Ga and As fluxes to determine the adequate growth rate during NW growth. The flux calibration for determining the group III growth rate is usually carried for planar GaAs (100) growth direction based on the number of monolayers deposited in this crystalline direction. However, the ZB phase of GaAs NWs grow in the (111) direction and therefore will have a different growth rate than the calibration determined for planar GaAs growth [25]. The NW growth is terminated by simultaneously switching off all fluxes and rapidly cooling down the substrate.

The doped NW samples were grown by providing a dopant flux simultaneously with the Ga and As fluxes. The Be and Te doped GaAs NWs investigated in this thesis work were grown with a V/III BEP of 9. For *p*-type GaAs NWs, Beryllium (Be) flux corresponding to nominal dopant concentration of 2×10^{18} cm^{-3} or 2×10^{19} cm^{-3} in case of planar growth was used. To obtain *n*-type GaAs NWs, a GaTe flux was used as source of Te dopant with nominal doping level of 2×10^{19} cm^{-3}, as calibrated for planar growth. For either *p* or *n*-type GaAs NWs, the nominal doping level was determined based on Hall Effect measurements of Be- or Te-doped planar GaAs samples grown on semi-insulating GaAs (100) substrates (Publication I and Publication II). Table 1 summarizes the sample code (ID) of the NWs used and the corresponding relevant growth parameters.

Table 1. Description of the relevant growth parameters of the nanowire samples investigated.

Sample ID	Nanowire Density (cm^{-2})	Growth Temperature (°C)	Ga flux (μm/h)	Growth Time (min)	Dopant	Nominal doping (cm^{-3})
***p*-type**						
Ref1	2×10^{8}	640	0.3	60	-	-
Be1	2×10^{8}	640	0.3	60	Be	2×10^{18}
Be2	2×10^{8}	640	0.3	60	Be	2×10^{19}
***n*-type**						
Ref2	4.4×10^{7}	640	0.3	80	-	-
Te1	4.4×10^{7}	640	0.3	60	Te	2×10^{19}

3.2 Raman spectroscopy

In Publication I and Publication II we used Raman spectroscopy to investigate the structural properties, surface optical phonons and to estimate the free-carrier concentration and carriers mobility in the undoped, *p*-type and *n*-type NWs. Raman spectroscopy of the undoped and doped GaAs NWs was performed at room temperature in the backscattering geometry described in Chapter 2.4. All the Raman spectra analyzed in this thesis were obtained from single NW. The *p*-type set of NW samples (Ref1, Be1 and Be2 in Table 1) investigated in Publication I were measured using a 532 nm excitation wavelength and a 50× magnification lens (NA = 0.82) was used to obtain a spot of <1 μm in diameter. For this setup, the NWs were harvested from the growth substrate and dispersed in isopropyl alcohol (IPA) followed by sonication, and then drop-casting the NW+IPA solution on a Si substrate with a 200 nm SiO_2 thermal oxide layer. Accordingly, we measure backscattering from x = {110} surface orientation of the NWs sidewalls and the linear polarization of

the excitation and scattered light can both be adjusted in relation to the NW radial direction y = {112} and growth direction z = {111}. In order to estimate the dopant concentration and carrier mobility from Be-doped GaAs NWs by analysis of the CPPM described in Chapter 2.4, the linear polarization of both excitation and scattered light were set perpendicular to the NW growth axis. In the Porto notation, this is represented as $x(y,y)\bar{x}$. The sub-micrometer spot size used in the Raman experiments allowed a spatially resolved analysis of the CPPM (and therefore, dopant concentration) along the NW growth direction.

The *n*-type GaAs NWs set of samples (Ref2 and Te1 in Table 1) investigated in Publication II were measured in a confocal Raman microscope equipped with a 100× (NA=0.85) objective lens, providing a spot size of <1 μm in diameter of a 532 nm excitation laser. The small NW density on the growth substrate combined with the sub-micrometer spot size used made it possible to measure backscattering Raman spectra of the as-grown NWs. In this way the backscattering from x = {111} surface of the standing NWs was measured with the linear polarization of excitation set perpendicular to the NW axis and the scattered intensity was unpolarized. Spatially resolved Raman spectra along the NW axis were obtained by adjusting the vertical position of the piezo stage of the Raman microscope. The intensity of the Si optical Raman mode (~520 cm^{-1}) arising from the growth substrate was used as reference for determining the stage position corresponding to the NW bottom part.

3.3 Device processing

The electronic transport properties of the Be- and Te-doped GaAs NWs were investigated in Publication I, Publication II and Publication III. To fabricate electrical contacts, the single NWs were harvested from the growth substrate and transferred to a *p*-GaAs substrate covered with a 200 nm SiO_2 layer. The substrate to where the NWs were transferred was pre-patterned by UV-lithography with Ti/Au pads for connecting the probes used for IV measurements and also with several marks to assist on localizing single NWs as will be described. The main steps for contact manufacturing are defining the contacts areas by electron beam lithography (EBL), surface treatment of the exposed contact area, deposition of the metallic multilayers acting as contacts, and thermal annealing of the contacts after device processing. Each of these steps will be discussed with further details.

3.3.1 Electron beam lithography

EBL is a common lithography procedure to define structures and patterns on a substrate that will be further processed, for example by chemical/dry etching or depositing metallic layers. One advantage of EBL over standard photolithography techniques lies in the shorter wavelength of electrons when compared to the UV light, for example. In relation with NWs, EBL is convenient since it allows easier identification of the position of the NWs transferred to the substrate on top of which the electrical contacts will be fabricated.

The main steps used in EBL are show in Figure 3.10. An electron sensitive polymer (resist) is spin coated on the processing substrate and baked in a hot plate, with the possibility to select the resist thickness by adjusting the coating spinning speed and time. The sample is then loaded in an electron microscope equipped with the proper EBL tools (hardware and software) and only the selected areas defined by a pattern designed using a CAD software are exposed by the electron beam. Two types of EBL resist are commonly used: positive and negative. The exposed areas of a positive resist will be removed after resist development, leaving the substrate exposed for further processing steps. For negative resists, the areas that exposed by the electron beam will not be removed after resist development, therefore leaving all the other regions of the substrate exposed. In this work it was only positive EBL resists. In this thesis only positive EBL resist was used.

The sample is then unloaded from the SEM and the resist is developed in a MIBK:IPA solution, which removes the areas of the positive resist that was exposed to the electron beam. After this step, the NW sidewalls are exposed and an oxide removal and surface passivation steps are performed, as will be later discussed in the text. The following step is to load the sample in the e-beam metal evaporation to deposit the metallic multilayers, which will depend on the doping type of the NWs. At last, the sample is dipped in acetone in order to remove the remaining resist and leaving only the patterned area with the metallic multilayers acting as electrical contacts.

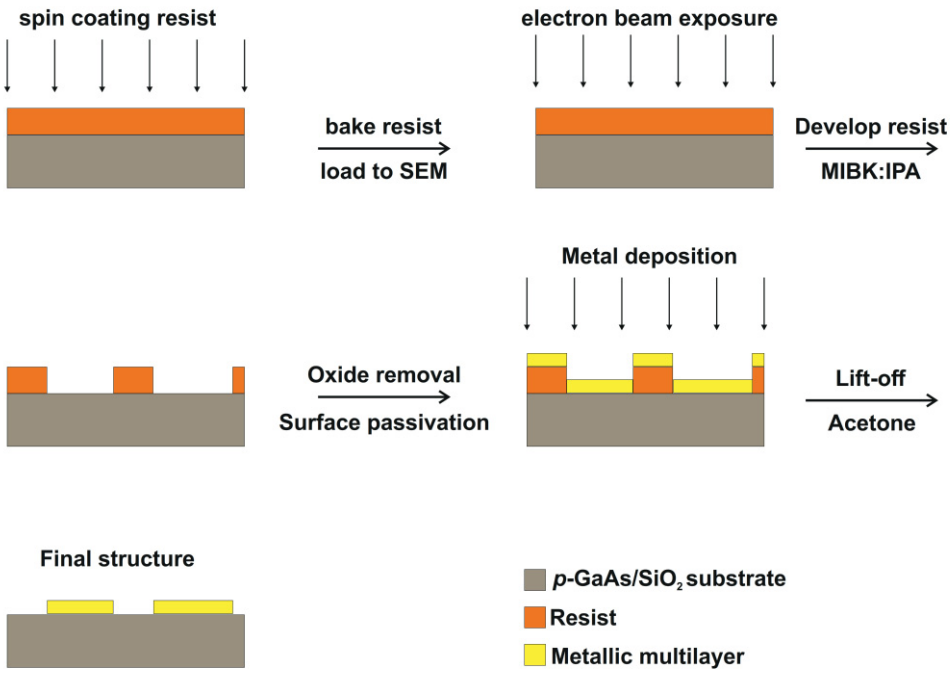

Figure 3.10: Schematics of the main steps in electron beam lithography using a positive e-beam resist.

3.3.2 Electrical contact processing

The key processing parameters to be considered and optimized when fabricating electrical contacts onto semiconductor materials are: (1) removal of the surface native oxide, (2) surface passivation at the metal-semiconductor interface, (3) deposition of metallic layers, and (4) thermal annealing [58, 59]. Usually the choice of the metallic multilayer is of importance to provide low contact resistance and thermal stability. In this thesis, different combinations of the steps (1)-(4) were designed to determine the processing steps that would yield the best IV performance and linear behavior, i.e., aiming to achieve Ohmic contacts on the NWs. The majority of the literature for Ohmic contacts fabrication on GaAs was based on thin films and bulk structures with (100) surface orientation, while the self-catalyzed growth of GaAs NWs results in (110) surface orientation at the sidewalls. The surface orientation influences the electronic states [60], and therefore the interface

properties, Schottky barrier heights [61–63] and even the crystallization dynamics of the deposited metal films.

3.4 Transport characterization

In Publication I and Publication II the transport properties of the *p*-type and *n*-type GaAs NWs were investigated to obtain complementary information to Raman experiments on the distribution of Be and Te dopants along the NW axial direction. In Publication III the transport characterization was used to optimize the processing parameters of electrical contacts to *p*-type GaAs NWs. The IV properties of the Be and Te-doped NWs were measured at room temperature using a two-probe configuration. In order to identify possible spatial dependences of the transport properties of individual NWs, several evenly spaced contacts (same channel length) were fabricated along the NW axis and the IV of each channel was analyzed individually. For the processing steps that resulted in Ohmic contacts on the NWs, an additional sample was prepared in the transmission line model (TLM) geometry to obtain information of the contacts specific resistance and the semiconductor resistivity.

In the TLM samples, the contacts are fabricated with increasing channel length and the IV from each channel is measured. The total resistance R_T from each channel (nanowire and contacts) is analyzed as a function of the channel length (L) in order to obtain the NW resistivity ρ_S and the transfer length L_T by fitting the experimental points (R_T,L) [64, 65] :

$$R_T(L) = \frac{\rho_S}{\pi r^2}\left(2L_T \coth\left(\frac{W_C}{L_T}\right) + L\right) \tag{3.1}$$

where W_C is the contact width and r is the NW radius. Usually, a linear fit of the (R_T,L) points is used, but in this case Equation (3.1) was chosen to account for the reduced contacts used in our experiments [64]. The specific contact resistance (ρ_C) can be obtained from:

$$\rho_C = \frac{3}{2}\frac{\rho_S}{r}L_T^2 \tag{3.2}$$

3.5 Complementary experimental techniques

In this sub-section, we describe several other complementary experimental techniques that have been employed at external sites and collaborators. The results obtained with these techniques were instrumental for the interpretation of the data obtained using experimental techniques we deployed in our laboratory.

3.5.1 Transmission electron microscopy

In transmission electron microscopy (TEM) a coherent and collimated beam of high energy electrons is incident on the sample to be investigate. These electrons can be absorbed, scattered or transmitted by the sample, and the proper treatment of the data obtained from the electrons after interacting with the crystal can provide valuable information of the crystalline structure and composition of the material with possibility of sub-nanometer spatial resolution.

TEM characterization was used in Publication I and Publication II to evaluate the effect of Be and Te dopants incorporation on the structural properties of self-catalyzed GaAs NWs. In Publication V, a cross-section TEM image from a GaAs/AlGaAs NW partially covered with Au was obtained to show the formation of the Au layer on the sidewalls and the overall structure of the core-shell NW. The NWs investigated by TEM in Publication I and Publication II were harvested from the growth substrate and transferred to the copper grids with thin carbon films which were loaded into the transmission electron microscope. Bright-field (BF) images are obtained by comparing the contrast between the electrons that are transmitted by the sample and the ones that are not. High-resolution TEM (HR-TEM) images are obtained by increasing the magnification significantly and selecting a smaller region to be scanned at the sample. This enables the analysis of how the atomic planes are stacked along the NW axis and evidences the presence of twin planes and stacking faults. When imaging in HR-TEM mode, it is also possible to record the selected-area electron diffraction (SAED) pattern, which gives information of the local crystalline lattice in similar way as X-rays diffraction.

3.5.2 Off-axis electron holography

Off-axis electron holography is a TEM technique that spatially measures the phase difference ($\Delta\varphi$) that originates from the interference of the electrons when

transmitted through the sample and the electrons that do not interact with the sample, named object and reference waves respectively. The phase difference between object and reference wave after interacting with a sample of thickness H will depend of the sum of the crystalline potential over H, which can be summed as a mean inner potential (MIP) and a built-in potential V_{BI} by the relation:

$$\Delta\varphi = C_E H(V_{BI} + MIP) \tag{3.3}$$

where C_E is a constant that depends on the acceleration voltage used in the electron microscope. The V_{BI} gives information of the active doping in semiconductor materials.

In this thesis work, cross-sectional slices from the bottom and tip regions of Te1 NWs with an undoped AlGaAs shell were obtained by focused ion beam (FIB) cut and the MIP and V_{BI} values were obtained for both slices. The results are discussed in this thesis and with more details in Publication II.

3.5.3 Atom probe tomography

In atom probe tomography (APT), ions are formed by thermal pulses from a laser or field pulses from a voltage pulser, and then removed from the surface of the NWs by a dc electric field. After evaporation from the sample, the ions are projected onto a detector. The 3D reconstruction of the atoms composing the sample can be made based on the arrival time and position of each ion on the detector. In Publication II, Te-doped GaAs NWs and *n*-GaAs/*i*-AlGaAs core-shell NWs were measured by APT. The core-shell NWs were measured in order to increase the field of view provided by the APT, which is limited to a solid angle covering around 1/8 of a sphere.

3.5.4 Photo-acoustic spectroscopy

In Publication IV, Photo-acoustic spectroscopy (PAS) was used to investigate the extrinsic optical chirality in terms of the absorption properties of GaAs/AlGaAs NWs partially covered with Au. The working principle of PAS relies on the thermal expansion of a sample that results from the generated heat when the samples absorbs an incoming light beam. By modulating the intensity of the incident excitation over time, the continuous heating and cooling down process will create an acoustic wave

due to the periodic pressure changes caused by the thermal expansion and contraction of the analyzed sample. This acoustic wave signal is then collected by a microphone and converted into electrical signals. Therefore, the PA signals measured over continuous range of excitation wavelengths will give as a result the absorption peaks of that sample. Owing to its scattering-free properties, PAS is a convenient technique to investigate the absorption spectra of nanowires, plasmonic nanoparticles and metasurfaces. A comprehensible description of the PAS experimental setup is presented in Publication IV and in Ref [66].

The geometric parameters of the Au-coated GaAs/AlGaAs core-shell NWs investigated in Publication IV and Publication V are summarized in Table 2:

Table 2. Geometric parameters for the Au-coated GaAs/AlGaAs investigated in Publication IV and Publication V

Sample	L [nm]	D [nm]	T_{AlGaAs} [nm]	T_{GaAs} [nm]	T_{gold_1} [nm]	T_{old_2} [nm]
S1	4750 ±34	138 ± 5	3.5	0.7	20	10
S2	5190 ± 64	151 ± 5	8.6	1.7	20	10
S3	4600 ± 52	165 ± 6	11.7	5.8	20	10

4 RESULTS AND DISCUSSION

In this chapter, the main results of the structural, optical and transport properties of the undoped, Be and Te-doped GaAs NWs investigated in this thesis are presented. The chapter is divided in 3 subsections: the first and the second are dedicated to Be and Te-doped GaAs NWs, respectively. The experimental results from TEM analysis, Raman spectroscopy and IV measurements are combined to evaluate the dopant incorporation mechanisms for each case. Additional experimental results originating from international collaborations are used to corroborate the findings for Te-doped NWs. The third section briefly presents the results of partially covering GaAs and GaAs/AlGaAs nanowires with Au and its effect on the absorption and photoluminescence properties.

4.1 Be-doped GaAs nanowires

As previously described in Chapter 3.1.2, the incorporation of Be as *p*-type dopant in self-catalyzed GaAs NWs was investigated in Publication I. Two different NW samples with nominal doping levels of 2×10^{18} cm^{-3} (Be1) and 2×10^{19} cm^{-3} (Be2) were grown. In addition, a reference sample (Ref1) was also grown using the same template as described in Chapter 3.1.1. The nominal doping levels were determined based on Hall measurements of MBE grown Be-doped GaAs (100) planar layers and are listed in Table 1. The effects of Be incorporation on the structural properties of the GaAs NWs was investigated by transmission electron microscopy (TEM). The spatial dependence of the Be concentration and hole mobility along the NW axis was determined by analysis of the CPPM measured by Raman spectroscope. Finally, the IV analysis of single–NW devices provided further details on the dopant distribution. In addition, the optimization of the electrical contact properties by adjusting the processing parameters was also developed in Publication III.

4.1.1 Structural properties

The influence of Be-dopant incorporation in the structural properties of the GaAs NWs was investigated by HR-TEM imaging and SAED analysis. Figure 4.11 summarizes the results from representative Ref1, Be1 and Be2 NW samples. The undoped NWs (Ref1) presented an increasing twin plane density towards the NW/droplet interface as can be seen from the bright-field (BF) TEM image in Figure 4.11(a), which is ascribed to the change in the contact angle between the NW tip and Ga droplet during lateral growth in Publication I and in Ref [10]. The analysis of the HR-TEM images and the SAED patterns from Ref1 sample shows that the undoped NWs are composed from twinned ZB structure at the root region, followed by a defect-free, 2 μm long, ZB GaAs at the center region and ending with a short WZ section (~5 nm) at the interface of the Ga droplet and the NW. The formation of the WZ section in this region is typically observed in self-catalyzed GaAs NWs due to the sudden changes in the growth conditions when switching off the Ga and As fluxes and ramping down the sample temperature, resulting in a decrease of the droplet contact angle [10].

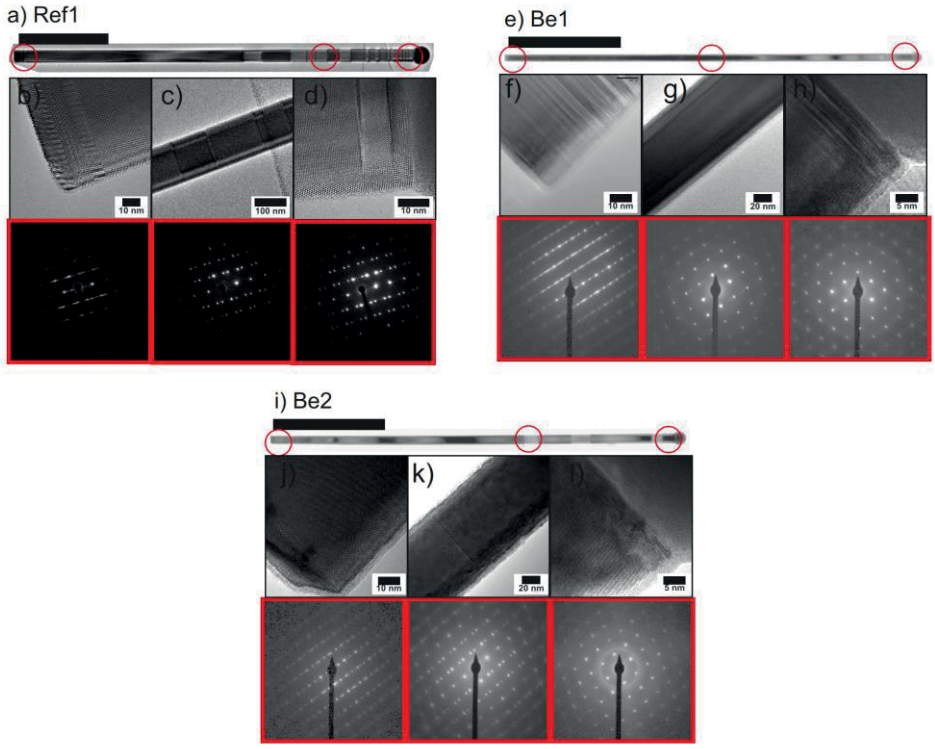

Figure 4.11: HR-TEM images and SAED patterns of (a)-(d) Ref1, (e)-(h) Be1, and (i)-(l) Be2 NWs. The red circles in (a), (e) and (i) indicate the different positions corresponding to the higher magnification images in (b)-(d), (f)-(h) and (j)-(l). The scales bars are 1 μm in (a), (e) and (i). The other scale bars sizes are indicated on each figure. Adapted from Publication I.

The addition of Be into the GaAs NWs resulted in an overall decrease of the twin planes formation along the NWs as can be seen from the BF images of Be1 and Be2 in Figure 4.11(e) and Figure 4.11(i) respectively. In addition, the NWs are composed of ZB GaAs and no evidence of WZ was observed from the SAED patterns. It has been previously reported that Be suppresses both the twin plane and WZ phase formation in self-catalyzed growth of GaAs NWs [29, 67]. The relatively high density of twin plane at the root regions of Be1 and Be2 NWs is due to early-stages of the NW growth prior to the stabilization of droplet contact angle and composition. The contact angle between the Ga droplet and the NW also affects the formation of twin planes and WZ segments in self-catalyzed GaAs NWs [68–70]. However, SEM analysis of Ref1, Be1 and Be2 NWs measured from post-growth conditions revealed a negligible variation in the contact angle between the Ga droplet and the NW samples. Therefore, the suppression of twin planes formation and absence of WZ

phase can be ascribed to a change of the energetics in the VLS system due to the incorporation of Be-dopant.

4.1.2 Raman spectroscopy

As previously discussed, spatially-resolved Raman spectroscopy was used to estimate the dopant concentration and hole mobility in single Be-doped GaAs NWs via analysis of the CPPM line-shape, as described by Eqs. (2.11) and (2.12). The Raman spectra obtained from the center region of single NWs of Ref1, Be1 and Be2 samples are shown in Figure 4.12. The decomposition of the experimental data in Lorentzian peaks from Ref1 reveals the TO, SO and LO modes of ZB GaAs centered at 268, 272 and 288 cm^{-1}, respectively. The position and linewidth of the TO modes from Be1 and Be2 NWs are consistent with the Ref1 sample. The SO position may depend on the NW diameter and density of twin planes [46, 48] and are in accordance with the HR-TEM results in Figure 4.11. In addition, the CPPM lineshape analysis shows a Be-dopant concentration and hole mobility of $p = 1.2 \times 10^{18}$ cm^{-3} and $\mu = 70\ cm^2/V \cdot s$ for Be1, and $p = 1.1 \times 10^{19}$ cm^{-3} and $\mu = 13\ cm^2/V \cdot s$ for Be2 NW.

The reliability of the fit method used to estimate the free-carrier concentration and hole mobility in Publication I was evaluated by measuring Raman scattering of Be-doped GaAs (100) thin film samples and comparing the fit results with Hall effect data. The free-carrier concentration obtained from Raman spectroscopy was in good agreement with the Hall measurement data, whereas there was a clear underestimation of the hole mobility by Raman spectroscopy technique. This is due to the contribution of several scattering mechanisms that cause an apparent decrease of the hole mobility when estimated by Raman spectroscopy, such as non-polar optical and acoustic phonons, polar optical phonons and ionized impurities [49, 71]. This effect was also previously reported for Zn-implanted GaAs [50] and *p*-type GaP [54].

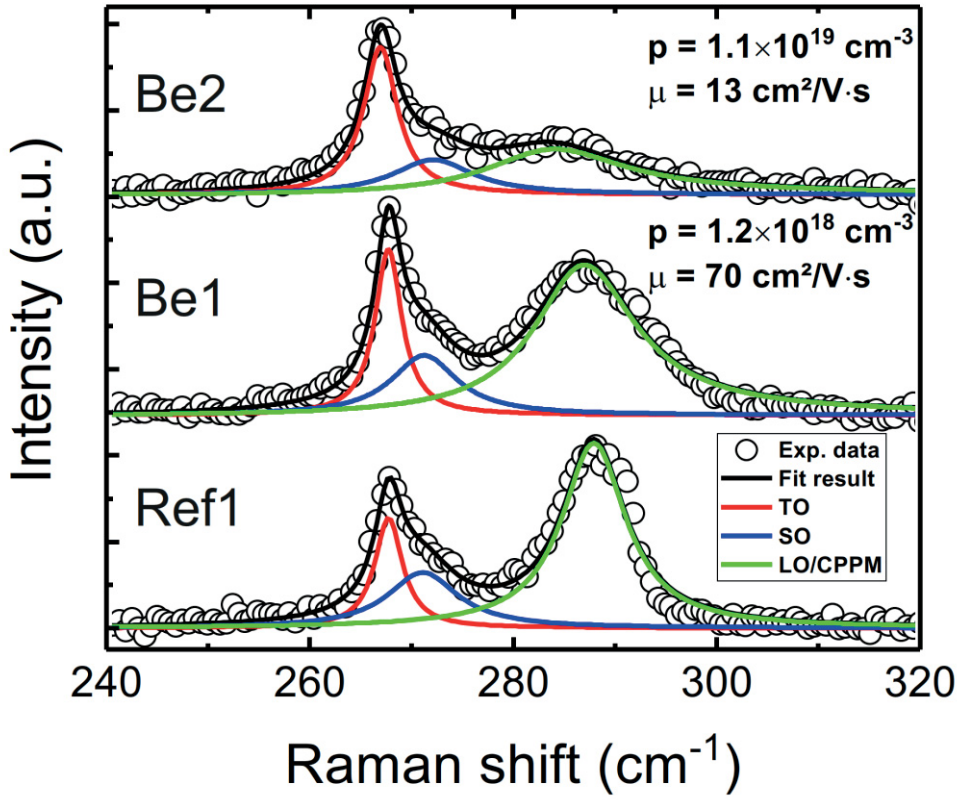

Figure 4.12: Raman spectra of the center region of representative Ref1, Be1 and Be2 NWs. The open circles represent the experimental points. The color-dashed lines represent the spectral decomposition of TO, SO, LO/CPPM peaks and the solid black line the total fit result. The Be-concentration and holes mobility determined by the CPPM lineshape analysis of Be1 and Be2 NWs are indicated.

In order to identify any possible gradient of Be-dopant concentration in *p*-GaAs NWs, Raman spectra were measured from three different positions along the axis of three representative NWs from each sample, and the CPPM line shape analysis was performed. The results of carrier concentration and hole mobility from Be1 and Be2 NW samples are presented in Figure 4.13. An SEM image of a representative NW showing the positions from where the Raman spectra were obtained is also shown on the right side of the same figure.

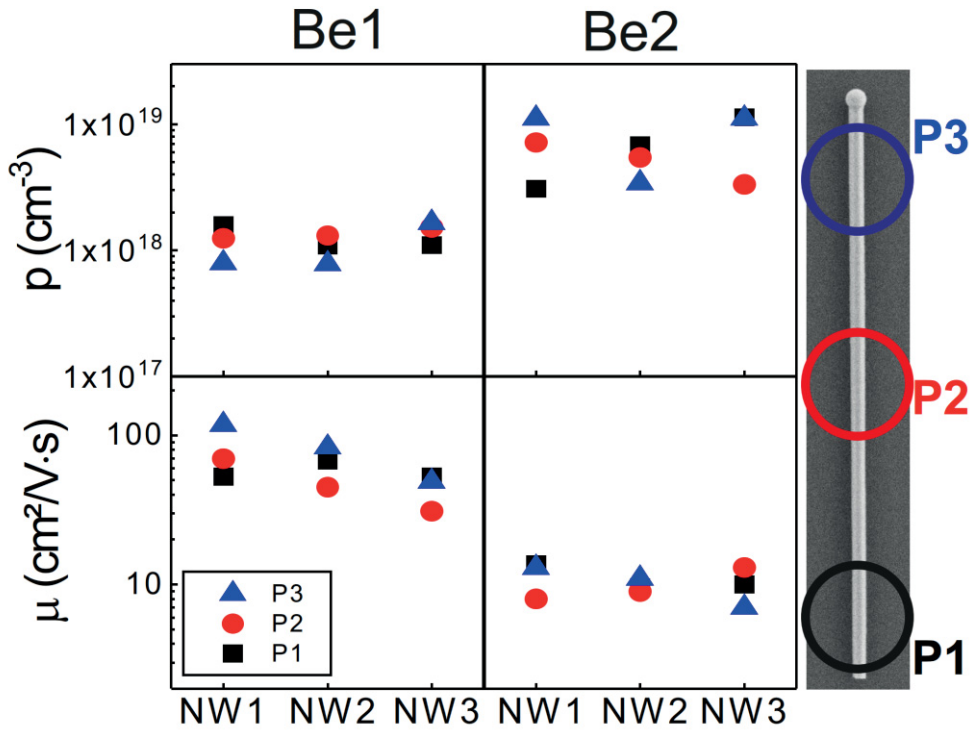

Figure 4.13: Hole concentration and mobility obtained from the fit of CPPM line shape to the Raman spectra for three different NWs from Be1 and Be2 samples. The symbols represent the different positions of the NWs from which the Raman spectrum was measured, as indicated in the SEM image of a representative NW shown on the right side: bottom region (P1), center region (P2) and tip region (P3). Adapted from Publication I.

The Be-dopant concentration estimated by Raman spectroscopy ranges from 8×10^{17} to 1.6×10^{18} cm^{-3} for Be1 NWs and from 3.4×10^{18} to 1.1×10^{19} cm^{-3} for the Be2 NWs. The results in Figure 4.13 do not indicate any consistent gradients of the Be-dopant concentration either along the Be1 or Be2 NW axis, but it is worth noticing that there is a rather large variation of the values obtained for each axial position. This spreading of the values of dopant concentration arise from the uncertainty in performing the spectral decomposition of the overlapped TO, SO and LO/CPPM peaks from GaAs NWs. The CPPM peak gets broader and shifts to frequencies closer to the TO mode of ZB GaAs with increasing carrier concentration [50], which further complicates the CPPM line shape analysis in which Eq. (2.11) is used as component for spectral decomposition. Regardless, the fit results were still consistent with the method applied to the thin film samples supported by Hall data.

One interesting fact to be observed from the Raman spectroscopy results is the efficiency of the Be-dopant incorporation into the GaAs NWs, when comparing the free-carrier concentration obtained from the CPPM line shape analysis shown in Figure 4.13 and the nominal dopant concentrations used for the NW growth: 2×10^{18} cm^{-3} for Be1 and 2×10^{19} cm^{-3} for Be2 sample. On average, the Be1 NWs show 60% of the nominal doping level while only 35% of the nominal doping level was observed for Be2 NWs. A similar efficiency has been previously reported for Be-doped self-catalyzed GaAs NWs [18]. This could be explained by the different Be incorporation rates between (100)-oriented GaAs samples, measured by Hall Effect and used for calibrating the Be-fluxes, and the VS incorporation at the (110) oriented NW sidewall or the VLS incorporation mechanism through the droplet [15, 29, 30]. In addition, the different efficiencies in Be-dopant incorporation observed for Be1 and Be2 NWs suggest that the incorporation efficiency depends on the Be flux during NW growth.

4.1.3 Optimization of electrical contacts properties to *p*-GaAs nanowires

High-quality and reliable electrical contacts at the metal-semiconductor interface are important requirements on the fabrication of semiconductor electronic and optoelectronic devices. As described in Chapter 3.3, the main steps to optimize when fabricating electrical contacts to semiconductor materials are the (1) removal of the surface native oxide, (2) passivation of the surface states at the semiconductor-metal interface, (3) deposition of metallic layers acting as the electrical contacts, and (4) thermal annealing [58, 72]. In order to investigate the electronic transport properties of Be1 and Be2 NW samples by the methodology presented in Chapter 3.4, we needed to deposit Ohmic contacts on the NW sidewalls.

To this end, in Publication III five distinct processes combining different parameters of steps (1)-(4) were developed. This allowed the determination of the individual contributions of each parameter in the resulting contact resistance of the Be-doped GaAs NWs: (1) the native oxide removal was done by either a 2.8% NH_4OH or 3.7% HCl diluted in H_2O, followed by H_2O rinsing; (2) The surface passivation prior to metal deposition was done by a 15% solution of $(NH_4)_2S_x$ (Ammonium Polysulfide) diluted in H_2O and heated at 45 °C, followed by H_2O rinsing; (3) The metallic multilayers deposited were either Ti/Pt/Au (20/20/200 nm) or Pt/Ti/Pt/Au (5/10/10/200 nm); (4) A rapid thermal annealing (RTA) of 400 °C for 30 s was used for the Pt/Ti/Pt/Au multilayer. For each processing sample, 4

evenly spaced electrical contacts were fabricated along the NW to identify possible changes in the IV behavior, which would indicate gradients of Be-dopant concentration along the NW. For the optimization of the electrical contacts, the Be2 NW was chosen since the higher doping level results in a smaller depletion layer width, thus facilitating the formation of Ohmic contacts. The different processing parameters used for each sample (P1-P5) are summarized in Table 3. In addition to the steps (1)-(4), an oxygen plasma cleaning after developing the resist and prior to oxide removal of the NW sidewalls was performed in sample P2 to evaluate the possible effects of the additional surface defects that may arise from oxygen plasma exposure [73].

Table 3. Fabrication details of electrical contacts to Be-doped GaAs NWs. Adapted from Publication III.

Process#	Oxygen plasma	Oxide removal	Surface passivation	Metal layers	RTA
P1	-	$NH_4OH:H_2O$	-	Ti/Pt/Au	-
P2	Yes	$HCl:H_2O$	$(NH_4)_2S_x$	Ti/Pt/Au	-
P3	-	$HCl:H_2O$	$(NH_4)_2S_x$	Ti/Pt/Au	-
P4	-	$HCl:H_2O$	$(NH_4)_2S_x$	Pt/Ti/Pt/Au	-
P5	-	$HCl:H_2O$	$(NH_4)_2S_x$	Pt/Ti/Pt/Au	400 °C, 30 s

The IV characteristics from samples P1-P5 are summarized in Figure 4.14(a). The Ohmic character of the electrical contacts was qualitatively evaluated by the IV linearity. All the analysis of the process parameters on the contact properties were based on the IVs measured from the center region of the Be2 NWs (BC contacts in Figure 4.14(b)). The nonlinear behavior of the IVs for P1 to P4 are characteristic of Schottky-like contacts with similar barrier heights for each contact [74]. Process P1 was developed as a typical Ohmic contact manufacturing protocol for planar *p*-GaAs

(100), but it clearly does not yield the same results when applied to the (110)-oriented surface of GaAs NWs sidewalls. The Ohmic character of the IVs was greatly enhanced in P4, when compared to P1-P3, by adding a 5 nm Pt layer under the Ti/Pt/Au multilayer. The IV further approached to linear behavior by performing an RTA at 400 °C for 30 s in P5, as can be seen in Figure 4.14(a).

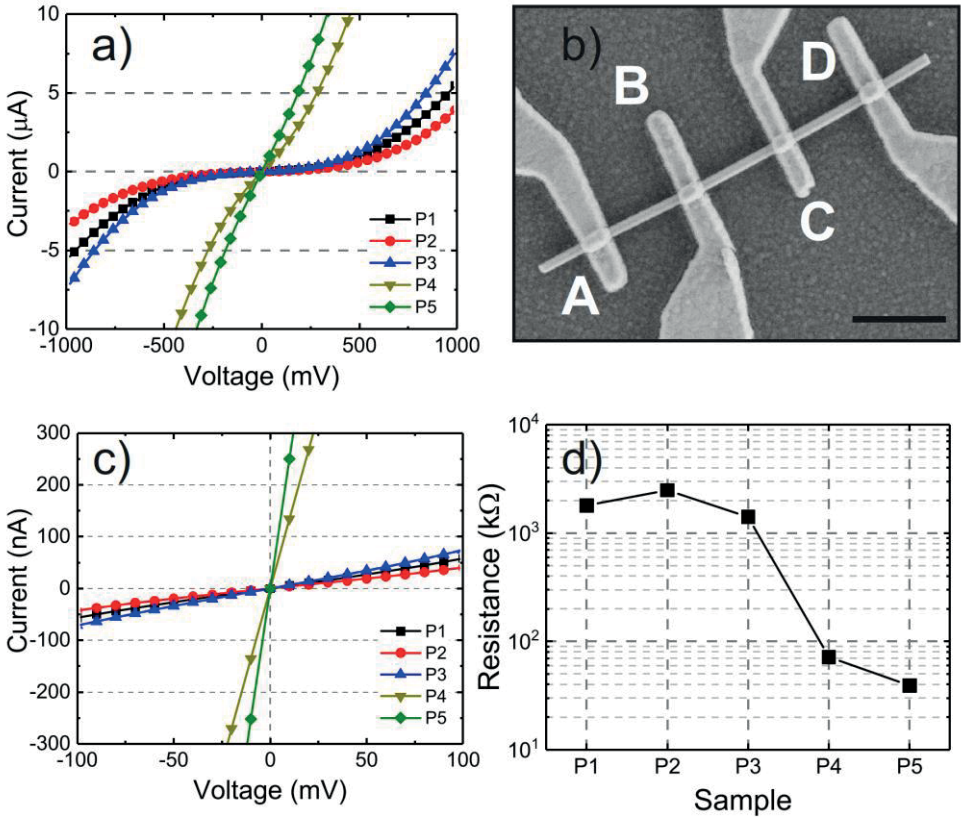

Figure 4.14: (a) IV from the center region of Be2 NWs with electrical contacts fabricated using process P1-P5 as described in Table 3. (b) SEM image of a representative Be2 NW with four evenly spaced contacts. The scale bar is 1 μm. (c) IV from P1 to P5 in the 100 mV applied voltage range. (d) Total channel resistance obtained from the linear fit of the IVs in the bias range displayed in (c). Adapted from Publication III.

To further quantify the effects of the processing parameters on the contact properties, the IV from samples P1-P5 are shown in a 100 mV bias range in Figure 4.14(c). In this smaller bias range, the IVs exhibit linear behavior and are mainly governed by the contact resistance [74]. The linear fit of the IVs in this bias range gives the total channel resistance (NW + contacts) and any changes of the total

resistance were ascribed to the contact resistance. This was possible owing to the small wire-to-wire variation in the dopant concentration as was observed in Publication I and the fact that all the investigated NWs have similar diameter. The total resistance from P1-P5 are shown in Figure 4.14(d). The increase in resistance of P2 compared to P1 and P3 indicates the detrimental effect of the oxygen plasma treatment previously discussed. A great reduction of the total resistance from 1400 kΩ to 72 kΩ from P3 to P4 was achieved by depositing the additional Pt layer prior to the Ti/Pt/Au multilayer used in samples P1-P3. The total resistance was further decreased from 72 kΩ to 40 kΩ by rapid thermal annealing (RTA) of the contacts in P5. The improvement of the contact properties in P4-P5 compared to P1-P3 was ascribed to the higher degree of crystallinity of Pt when deposited directly to GaAs (110) surface in comparison to Ti. These findings were confirmed by grazing incidence x-ray diffraction measurements of Ti, Pt and Pt/Ti thin films deposited on GaAs (110) substrates. More details of the structural characterization of the Ti, Pt and Pt/Ti thin films on GaAs (110) substrates are presented in Publication III.

4.1.4 Transport characterization

The process P5 developed in Publication III was used to fabricate the electrical contacts onto the Be1 and Be2 NW samples described in Publication I. The spatial dependence of the IV characteristics from individual Be-doped NWs was possible by manufacturing four evenly spaced contacts along the NWs and comparing the IV from the bottom, center and tip region of the NWs. In Figure 4.14(b), these correspond to the IV measured between the contacts AB (bottom), BC (center) and CD (tip). The IV characteristics of the AB, BC and CD contacts from Be1 and Be2 NWs are shown in Figure 4.15(a) and Figure 4.15(b) respectively. The asymmetry of the IVs from Be1 in Figure 4.15(a) indicates a Schottky-like behavior of the metal-semiconductor contacts. In addition, the decrease of the current values from bottom to tip of the Be1 NW is associated to an increase in the values of the Schottky barrier heights in the region of the NW where the contacts AB, BC and CD were fabricated. This change in the Schottky barrier height can be associated to a Be-dopant concentration profile that increases from the tip towards the root region of the NW, and such behavior was consistently observed for additional representative NWs from Be1 sample measured in the same configuration, as presented in Publication I.

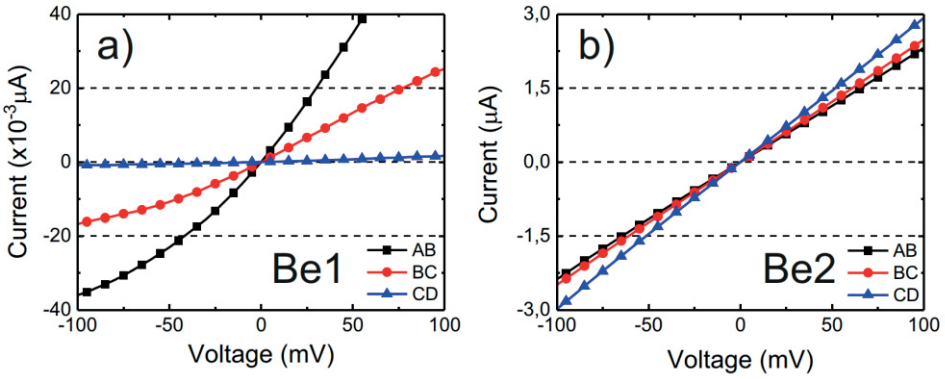

Figure 4.15: IV characteristics measured from different channels along (a) Be1 and (b) Be2 NWs. Adapted from Publication I.

In contrast to Be1, the IV measured from the AB, BC and CD contacts of Be2 NW present linear behavior with small variation in the current values between different channels, as can be seen in Figure 4.15(b). This behavior was also consistently observed for additional Be2 NWs measured with the same configuration in Publication I. In order to determine whether any dopant gradient was present also in Be2 NWs, the NW resistivities of each channel were obtained and compared. To this end, the specific contact resistivity ρ_C was obtained by fabricating five electrical contacts with increasing channel length along the NW, which is the TLM geometry described by Equations (3.1) and (3.2) in Chapter 3.4. With the value of ρ_C determined, the NW resistivity ρ_S can be determined by the relation:

$$R_T = \rho_S \frac{L}{A} + 2R_C \tag{4.1}$$

where R_T is the total channel resistance (NW + 2 contacts), L is the channel length and A is the hexagonal cross-section area of the NW. The values of L and A were measured from SEM images of the devices after transport characterization. The IV characteristics of Be2 NW with increasing channel length is shown in Figure 4.16(a). The total resistance of the longer channel (L=1.10 μm) was unexpectedly smaller than the shorter center channels, most likely due to contact overlap with one of the ends of the NW which resulted in smaller contact resistance. Therefore, the total resistance of this channel was omitted from the fitting procedure using Equation (3.1). Nevertheless, the fit of the remaining data points resulted in NW resistivity of

ρ_S = 0.027 Ω cm and specific contact resistance of $\rho_C = 4.5 \times 10^{-6}$ Ω cm². Based on this, the total contact resistance for each cannel is 18 kΩ.

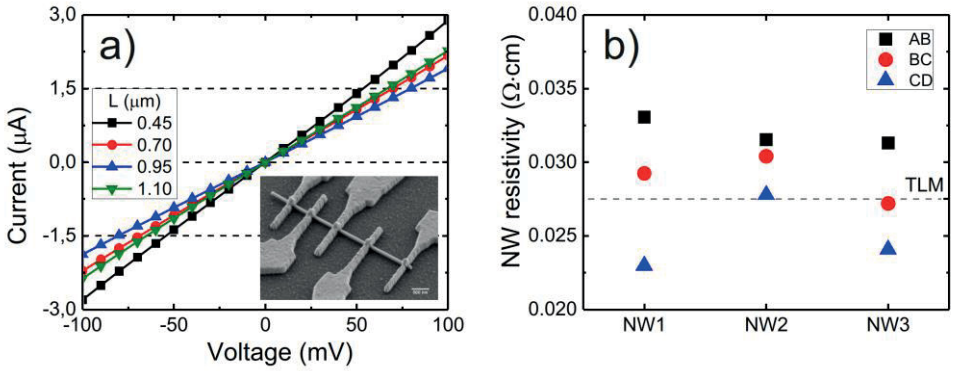

Figure 4.16: (a) IV characteristics of Be2 NW measured in TLM geometry. The inset shows a tilted SEM image of the measured device. (b) Nanowire resistivity obtained from representative Be2 NWs with four evenly-spaced contacts. The dashed line indicates the NW resistivity value obtained by TLM. Adapted from Publication I.

The NW resistivity for each channel of the evenly spaced contacts was calculated by using Equation (4.1), where the total resistance was obtained from the linear fit of the IV for each channel (AB, BC, CD) and the total contact resistance of 18 kΩ previously determined was used. The calculated resistivity values of each channel from three different Be2 NWs are shown in Figure 4.16(b), with the dashed gray line representing the resistivity value obtained from the NW analyzed by TLM in Figure 4.16(a). Despite of the NW-to-NW variation of the resistivity values obtained, we observe a consistent decrease of the NW resistivity from the bottom to the tip region which indicates that the axial Be concentration increases towards the tip.

4.1.5 Gradients of Be-dopant concentration

The IV analysis of the Be1 and Be2 NWs clearly shows that the Be-dopant gradient is opposite between both NW samples: the dopant concentration increases from the tip towards the bottom region of the Be1 NWs, while it decreases when following the same axial direction for the Be2 NWs. This suggests that the Be flux can determine the dominant dopant incorporation mechanism during NW growth. Since the Be-doped NWs do no exhibit any tapering (difference in diameter at the bottom and tip region), we can conclude that they grow constantly in both axial (VLS) and

radial (VS) direction. Therefore, we expect that the thickness of the VS grown shell is larger at the bottom than at the tip of the NWs as illustrated in Figure 2.3[11]. Thus, in Publication I we conclude that the Be dopants incorporate predominantly via the VS mechanism, through the NW sidewalls, in similar mechanism reported in [15].

On the other hand, if the Be dopants would incorporate predominantly via the VLS mechanism, through the Ga droplet, we would expect a dopant gradient that increases from bottom to tip [29, 30] in the same way that the thickness of the VLS grown core increases [75]. This is the behavior we observe for Be2 NWs. Therefore, we can conclude that the VS mechanism is predominant for low Be flux and that VLS is favored at higher Be flux. At lower Be flux, the direct impingement to the Ga droplet is the limiting factor for the Be incorporation via the VLS mechanism, while the axial growth rate (VLS) is around 10-times larger than the nominal growth rate, from which the nominal doping level is determined. This leads to the predominant VS incorporation observed for the Be1 NWs. As observed by Raman spectroscopy, the incorporation efficiency decreases with increasing Be flux. Thus, it is more likely that the VS incorporation mechanism is suppressed rather than an increase of the VLS incorporation rate. This can be attributed to the onset of Be segregation on the GaAs surface, which results in the surface roughening of the NW sidewalls as observed in the TEM analysis of the bottom region of Be1 and Be2 NWs in Figure 4.11. According to the thermodynamic model presented in [76], the growth rate can yield a significant decrease of the doping levels required determining the onset of Be segregation in VS grown Be-doped GaAs. In addition, the onset depends also on the As flux and growth temperature, which provides further evidence that the growth conditions affects the Be-dopant incorporation mechanism in self-catalyzed GaAs NW growth.

4.2 Te-doped GaAs nanowires

The main results of the incorporation of Te and *n*-type dopant in self-catalyzed GaAs NWs obtained in Publication II are presented in this chapter. The NWs were grown with a nominal Te-dopant concentration of 2×10^{19} cm^{-3} (Te1 sample in Table 1), based on Hall measurement of MBE grown Te-doped GaAs (100) planar layers. Additional *n*-type GaAs NW sample with undoped AlGaAs shell were grown for off-axis electron holography and atom probe tomography experiments. The structural changes of the GaAs NWs caused by Te doping were investigated by

TEM. Spatially-resolved Raman spectroscopy and transport characterization on single-NW level were applied to assess the Te concentration gradient along the NWs. The Raman and transport results are supported by complementary experimental techniques such as off-axis electron holography and atom probe tomography, which were obtained through international collaboration partners.

4.2.1 Structural properties

Figure 4.17 shows side view SEM images from (a) undoped (Ref2) and (b) Te-doped NWs (Te1). The undoped reference NWs grown for 80 min (Ref2) have an average length and diameter of 5100 nm and 150 nm respectively [11] and the Te-doped NWs grown for 60 min have an average length and diameter of 3700 nm and 170 nm. The average length and diameter of the undoped reference sample grown for 60 min (Ref1) are 4300 nm and 130 nm respectively, which indicates that the incorporation of Te dopants increases the radial and decreases the axial growth rates, as has been also previously reported in references [16, 77]. Since the undoped reference sample grown for 80 min (Ref2) has a diameter closer to the Te-doped NWs than the undoped sample grown for 60 min (Ref1), it was used as comparison for the Raman spectroscopy analysis further described in this text and in Publication II.

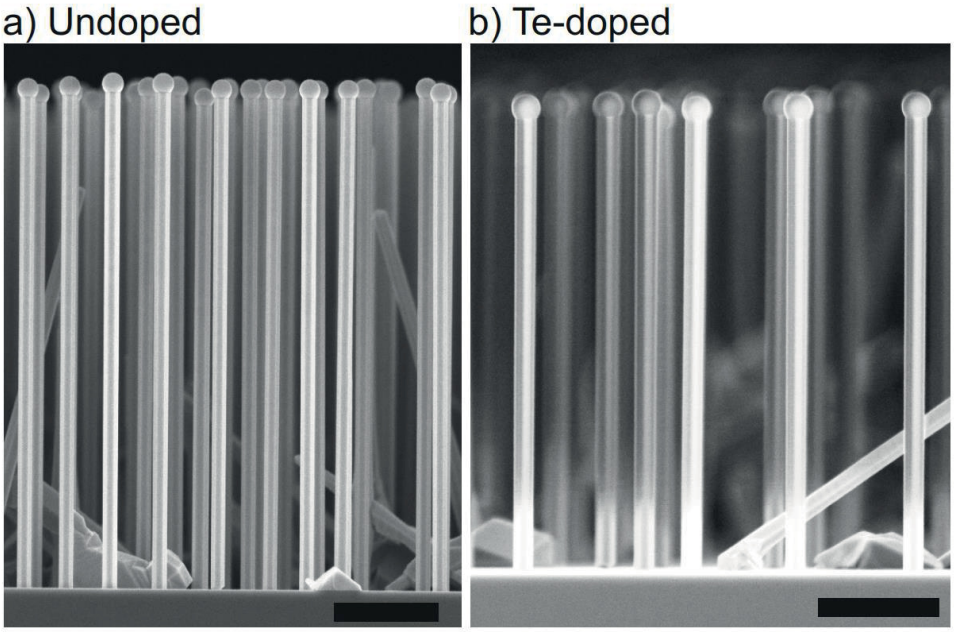

Figure 4.17: Side view SEM images of (a) Ref2 GaAs and (b) Te1 GaAs NW samples. The scale bars are 1 μm.

The TEM images and SAED of a representative Te-doped NW are shown in Figure 4.18. The Te-doped NWs grow with zinc-blende structure and the density of twin planes defects increases towards the NW tip, where it was observed a (111)-type sidewall faceting. This effect has been previously observed for self-catalyzed Te-doped GaAs NWs grown on GaAs substrates [16]. The increasing twinning frequency of the ZB structure towards the NW tip is clearly visible in the HR-TEM micrographs and further evidenced by the corresponding SAED patters in Figure 4.18(b)-(e), which were obtained from the regions marked by circles (1)-(4) in the low-magnification TEM image in Figure 4.18(a).

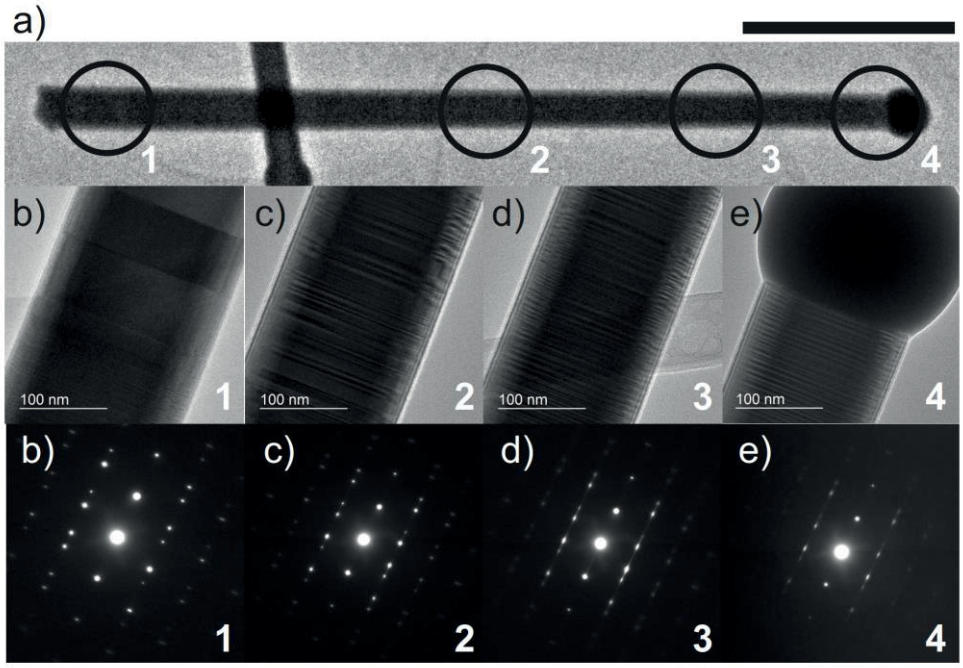

Figure 4.18: (a) low-magnification TEM image of a representative Te-doped GaAs NW. (b)-(e) High magnification HR-TEM micrographs and the corresponding SAED patterns from the corresponding regions labeled (1)-(4), where (1) is closer to the bottom and (4) to the tip regions of the NW. The scale bar in (a) is 1 μm and in (b)-(c) 100 nm. Adapted from Publication II.

4.2.2 Raman spectroscopy

Spatially-resolved Raman spectroscopy along the axis of the as-grown Ref2 and Te1 NWs was measured by adjusting the z-piezo stage position during spectra acquisition. The shallow depth of focus of the Raman setup combined with the low NW density allowed the measurements to be carried on the vertical standing NWs without harvesting them from the growth substrate. More details of the Raman experiments are discussed in Publication II. In this configuration, the GaAs (111) surfaces are measured in the backscattering geometry, from which selection rules allows the observation of the TO, LO and CPPM modes [44]. The correlation of the z-piezo height and the position of the NWs from where the Raman spectra were obtained was determined by the intensity of optical modes at ~520 cm^{-1} originating from the Si substrate. The linear polarization of the laser excitation was set

perpendicularly to the NW axis and the detection of the scattered intensity was unpolarized.

Figure 4.19(a) and (b) show Raman spectra obtained from the bottom (z=0 μm) and top (z=3.5 μm) from the undoped reference (Ref2) and Te-doped NW (Te1) respectively. In addition, the fitted CPPM curves from Te1 NW are shown in red lines in Figure 4.19(b). The scales have been selected to focus on the features with intensities much smaller than the GaAs TO/LO and the Si optical mode. The TO and LO modes of the undoped GaAs NW in Figure 4.19(a) exhibit typical peak positions and linewidths observed in GaAs NWs. The LO mode in the Te-doped NWs is clearly suppressed due to the screening of this mode caused by the presence of the free charge-carriers. In such case the LO intensity originates solely from the surface depletion layer, the width of which decreases with increasing doping concentration [51, 55, 78, 79]. In addition to the usual GaAs Raman peaks, two broad features at 160 cm^{-1} and 350 cm^{-1} (labeled X1 and X2, respectively) were observed in both undoped and Te-doped GaAs NWs. These modes are ascribed to disorder-activated acoustical phonons [80] and surface oxides [81, 82]. The high-frequency branch of the CPPM (L+) was observed to shift from 300-350 cm^{-1} at the bottom region to 650-700 cm^{-1} at the tip region of the NW, as can be seen from the fitted CPPM curves in Figure 4.19(b). This indicates that the free-carrier concentration increases from the bottom to the tip along the NW axis.

At the bottom region of the NW, only the L+ CPPM branch with an asymmetric lineshape was obtained from the fitting of the Raman spectrum from this region. As will be discussed with more details later in the text, the plasma frequency and damping constant obtained from the fit of the Raman spectrum using Equation 2.11 correspond to an overdamped case of the LO phonons and the plasmon associated to the free-electrons in this region, in similar way for *p*-GaAs. In this case, the L+ and L- branches are overlapped and undistinguishable, which is further complicated by the presence of the acoustic modes in the same spectral region.

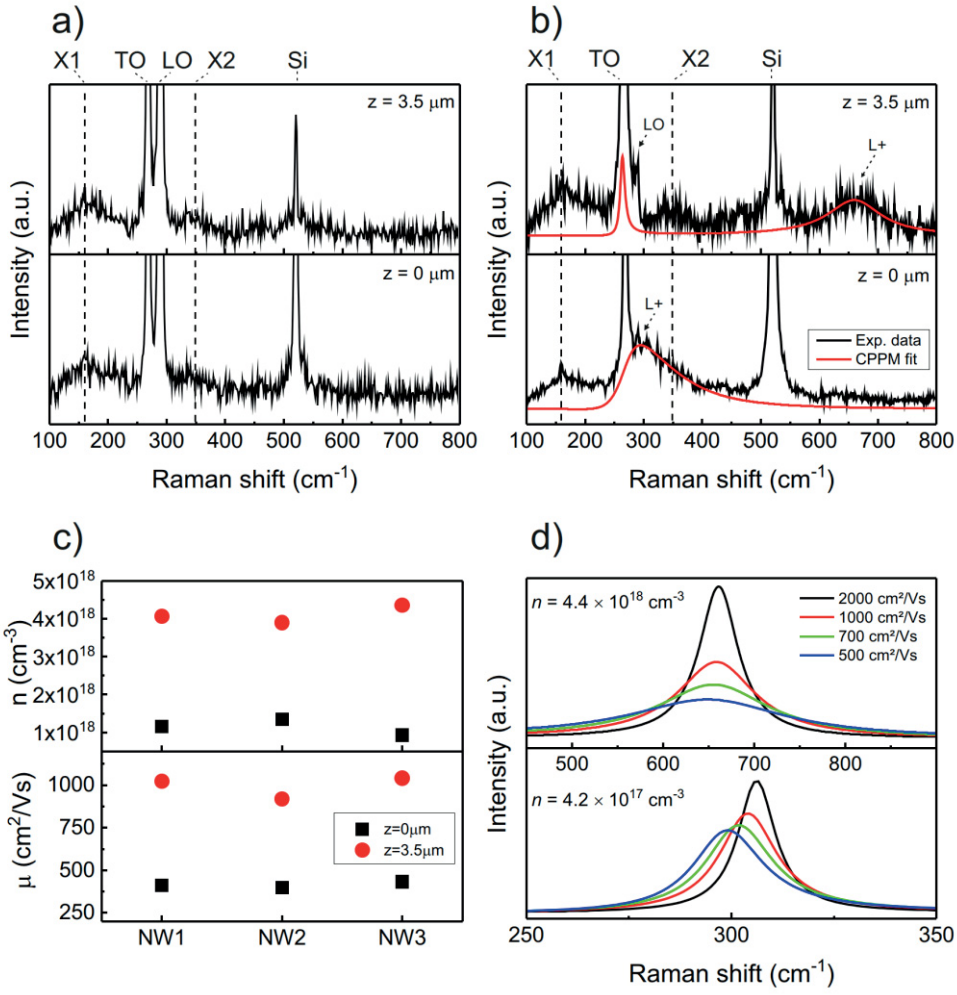

Figure 4.19: Raman spectra obtained at two different focal positions from (a) undoped reference GaAs NWs (b) Te-doped GaAs NW. Positions at z = 0 and z = 3.5 μm correspond to the bottom and top region of the NWs, respectively. The Raman spectra are normalized to the GaAs TO peak. (c) Electron concentration and mobility data obtained from the CPPM fit from the bottom and top regions of the Te-doped NW shown in (b) (NW1) and two additional representative Te-doped NWs. (d) Calculated CPPM line shapes for different values of the electron mobility for electron concentrations of 4.2×10^{17} (bottom) and 4.4×10^{18} cm^{-3} (top). Adapted from Publication II.

The plasma oscillation frequency and damping constant obtained from fit of the CPPM curves using Equation (2.11) allowed the estimation of the electron concentration (n) and mobility (μ) from the bottom and tip of representative Te1 NWs. The fit results for three different Te-doped NWs are shown in Figure 4.19(c),

and a good agreement between the values of n and μ obtained for the bottom and tip regions of the different NWs was observed. The free-electron concentration ranges from $\sim 1 \times 10^{18}$ cm^{-3} at the bottom and $\sim 4 \times 10^{18}$ cm^{-3} at the tip region of the NWs, consistently showing a gradient of Te-dopant concentration along the NW axis. Remarkably, the free-electron concentration values at the tip region of the NWs obtained by Raman spectroscopy is in good agreement with the Te-dopant concentration values obtained by atom probe tomography. This result indicates that 100% of the Te atoms incorporated in the GaAs NWs are activated as *n*-type dopants at the tip region of the NWs, which is an important result for future device applications.

The dependence of the values of the electron mobility for different dopant concentrations observed from the CPPM fit is now addressed. Usually, the electron mobility should decrease as the dopant concentration increases as a result of the reduced mean free path of the charge carriers. This is the opposite trend observed from the fit results of the CPPM curves from the Te-doped NWs and requires a careful interpretation. To this end, Figure 4.19(d) shows calculated CPPM curves for low doping level (bottom) and higher doping level (top) using several typical values of electron mobility (plasma damping constant). In addition, Figure 4(a) of Publication II shows the peak position of the CPPM L+ branch for calculated from Equation 2.11 for the investigated range of free-carrier concentration and electron mobility. It is clear from Figure 4(a) of Publication II that the free-electron concentration has a stronger influence on the peak position of the L+ when compared to the effect of the electron mobility. At typical electron mobility values for *n*-GaAs, the damping constant Γ tends to zero values, which refers to an undamped case. A decrease in the mobility value has a strong effect in the CPPM lineshape, resulting in its broadening as can be seen in Figure 4.19(d).

Therefore, the mobility values would be underestimated even by a small overestimation of the L+ peak width during the fitting procedure. The Raman spectra of the bottom part of the Te1 NW in Figure 4.19(b) is a clear example of the uncertainties that may arise from the fitting procedure. In the 300-350 cm^{-1} range, there is an overlap of the L+ branch, X2 peak and possibly the acoustic modes from the Si substrate. The spectral decomposition of this wavenumbers range in the Raman spectrum is further complicated by the nature and undefined selection rules of the L+ and X2. In addition, the combination of axial and possibly radial gradients of dopant concentration would result in extra uncertainties in the CPPM fit due to the volume of the NW probed in the Raman experiment. Nevertheless, the CPPM line shape analysis results in a good consistency and reliability when estimating the

free-carrier concentration in the Te1 NWs. Similar differences between the carriers mobility estimated by Raman spectroscopy and Hall effect experiments has been previously reported for *p*-type and *n*-type thin-films investigated by Raman spectroscopy [49, 54].

4.2.3 Transport properties

The IV characteristics of the Te-doped NWs were spatially-analyzed by fabricating four evenly spaced electrical contacts distributed along the NW axis. The *n*-GaAs-metal contact properties are characterized by the formation of a Schottky barrier with height determined by the Fermi level pinning at the GaAs surface, which is independent of the work function of the metal. Usual barrier heights of common metals deposited on *n*-GaAs(110) surface range from 0.7 to 0.9 eV [63] and the electrical transport mechanism will depend on the doping level at the semiconductor-metal interface region. In addition, a transition between the main transport mechanisms can happen for a certain range of bias voltage or temperature, as they will also affect the potential barrier at the metal-semiconductor interface. For low and moderate doping concentrations the dominant current transport mechanism is the thermionic emission (TE) over the barrier and the IV behavior is of typical Schottky diode. At high dopant concentrations the linear IV behavior is characteristic of low contact resistance, resulting from a reduced barrier width – this favors the tunneling of the electrons with energies close to the Fermi level energy and is known as field emission (FE) mechanism. At last, for intermediate doping levels the main transport mechanism is called thermionic field emission (TFE). In this mechanism the thermally excited electrons can tunnel through the narrower upper part of the barrier [35, 36].

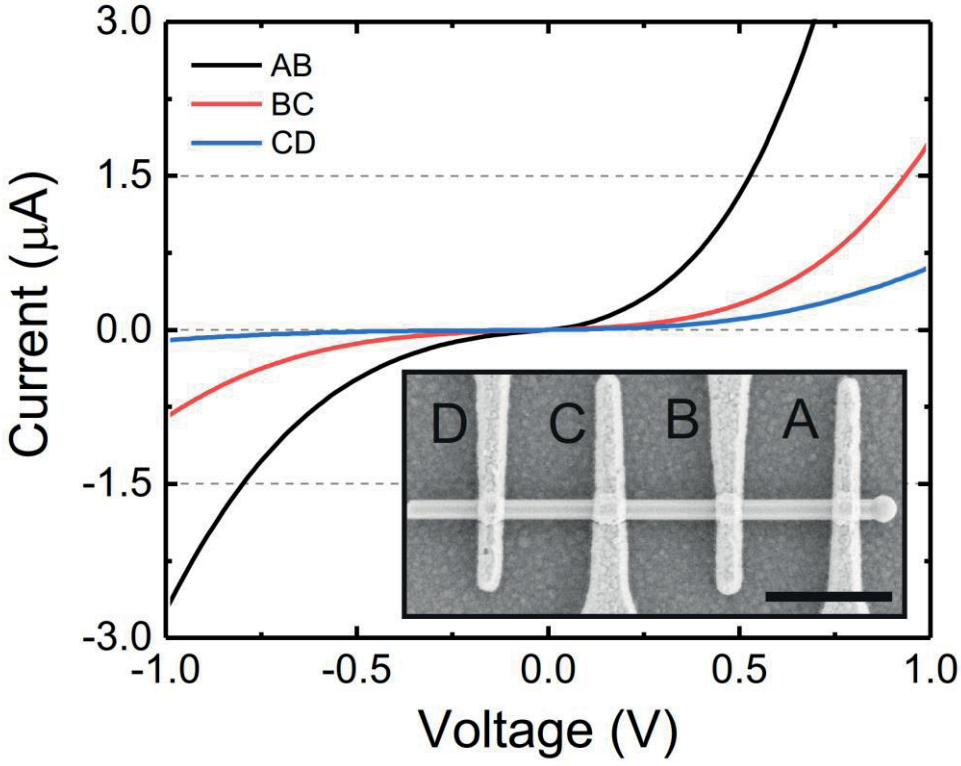

Figure 4.20: IV characteristics showing asymmetric double-Schottky type behavior measured from a Te-doped GaAs NW. The inset shows the measured device and the IVs correspond to the different contact pairs labeled along the NW. The scale bar is 1 μm. Adapted from Publication II.

Figure 4.20 shows the IV characteristics of a Te-doped GaAs NW measured from the contact pairs located at the tip (AB), center (BC) and bottom (CD) regions along the NW axis, as illustrated in the SEM image of the inset. Each contact pair exhibits non-linear, asymmetric, IV characteristics with positive bias resulting in higher current values than for the negative bias. In addition, the current value consistently increases towards the NW tip for the same bias voltage applied for each contact pair. In order to exclude possible influence of the interface properties in the Schottky barrier (barrier reduction caused by image forces, Fermi level pinning position due to different surface terminations, defect assisted tunneling and interfacial layers), several NW devices with the same contact processing parameters were measured. The additional IV data are presented in the Supplementary Material of Publication

II. The IV characteristics along the measured NWs have the same trend as the one presented in Figure 4.20.

One way to interpret the IV curves from the Te-doped NWs is to consider that the NW acts as a resistive channel separating two back-to-back Schottky metal-semiconductor contacts [74, 83]. In this way, regardless the polarity of the applied bias voltage one of the contacts will be reversed biased while the other will be forward biased. Considering the values of dopant concentration and electron mobility estimated by Raman spectroscopy of $n = 4 \times 10^{18}$ cm^{-3} and $\mu = 1000$ cm^2/V s for the tip region, and $n = 1 \times 10^{18}$ cm^{-3} and $\mu = 400$ cm^2/V s for the bottom region, it can be estimated that the resistive voltage drop in the NW is at least two orders of magnitude smaller than the applied bias. Therefore, it is safe to assume that the current flow observed in the Te-doped NWs is mainly limited by the reverse-biased Schottky contacts. At room temperature and for the doping levels estimated by Raman spectroscopy and supported by APT, the reverse current is mainly due to TFE mechanism and can be overcome by pure FE at higher bias values or with increasing doping concentration. Therefore, a quantitative analysis of the IVs based on the transport mechanisms involved leads to the conclusion that there is indeed an axial dopant gradient along the Te-doped NWs.

4.2.4 Gradients of Te-dopant concentration

The presence of an axial gradient of Te-dopants along the NWs is evidenced by both Raman spectroscopy and IV analysis. In addition, off-axis electron holography data measured from different slices from the bottom and tip region of *n*-GaAs/*i*-AlGaAs core-shell NWs also show that both an axial and radial dopant gradients are formed during the self-catalyzed growth of Te-doped GaAs NWs investigated in Publication II. The APT experiments from the same set of NW samples show that there is a uniform Te concentration in the upper part of the NWs. But it should be noted that the spatial resolution of APT is limited to the initial ~1000 nm and ~100 nm along the axial and radial directions of the NW, respectively. This limitation on the probed volume of the NWs by APT originates from the field of view and reconstructions tools used for the experiment [84, 85]. On the other hand, the asymmetric behavior of the IV from the tip region (AB contacts) from the Te-doped NWs suggests that there is indeed an axial dopant gradient in this region of the NW, since the metal-semiconductor properties are much more sensitive on the doping level at the surface.

Based on a theoretical model developed in Publication II to explain the origin of the non-uniform concentration of Te dopants in the GaAs NWs the growth conditions strongly affect the distribution and how the dopants and incorporated during self-catalyzed growth. The Te dopants incorporate mainly via the VLS mechanism, which should result in a uniform dopant concentration for each monolayer formed. However, the VLS growth usually results in tapered NWs due to increasing radius of the Ga-droplet during self-catalyzed growth. There is no evidence of tapering in the investigated Te-doped GaAs as seem from the SEM images in Figure 4.17 and TEM image in Figure 4.18. Therefore, we can conclude that the radial growth due to VS mechanism is also significant in these samples. The probability of Te incorporation via VS mechanism strongly depends on the temperature [86], and can be neglected for this case. This means that the final NW structure is a tapered VLS grown Te-doped GaAs core surrounded by an undoped GaAs VS grown shell, as illustrated in Figure 4.21.

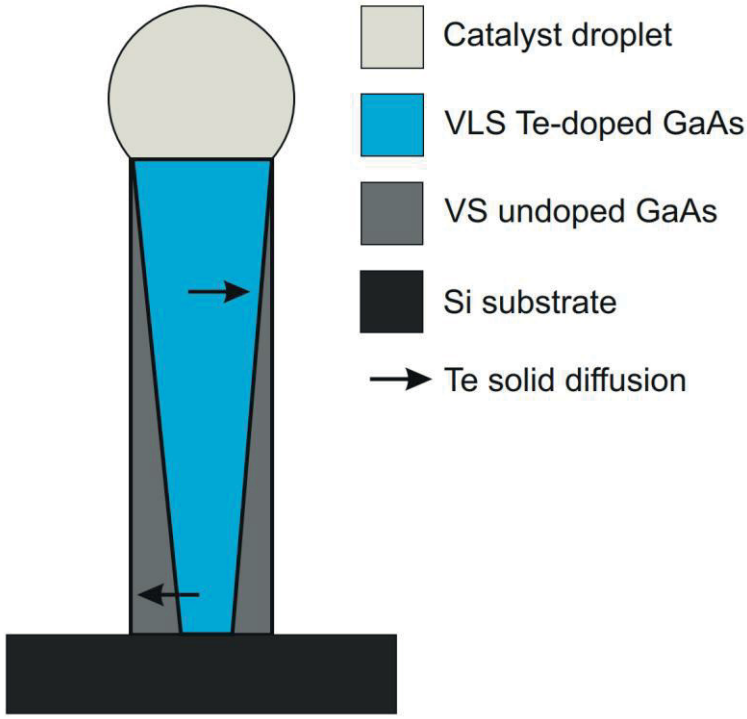

Figure 4.21: Schematics showing the most probable final structure of the Te dopants distributions of the n-GaAs NWs. The VLS grown Te-doped GaAs core in blue is tapered due to increase of the Ga-droplet diameter, surrounded by the VS undoped GaAs that is responsible for radial growth. The Te solid diffusion are represented by arrows. The relative sizes of the substrate, NW and Ga droplet are out of scale so that the features of interest can be better illustrated.

The incorporation rate of Te via the VLS mechanism will also increase during the NW growth. The incorporation efficiency of dopants is proportional to the squared radius at the base of the catalyst droplet, which also determines the NW radius. Thus, we can conclude that less Te incorporates at the bottom of the NW (which has smaller diameter of the VLS grown core) than at the tip region of the NW (with increased VLS grown diameter), resulting in the shapes of the VLS core and VS shell represented in Figure 4.21. Moreover, the difference in dopants concentration along the NW radial direction will lead to a solid diffusion of Te dopants from the VLS Te-doped core to the VS undoped GaAs shell.

The radial gradient for each segment will depend on the ratio of the solid diffusion coefficient over the radial growth rate. In this case, the radial growth rate is faster than the solid diffusion which results in the non-uniform Te-dopant

distribution. Two possible options to avoid a gradient of Te-dopant distribution in self-catalyzed growth of GaAs NWs are to increase the VS incorporation mechanism rates or to eliminate the radial growth. These results show that a careful control of the growth parameters during self-catalyzed grow of Te-doped GaAs NWs is required. In particular, a key factor is to control the radial growth rate of the NWs.

4.3 Extrinsic optical chirality in the absorption and emission of partially Au-coated GaAs/AlGaAs nanowires

As discussed in Chapter 2.5, the optical modes of III-V semiconductor NWs can be modified by altering the combined symmetry of the samples and the optical experiment. To this end, the NWs were partially covered with Au thin film by tilting the as-grown NW samples in relation to the Au-flux during e-beam metal evaporation. The nominal Au-thickness deposited on the NWs sidewalls is determined from the tilt angle of the sample holder and the planar Au-thickness evaporated. Therefore, the Au-evaporation parameters were selected in such a way to obtain 10-20 nm of nominal Au thickness in two or three of the hexagonal-shaped NW sidewalls Figure 4.22 shows tilted SEM images of GaAs and GaAs/AlGaAs NWs with 2-facets covered with Au for two different tilt angles of the sample holder, i.e. resulting in different effective Au deposition rate. With increasing tilt angle, the planar Au-thickness necessary to keep the same nominal thickness deposited on the NWs sidewalls is reduced. This combined with the fact that the same Au-flux (in nm/s) is used for both tilt angles results in an increased effective Au-deposition rate at the NWs sidewalls. It is expected that a higher effective Au-deposition rate would result in a decrease of the apparent surface roughness of the Au layer at the nanoscale. In addition, the GaAs sample has a much higher NW density than the GaAs/AlGaAs, which gives insight on the possible flux shadowing effects.. As can be seen comparing Figure 4.22(a)-(d) with Figure 4.22(b)-(e), not only that the Au layer roughness was indeed reduced, but also the coverage of the Au layer on the NWs facets was considerably improved. This effect was consistent regardless the density, length or diameter of the NWs investigated.

The chiral properties of the absorption (Publication IV) and PL emission (Publication V) of the Au-coated NWs were investigated by properly selecting the angle of incidence of the excitation laser in relation to the NW growth axis. A structure that is not intrinsically chiral can exhibit chiral optical response as long as the following three vectors do not lie in the same plane: (1) the vector representing

the surface normal to the sample, (2) the direction of anisotropy of the structure, and (3) the wave vector ***k*** representing the direction of propagation of the excitation light. If we set the z-direction as the [111] direction of ZB which is the NW growth direction, vector (1) is parallel to the NW axis and therefore to the z-direction, vector (2) is parallel to the radial direction of the NW and points from the Au-free sidewalls towards the Au-coated ones, and vector (3) represents the laser excitation direction. In the experiments further described, the angle between (1) and (3) is selected by adjusting the tilt angle of the NW sample holder as described in Publication IV and Publication V .

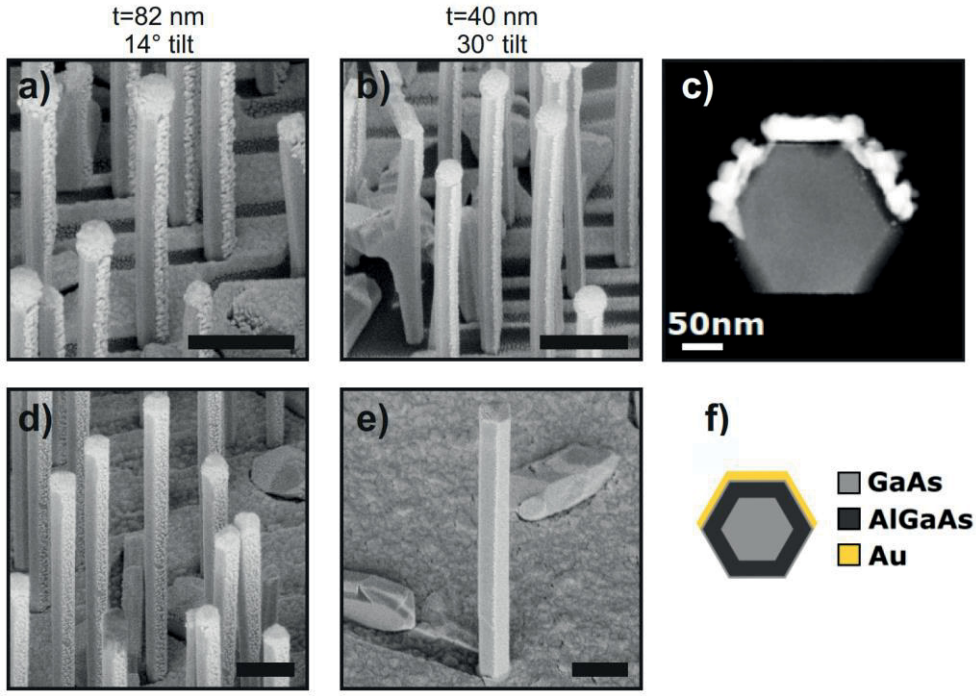

Figure 4.22: Structural details of the Au-coated NWs. (a)-(b) shows tilted SEM images of GaAs NWs with 2 facets covered with Au. (d)-(e) show GaAs/AlGaAs core-shell NWs. The Au planar thickness and the tilt angle of the NWs during metal evaporation. (c) Cross-sectional dark-field TEM image of GaAs/AlGaAs NW from (d) with 3 facets covered with Au. (f) Cross-sectional representation of the metal-NW structure. The scale bars in (a), (b), (d) and (e) are 500 nm and the SEM images were obtained with a 30° tilt of the sample holder. The scale bars in (c) is 50 nm. Figures (c) and (f) were adapted from Publication V.

The extrinsic chirality of the absorption properties of Au-coated GaAs/AlGaAs NWs was investigated by a scattering-free technic called PAS in Publication IV. The proper orientation of the Au-coated NW sample inside the PA chamber in relation

to the direction of the laser excitation provides the required configuration for observation of the extrinsic chiral properties. A 532 nm laser is circularly polarized by passing through a linear polarizer followed by a quarter-wave plate before reaching the NW sample. The angle between the laser wave vector and the surface normal to the NW growth axis can be modified by a tilting stage.

The polar plot in Figure 4.23(a) shows the PA signal intensity of the absorption peak of GaAs/AlGaAs NWs with 3 facets covered with Au. The PA spectra were measured for different angles of the quarter-waveplate, where 45° corresponds to RCP and 135° to LCP, and for several tilt angles of the NW sample holder. The difference between the lobes for RCP and LCP is clearly dependent on the sample tilt angle. The CD dependence on the tilt angle has been determined experimentally and theoretically for Au-coated GaAs/AlGaAs NWs with different lengths and diameters of the GaAs core and AlGaAs shell and the results are shown in Figure 4.23(b). The experimental data were determined using Equation (2.14) and the quarter-waveplate was set to LCP. Although it was determined that the NWs diameter strongly affects the linear response of Au-free NWs [66], it was observed that the NW length is the dominating parameter in the CD signal. The discrepancies of the simulated curves (dashed lines) and experimental data (solid curves) in Figure 4.23(b) were ascribed to the non-chiral contributions of the Si substrate and to the collective interactions of the optical fields from neighboring NWs, but nevertheless the CD behavior is consistent between theory and experimental data.

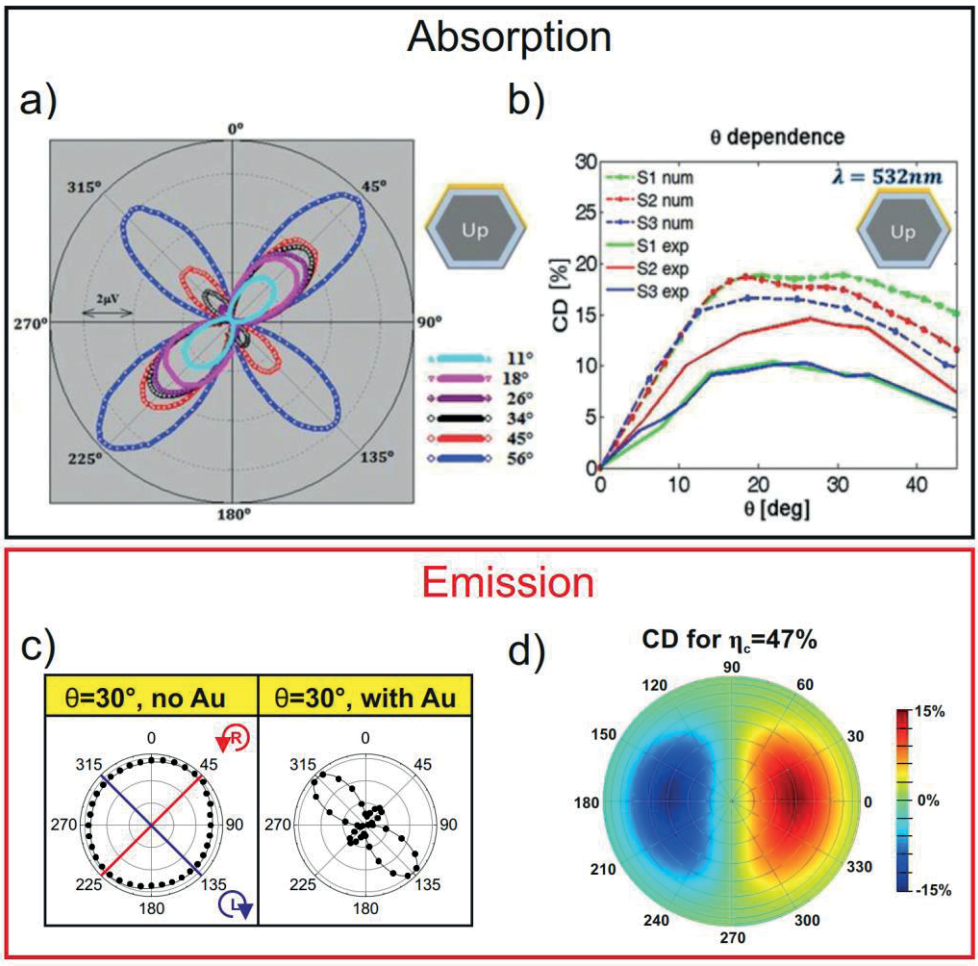

Figure 4.23: (a) PAS polar plot of Au-coated GaAs/AlGaAs NW at 532 nm for various angles of incidence as illustrated in the legend. (b) Dependence of the CD on the incidence angle of GaAs/AlGaAs NWs with different dimensions (length and diameter of the GaAs core and thickness of the AlGaAs shell). The solid lines represent the experimental data and the dashed-dotted lines the numerical simulations. (c) Polar plot of the normalized PL intensity vs λ/4 waveplate angle of GaAs/AlGaAs with and without Au coating, and tilted by 30° in relation to the NW growth axis and direction of the laser excitation. (d) Far-field CD map of Au-coated GaAs/AlGaAs NW calculated for the best fit of the CD properties as a function of the tilt angle, ranging from 0° to 90° with 10° steps. (a) and (b) were adapted from Publication IV, (c) and (d) were adapted from Publication V.

The extrinsic chirality properties of the room-temperature photoluminescence emission (PL) of the GaAs/AlGaAs NWs with 3 facets covered with Au were investigated by exciting the NWs with a 640 nm linear-polarized laser and detecting the PL signal for several quarter-waveplate angles. A detailed description of the

experimental setup and sample geometry are presented in Figure 2 of Publication V. The NWs were tilted in relation to the growth axis and the direction of incidence of the laser excitation, in order to achieve the geometry required for extrinsic chirality experiments. The unpolarized room-temperature PL spectra of the GaAs/AlGaAs NWs is centered at 870 nm, with a small blueshift of the PL peak of the Au-coated NWs in respect to the reference samples which can be ascribed to band-bending effects due to the presence of Au. Figure 4.23(c) shows the polar plot of the PL peak intensities detected with different angles of the quarter-waveplate and with a 30° tilt of the NWs axis in relation to the laser excitation direction. As it is expected, the Au-free NWs sample do not exhibit any extrinsic chiral behavior of the PL emission since there is no anisotropy in the NW radial direction. On the other hand, a strong extrinsic chiral behavior is evidenced by the difference in the lobes of the LCP and RCP behavior of the PL emission of the Au-coated NWs. The LCP and RCP globes behavior were inverted if the NWs were tilted by 180° in relation to the growth axis, i.e., a -30° tilt. This is a characteristic property of extrinsic chirality and observed in the PL emission.

The CD from the PL emission of the Au-coated GaAs/AlGaAs NWs was investigated experimentally and theoretically as a function of the NWs tilt angle but using the figure of merit represented by Equation (2.14). It was determined that the extrinsic chirality behavior of the PL emission arises mostly from the HE_{11} optical mode, more specifically in the direction where the anisotropy exists along the NW radial axis due to the presence of the Au layer. A theoretical model was used to fit the experimental data of Publication V with support of a Lambertian source to extract the part of PL emission that contributes to the CD changes, and the results are shown as polar plot in Figure 4.23(d). The maximum CD value of 15% was experimentally achieved for tilt angle of 20°, and the best fit to the experimental data was obtained for coupling efficiency of η_C = 47%. The value η_C represents the coupling efficiency of the HE_{11} modes, while the uncoupled part modeled by the Lambertian source contributes to the unpolarized background emission that lowers the value of CD. The roughness of the Au layer deposited on the NW sidewalls is responsible for scattering losses and is one factor that contributes to the uncoupled emission discussed in Publication V. Therefore, it is expected that the extrinsic chirality properties observed in both absorption and emission will be improved by the decreased Au layer roughness on the NW sidewalls. As shown in Figure 4.22 (b) and (d), this was achieved by increasing the effective Au deposition rate to the NW sidewalls.

The main results from designing asymmetrically-Au-coated GaAs/AlGaAs NWs for extrinsic optical chirality experiments show that the Au layer can control the handedness of absorption efficiency of circular polarized light. Moreover, the direction and handedness of the PL emission from the GaAs NW core can also be controlled by the correct design of the Au layer on the NW sidewalls. The possibility of combining the light-emitting properties of III-V semiconductor NWs and control of the circular polarization of the absorption and/or emission of optical fields paves the way to a broad range of applications that require chiral light detector or sources, such as in fields of quantum technology, biology and chemistry.

5 CONCLUSIONS

The main objective of this thesis was to correlate the structural, optical and carrier transport properties of Te- and Be-doped GaAs NWs with the growth conditions used in the self-catalyzed NW epitaxy on Si/SiO_x substrate. The main dopant incorporation mechanisms during self-catalyzed growth of *n* and *p* type GaAs NWs were identified by combining data from complementary experimental techniques. The unique NW geometry and reduced dimensions were exploited also in the chiral properties in terms of optical absorption and emission of circularly-polarized radiation of GaAs/AlGaAs core-shell structures partially covered with Au.

The incorporation of Be-dopant in self-catalyzed GaAs NWs was investigated in Publication I. The suppression of the formation of twin planes and stacking faults was found to be associated to the increasing Be-dopant concentration for two different NW samples. Spatially resolved Raman spectroscopy was used to estimate the hole concentration and mobility along the NW axial direction by analyzing the coupling of the lattice phonons with the plasma associated to the free-carriers. It was found that the Be-dopants incorporation efficiency decreased from 60% to 35% of the nominal doping level with increasing Be flux during self-catalyzed NW growth. Moreover, the IV characterization of Be-doped GaAs NWs revealed the existence of two types of axial gradients of dopant concentration which depends on the nominal doping level. With low Be flux, the dopant concentration decreases from the bottom towards the tip of the NW which was ascribed to the predominance of VS incorporation mechanism of Be dopants. The opposite gradient was observed for higher Be flux, which was a result of increased significance of the VLS mechanisms for the growth conditions used.

The effect of the several fabrication steps used to obtain Ohmic contacts on *p*-GaAs NWs was exploited to the unique surface orientation that results from self-catalyzed NW growth. In Publication III Be-doped GaAs NWs were used as base material for characterization of the metal-semiconductor interface at the nanoscale, aiming to Ohmic contacts. Different processing parameters were developed and their IV characteristics were interpreted based on structural characterization of GaAs (110) substrates with similar thin films used in the NW samples. It was found that combining an HCl oxide removal, a $(NH_4)_2S_x$ surface passivation and deposition

of Pt/Ti/Pt/Au metallic multilayer to the NW sidewalls resulted in a total electrical resistance of 72 kΩ. This corresponds to a 95% decrease of the total electrical resistance in comparison to NW devices with same surface treatment but with a Ti/Pt/Au metallic multilayer, which is traditionally used to obtain Ohmic contacts to (100) surface-oriented *p*-GaAs thin films. Structural characterization of similar metallic thin films revealed a higher degree of crystallinity of Pt compared to Ti when deposited directly on GaAs (110) substrates. The findings in Publication III are relevant on the technological point of view for the design of Ohmic contacts to GaAs NWs based devices, showing that the quality of the metal-semiconductor interface at the NW sidewalls has a major role in device performance.

The incorporation of Te as *n*-type dopant in self-catalyzed growth of GaAs NWs was investigated in Publication II. The structural characterization showed that the incorporation of Te-dopant increases the radial and suppresses the axial growth rates when compared to undoped GaAs NW self-catalyzed growth. The incorporation of Te also promoted the formation of rotational twin planes. Spatially-resolved Raman spectroscopy and IV analysis revealed a gradient of Te-dopant concentration that increases from bottom towards the tip of the NWs. The results were in agreement with data obtained from atom probe tomography and off-axis electron holography experiments. By combining the experimental data with a theoretical model, it was shown that Te dopants incorporate via the VLS mechanism through the Ga droplet in self-catalyzed GaAs NW growth. This creates a tapered VLS Te-doped GaAs core and an undoped GaAs VS-grown shell, which results in an axial and radial doping gradients along the NWs.

The deposition of asymmetric Au-layers on the sidewalls of GaAs/AlGaAs core-shell NWs was developed and optimized by adjusting the tilting angle of the NW sample in relation to the incoming Au-flux in the e-beam metal evaporation chamber. The combined break of symmetry of the NW and measurement geometry created the required conditions for extrinsic optical chirality experiments. The findings in Publications IV and V showed that the Au layer can control the handedness of absorption efficiency of circular polarized light. Moreover, the direction and handedness of the PL emission from the GaAs NW core can also be controlled by the correct design of the Au layer on the NW sidewalls. The possibility of combining the light-emitting properties of III-V semiconductor NWs and control of the circular polarization of the absorption and/or emission of optical fields paves the way to a broad range of applications that require chiral light detector or sources, such as in fields of quantum technology, biology and chemistry.

6 REFERENCES

1. Joyce HJ, Gao Q, Hoe Tan H, et al (2011) **III–V semiconductor nanowires for optoelectronic device applications**. Prog Quantum Electron **35**:23–75

2. Fang M, Han N, Wang F, et al (2014) **III-V nanowires: Synthesis, property manipulations, and device applications**. J Nanomater **2014**:

3. Dimakis E, Jahn U, Ramsteiner M, et al (2014) **Coaxial Multishell (In,Ga)As/GaAs Nanowires for Near-Infrared Emission on Si Substrates**. Nano Lett **14**:2604–2609

4. Svensson CPT, Mårtensson T, Trägårdh J, et al (2008) **Monolithic GaAs/InGaP nanowire light emitting diodes on silicon**. Nanotechnology **19**:305201

5. Aberg I, Vescovi G, Asoli D, et al (2016) **A GaAs Nanowire Array Solar Cell With 15.3% Efficiency at 1 Sun**. IEEE J Photovoltaics **6**:185–190

6. van Dam D, van Hoof NJJ, Cui Y, et al (2016) **High-Efficiency Nanowire Solar Cells with Omnidirectionally Enhanced Absorption Due to Self-Aligned Indium–Tin–Oxide Mie Scatterers**. ACS Nano **10**:11414–11419

7. Thompson MD, Alhodaib A, Craig AP, et al (2016) **Low Leakage-Current InAsSb Nanowire Photodetectors on Silicon**. Nano Lett **16**:182–187

8. Giuntoni I, Geelhaar L, Bruns J, Riechert H (2016) **Light coupling between vertical III-As nanowires and planar Si photonic waveguides for the monolithic integration of active optoelectronic devices on a Si platform**. Opt Express **24**:18417

9. Hakkarainen T V., Schramm A, Mäkelä J, et al (2015) **Lithography-free oxide patterns as templates for self-catalyzed growth of highly**

uniform GaAs nanowires on Si(111). Nanotechnology **26**:275301

10. Koivusalo E, Hakkarainen T, Guina M (2017) **Structural Investigation of Uniform Ensembles of Self-Catalyzed GaAs Nanowires Fabricated by a Lithography-Free Technique**. Nanoscale Res Lett **12**:192

11. Koivusalo ES, Hakkarainen T V., Guina MD, Dubrovskii VG (2017) **Sub-Poissonian Narrowing of Length Distributions Realized in Ga-Catalyzed GaAs Nanowires**. Nano Lett **17**:5350–5355

12. Koivusalo ES, Hakkarainen T V., Galeti HVA, et al (2019) **Deterministic Switching of the Growth Direction of Self-Catalyzed GaAs Nanowires**. Nano Lett **19**:82–89

13. Dufouleur J, Colombo C, Garma T, et al (2010) **P-Doping Mechanisms in Catalyst-Free Gallium Arsenide Nanowires**. Nano Lett **10**:1734–1740

14. Salehzadeh O, Chen MX, Kavanagh KL, Watkins SP (2011) **Rectifying characteristics of Te-doped GaAs nanowires**. Appl Phys Lett **99**:1–4

15. Casadei A, Krogstrup P, Heiss M, et al (2013) **Doping incorporation paths in catalyst-free Be-doped GaAs nanowires**. Appl Phys Lett **102**:013117

16. Suomalainen S, Hakkarainen T V., Salminen T, et al (2015) **Te-doping of self-catalyzed GaAs nanowires**. Appl Phys Lett **107**:012101

17. Orrù M, Repiso E, Carapezzi S, et al (2016) **A Roadmap for Controlled and Efficient n-Type Doping of Self-Assisted GaAs Nanowires Grown by Molecular Beam Epitaxy**. Adv Funct Mater **26**:2836–2845

18. Goktas NI, Fiordaliso EM, LaPierre RR (2018) **Doping assessment in GaAs nanowires**. Nanotechnology **29**:234001

19. Sze SM, Ng KK (2006) **Physics of Semiconductor Devices, 2nd ed**. John Wiley & Sons, Inc., Hoboken, NJ, USA

20. Besson JM, Itié JP, Polian A, et al (1991) **High-pressure phase transition and phase diagram of gallium arsenide**. Phys Rev B

44:4214–4234

21. Streetman BG, Banerjee S (2006) **Solid state electronic devices**. Pearson/Prentice Hall

22. Dimakis E, Ramsteiner M, Tahraoui A, et al (2012) **Shell-doping of GaAs nanowires with Si for n-type conductivity**. Nano Res **5**:796–804

23. Wagner RS, Ellis WC (1964) **Vapor-liquid-solid mechanism of single crystal growth**. Appl Phys Lett **4**:89–90

24. Spirkoska D, Abstreiter G, Morral AFI (2009) **GaAs nanowires and related prismatic heterostructures**. Semicond Sci Technol **24**:

25. Koivusalo E (2016) **EPITAXIAL III-V SEMICONDUCTOR NANOWIRES**. Tampere University of Technology

26. Dick K a. (2008) **A review of nanowire growth promoted by alloys and non-alloying elements with emphasis on Au-assisted III-V nanowires**. Prog Cryst Growth Charact Mater **54**:138–173

27. Dayeh SA, Chen R, Ro YG, Sim J (2017) **Progress in doping semiconductor nanowires during growth**. Mater Sci Semicond Process **62**:135–155

28. Wallentin J, Borgström MT (2011) **Doping of semiconductor nanowires**. J Mater Res **26**:2142–2156

29. Zhang Y, Sun Z, Sanchez AM, et al (2018) **Doping of Self-Catalyzed Nanowires under the Influence of Droplets**. Nano Lett **18**:81–87

30. Dastjerdi MHT, Fiordaliso EM, Leshchenko ED, et al (2017) **Three-fold Symmetric Doping Mechanism in GaAs Nanowires**. Nano Lett **17**:5875–5882

31. Ketterer B, Mikheev E, Uccelli E, Fontcuberta I Morral A (2010) **Compensation mechanism in silicon-doped gallium arsenide nanowires**. Appl Phys Lett **97**:1–4

32. De-Sheng J, Makita Y, Ploog K, Queisser HJ (1982) **Electrical properties and photoluminescence of Te-doped GaAs grown by**

molecular beam epitaxy. J Appl Phys **53**:999–1006

33. Salehzadeh O, Kavanagh KL, Watkins SP (2012) **Controlled axial and radial Te-doping of GaAs nanowires**. J Appl Phys **112**:

34. Rideout VL (1975) **A review of the theory and technology for ohmic contacts to group III–V compound semiconductors**. Solid State Electron **18**:541–550

35. Rhoderick EH (1982) **Metal-semiconductor contacts**. IEE Proc I Solid State Electron Devices **129**:1

36. Stratton R, Padovani FA (1966) **Field and thermionic-field emission in Schottky barriers**. Solid State Electron **9**:695–707

37. Yu PY, Cardona M **Fundamentals Of Semicondutors: Physics and Materials Properties, Fourth**. Springer

38. Cantarero A (2013) **Review on Raman scattering in semiconductor nanowires: I. theory**. J Nanophotonics **7**:071598

39. Zardo I, Conesa-Boj S, Peiro F, et al (2009) **Raman spectroscopy of wurtzite and zinc-blende GaAs nanowires: Polarization dependence, selection rules, and strain effects**. Phys Rev B **80**:245324

40. Glas F, Harmand JC, Patriarche G (2007) **Why does wurtzite form in nanowires of III-V zinc blende semiconductors?** Phys Rev Lett **99**:3–6

41. Strauch D, Dorner B (1990) **Phonon dispersion in GaAs**. J Phys Condens Matter **2**:1457–1474

42. Ketterer B (2011) **Raman Spectroscopy of GaAs Nanowires : Doping Mechanisms and Fundamental Properties**. École Polytechnique Fédérale de Lausanne

43. De Luca M, Fasolato C, Verheijen MA, et al (2019) **Phonon Engineering in Twinning Superlattice Nanowires**. Nano Lett acs.nanolett.9b01775

44. Steele JA, Puech P, Lewis RA (2016) **Polarized Raman backscattering selection rules for (hhl)-oriented diamond- and zincblende-type**

crystals. J Appl Phys **120**:055701

45. Hilse M, Ramsteiner M, Breuer S, et al (2010) **Incorporation of the dopants Si and Be into GaAs nanowires**. Appl Phys Lett **96**:193104

46. Spirkoska D, Abstreiter G, Fontcuberta i Morral A (2008) **Size and environment dependence of surface phonon modes of gallium arsenide nanowires as measured by Raman spectroscopy**. Nanotechnology **19**:435704

47. Sahoo P, K. A, Raj B, Dhar S (2011) **Surface Optical Modes in Semiconductor Nanowires**. In: Nanowires - Implementations and Applications. InTech

48. Venkatesan S, Mancabelli T, Krogstrup P, et al (2017) **Surface optical phonon propagation in defect modulated nanowires**. J Appl Phys **121**:085702

49. Irmer G, Toporov V V., Bairamov BH, Monecke J (1983) **Determination of the charge carrier concentration and mobility in n-gap by Raman spectroscopy**. Phys Status Solidi **119**:595–603

50. Irmer G, Wenzel M, Monecke J (1997) **Light scattering by a multicomponent plasma coupled with longitudinal-optical phonons: Raman spectra of p-type GaAs:Zn**. Phys Rev B **56**:9524–9538

51. Abstreiter G, Trommer R, Cardona M, Pinczuk A (1979) **Coupled plasmon-LO phonon modes and Lindhard-Mermin dielectric function of n-GaAs**. Solid State Commun **30**:703–707

52. Mooradian A, McWhorter AL (1967) **Polarization and Intensity of Raman Scattering from Plasmons and Phonons in Gallium Arsenide**. Phys Rev Lett **19**:849–852

53. Mlayah A, Carles R, Landa G, et al (1991) **Raman study of longitudinal optical phonon-plasmon coupling and disorder effects in heavily Be-doped GaAs**. J Appl Phys **69**:4064–4070

54. Irmer G, Siegel W, Kuhnel G, et al (1991) **Determination of the hole concentration and mobility of p-GaP by hall and by raman**

measurements. Semicond Sci Technol **6**:1072–1078

55. Mooradian A, Wright GB (1966) **Observation of the Interaction of Plasmons with Longitudinal Optical Phonons in GaAs**. Phys Rev Lett **16**:999–1001

56. Zekeng S, Prevot B, Schwab C (1988) **Raman Determination of the Faust-Henry Coefficient of GaAs in the 1.9 to 2.7 eV Range at Ordinary and Low Temperatures**. Phys status solidi **150**:65–72

57. Kong XT, Besteiro L V., Wang Z, Govorov AO (2018) **Plasmonic Chirality and Circular Dichroism in Bioassembled and Nonbiological Systems: Theoretical Background and Recent Progress**. Adv Mater **1801790**:1–14

58. Piotrowska A (1993) **Ohmic Contacts to GaAs: Fundamentals and Practice**. Acta Phys Pol A **84**:491–504

59. Cox RH, Strack H (2002) **Ohmic contacts for GaAs devices**. Solid State Electron **10**:1213–1218

60. Joannopoulos JD, Cohen ML (1974) **Intrinsic surface states of (110) surfaces of group IV and III-V semiconductors**. Phys Rev B **10**:5075–5081

61. Dinan JH, Galbraith LK, Fischer TE, Haven N (1971) **Electronic properties of clean cleaved {110} GaAs surfaces**. Surf Sci **26**:587–604

62. Allen LTP, Weber ER, Washburn J, Pao YC (1987) **Device quality growth and characterization of (110) GaAs grown by molecular beam epitaxy**. Appl Phys Lett **51**:670–672

63. Newman N, Van Schilfgaarde M, Kendelwicz T, et al (1986) **Electrical study of Schottky barriers on atomically clean GaAs(110) surfaces**. Phys Rev B **33**:1146–1159

64. Mohney SE, Wang Y, Cabassi MA, et al (2005) **Measuring the specific contact resistance of contacts to semiconductor nanowires**. Solid State Electron **49**:227–232

65. Park H, Beresford R, Hong S, Xu J (2010) **Geometry- and size-**

dependence of electrical properties of metal contacts on semiconducting nanowires. J Appl Phys **108**:094308

66. Leahu G, Petronijevic E, Belardini A, et al (2017) **Photo-acoustic spectroscopy revealing resonant absorption of self-assembled GaAs-based nanowires**. Sci Rep **7**:2833

67. Zhang Y, Fonseka HA, Aagesen M, et al (2017) **Growth of pure zinc-blende GaAs(P) core-shell nanowires with highly regular morphology**. Nano Lett **17**:4946–4950

68. Cirlin GE, Dubrovskii VG, Samsonenko YB, et al (2010) **Self-catalyzed, pure zincblende GaAs nanowires grown on Si(111) by molecular beam epitaxy**. Phys Rev B **82**:035302

69. Krogstrup P, Curiotto S, Johnson E, et al (2011) **Impact of the liquid phase shape on the structure of III-V nanowires**. Phys Rev Lett **106**:1–4

70. Jacobsson D, Panciera F, Tersoff J, et al (2016) **Interface dynamics and crystal phase switching in GaAs nanowires**. Nature **531**:317–322

71. Wenzel M, Irmer G, Monecke J, Siegel W (1997) **Hole mobilities and the effective Hall factor in p-type GaAs**. J Appl Phys **81**:7810–7816

72. Baca A., Ren F, Zolper J., et al (1997) **A survey of ohmic contacts to III-V compound semiconductors**. Thin Solid Films **308**:599–606

73. Stareev G (1993) **Formation of extremely low resistance Ti/Pt/Au ohmic contacts to p -GaAs**. Appl Phys Lett **62**:2801–2803

74. Zhang Z, Yao K, Liu Y, et al (2007) **Quantitative analysis of current-voltage characteristics of semiconducting nanowires: Decoupling of contact effects**. Adv Funct Mater **17**:2478–2489

75. Küpers H, Lewis RB, Tahraoui A, et al (2018) **Diameter evolution of selective area grown Ga-assisted GaAs nanowires**. Nano Res **11**:2885–2893

76. Ivanov SV, Kop'ev PS, Ledentsov NN (1991) **Interplay of beryllium segregation and diffusion in heavily doped GaAs and AlGaAs grown**

by molecular beam epitaxy (thermodynamic analysis). J Cryst Growth **108**:661–669

77. Czaban J a., Thompson D a., LaPierre RR (2009) **GaAs core-shell nanowires for photovoltaic applications**. Nano Lett **9**:148–154

78. Tell B, Martin RJ (1967) **Raman Scattering by Coupled Optical-Phonon-Plasmon Modes in GaAs**. Phys Rev **167**:

79. Olson CG, Lynch DW (1969) **Longitudinal-optical-phonon-plasmon coupling in GaAs**. Phys Rev **177**:1231–1234

80. Mintairov AM, Blagnov PA, Melehin VG, et al (1997) **Ordering effects in Raman spectra of coherently strained GaAs(1-x)N(x)**. Phys Rev B **56**:15836–15841

81. Farrow RL, Chang RK, Mroczkowski S, Pollak FH (1977) **Detection of excess crystalline As and Sb in III-V oxide interfaces by Raman scattering**. Appl Phys Lett **31**:768–770

82. Yazji S, Zardo I, Soini M, et al (2011) **Local modification of GaAs nanowires induced by laser heating**. Nanotechnology **22**:325701

83. Chiquito AJ, Amorim C a, Berengue OM, et al (2012) **Back-to-back Schottky diodes: the generalization of the diode theory in analysis and extraction of electrical parameters of nanodevices**. J Phys Condens Matter **24**:225303

84. Koelling S, Li A, Cavalli A, et al (2017) **Atom-by-Atom Analysis of Semiconductor Nanowires with Parts Per Million Sensitivity**. Nano Lett **17**:599–605

85. Koelling S, Plantenga RC, Hauge HIT, et al (2016) **Impurity and Defect Monitoring in Hexagonal Si and SiGe Nanocrystals**. ECS Trans **75**:751–760

86. Collins DM, Miller JN, Chai YG, Chow R (1982) **Sn and Te doping of molecular beam epitaxial GaAs using a SnTe source**. J Appl Phys **53**:3010–3018

PUBLICATIONS

PUBLICATION I

Gradients of Be-dopant concentration in self-catalyzed GaAs nanowires

Marcelo R. Piton, Eero Koivusalo, Teemu Hakkarainen, Helder V. A. Galeti, Ariano D. G. Rodrigues, Soile Talmila, Sergio Souto, Donald Lupo, Yara G. Gobato and Mircea Guina

Nanotechnology 30:335709 (2019)
DOI: 10.1088/1361-6528/ab1a97

IOP Publishing Nanotechnology
Nanotechnology 30 (2019) 335709 (11pp) https://doi.org/10.1088/1361-6528/ab1a97

Gradients of Be-dopant concentration in self-catalyzed GaAs nanowires

Marcelo Rizzo Piton[1,2,7], Eero Koivusalo[2], Teemu Hakkarainen[2], Helder Vinicius Avanço Galeti[3], Ariano De Giovanni Rodrigues[1], Soile Talmila[2], Sergio Souto[4], Donald Lupo[5], Yara Galvão Gobato[1,6] and Mircea Guina[2]

[1] Physics Department, Federal University of São Carlos, São Carlos-SP, Brazil
[2] Optoelectronics Research Centre, Physics Unit, Tampere University, Tampere, Finland
[3] Electrical Engineering Department, Federal University of São Carlos, São Carlos-SP, Brazil
[4] FZEA/ZAB, University of São Paulo, Pirassununga-SP, Brazil
[5] Electronics and Communications Engineering, Tampere University, Tampere, Finland
[6] High Field Magnetic Laboratory, Radboud University, The Netherlands

E-mail: marcelo.rizzopiton@tuni.fi

Received 20 February 2019, revised 9 April 2019
Accepted for publication 17 April 2019
Published 24 May 2019

Abstract

Effective and controllable doping is instrumental for enabling the use of III–V semiconductor nanowires (NWs) in practical electronics and optoelectronics applications. To this end, dopants are incorporated during self-catalyzed growth via vapor–liquid–solid mechanism through the catalyst droplet or by vapor–solid mechanism of the sidewall growth. The interplay of these mechanisms together with the competition between axial elongation and radial growth of NWs can result in dopant concentration gradients along the NW axis. Here, we report an investigation of Be-doped p-type GaAs NWs grown by the self-catalyzed method on lithography-free Si/SiO_x templates. The influence of dopant incorporation on the structural properties of the NWs is analyzed by scanning and transmission electron microscopy. By combining spatially resolved Raman spectroscopy and transport characterization, we are able to estimate the carrier concentration, mobility and resistivity on single-NW level. We show that Be dopants are incorporated predominantly by vapor–solid mechanism for low Be flux, while the relative contribution of vapor–liquid–solid incorporation is increased for higher Be flux, resulting in axial dopant gradients that depend on the nominal doping level.

Supplementary material for this article is available online

Keywords: nanowires, GaAs, Be doping, concentration profiles

(Some figures may appear in colour only in the online journal)

1. Introduction

Semiconductor III–V nanowires (NWs) have emerged due to their unique properties and development opportunities they render possible to a wide range of optoelectronics devices [1, 2], such as LEDs [3, 4], solar cells [5, 6], and photodetectors [7]. The one-dimensional NW geometry brings specific advantages including the possibility to combine different semiconductor alloys as radial and axial heterostructures, and relaxes the lattice matching requirements; in turn, this enables III–V semiconductor NW growth on dissimilar substrates such as Si [1] which is widely used in electronics. Going into more details of the fabrication of such NWs, the self-catalyzed growth [8, 9] has been adopted for direct epitaxial integration because it avoids the use of foreign catalyst metals such as Au, which is known to form deep traps in Si and therefore degenerate device performance [10]. Substantial progress has been made recently in self-catalyzed

[7] Author to whom any correspondence should be addressed.

growth of GaAs NWs with high control of the size distributions and crystalline structure [11–16]. Moreover, the ability to achieve an effective and controllable doping is essential for bringing these nanostructures to the realm of practical applications, for example enabling formation of p–n junctions without compromising the material quality of the NWs. It should be emphasized that the knowledge of the dopant incorporation in traditional thin film (TF) epitaxy cannot be directly applied to NW growth. Therefore, significant effort has been dedicated to investigate the dopant incorporation mechanisms in NW growth [17]. The dopants are incorporated in NWs either via vapor–liquid–solid (VLS) mechanism through the catalyst droplet, or via vapor–solid (VS) mechanism during the sidewall growth. The incorporation of p-type dopant Be into GaAs NWs during self-catalyzed growth has been investigated by several groups and different incorporation mechanisms have been reported. Casadei *et al* reported a preferential VS Be incorporation via the NWs sidewalls [18]. Zhang *et al* proposed a predominance of Be incorporation through the Ga catalyst droplets [19] and in the work of Dastjerdi *et al* it was determined that Be dopants incorporated through truncated facets under the Ga droplet followed by diffusion into the core of the NWs [20]. These previous studies suggest that the Be incorporation strongly depends on the growth conditions.

Here, we report an investigation of Be-doped self-catalyzed GaAs NWs grown on lithography-free Si/SiO_x templates fabricated by droplet epitaxy and spontaneous oxidation of Si substrates [11, 12]. We examine the microstructural changes caused by Be-dopant incorporation and, in particular, assess the dopant concentration and its axial variations by single-NW Raman and electrical characterization techniques, respectively. We show that different axial gradients of Be concentration are formed for different Be fluxes. Our results suggest that the predominant Be incorporation mechanism is VLS for high Be flux and VS for low Be flux.

2. Experimental methods

The self-catalyzed GaAs NWs were grown by solid-source molecular beam epitaxy (MBE) on lithography-free oxide patterns fabricated on p-Si(111) substrates by droplet epitaxy and spontaneous oxidation. GaAs droplet epitaxy was performed on oxide-free HF-etched substrates. After the droplet epitaxy, the wafers were removed from the MBE reactor, oxidized in air and loaded back to the MBE. Prior to NW growth, the samples were annealed for 30 min at 655 °C, as determined by pyrometer, in order to evaporate the GaAs mounds and to reveal oxide-free holes for NW nucleation as described in detail in [12]. The nucleation site density of the templates used was $2 \times 10^8\,cm^{-2}$. The annealing was followed by a 60 s Ga pre-deposition at the NW growth temperature of 640 °C with Ga flux corresponding to planar $0.3\ \mu m\,h^{-1}$ growth rate on GaAs(100). The NW growth was then initiated by providing As_2 corresponding to a V/III beam equivalent pressure ratio of 9. The NWs were grown for 60 min and the growth was terminated by switching off all fluxes simultaneously and rapidly cooling down the sample. The NWs were doped with Be fluxes corresponding to a nominal p-type dopant concentrations of $2.0 \times 10^{18}\,cm^{-3}$ and $2.0 \times 10^{19}\,cm^{-3}$ for samples hereafter named Be1 and Be2, respectively. The doping levels were calibrated based on Hall measurements of three planar Be-doped GaAs(100) samples grown on semi-insulating GaAs substrates. The TF samples were later used for comparing the carrier concentration and mobility values obtained from Raman spectroscopy and Hall measurements, and will be from now on named TF1, TF2 and TF3, in the order of increasing Be flux used during the growth.

The structural properties of NWs were characterized by scanning electron microscopy (SEM) and transmission electron microscopy (TEM). SEM characterization was performed to collect dimensional data and to obtain images of the NWs used for Raman spectroscopy and transport characterization after the measurements were carried out. TEM was used to analyze the microstructure of single NWs harvested from the as-grown samples to a carbon film of a Cu TEM grid; for the analyses we used a FEI Tecnai G2-F20 operating at 200 kV.

Room temperature Raman spectra of single NWs were obtained on backscattering geometry. The NWs were transferred to a Si substrate with a 200 nm SiO_2 thermal oxide layer. The excitation wavelength was 532 nm and a 50× magnification lens with NA = 0.82 was used to obtain a spot size of $<1\ \mu m$ in diameter. Raman spectra with varying excitation power were first collected from test NWs to select the optimal power density that would not result in any shifts or broadening of Raman peaks due to laser-induced heating. The linear polarization of both excitation laser and scattered light were adjusted perpendicular to the NW growth axis. The TF samples were also investigated by Raman spectroscopy with equivalent configuration of linear polarizations of excitation and detection to evaluate the methodology adopted on analysis of the Raman spectra for assessing the free carrier concentration and mobility.

For single-NW transport characterization, the NWs were first drop-casted on a p-GaAs substrate covered by a 200 nm SiO_2 layer with pre-patterned gold pads. The position of representative NWs on the substrate were identified by SEM imaging and electron beam lithography was used to fabricate electrical contacts on individual NWs. After resist development, the sample was dipped in 1:10 $HCl:H_2O$ solution for 10 s to remove the native oxide, followed by 15% ammonium polysulfide $(NH_4)2S_x$ diluted in H_2O for chemical passivation (45 °C, 3 min) of the exposed contact area of the NWs. After chemical treatments of the surface, the NWs were immediately taken to an electron beam metal evaporation equipment and a Pt/Ti/Pt/Au (5/10/10/200 nm) metallic multilayer was deposited on the sample. After lift-off of the resist, a rapid thermal annealing at 400 °C for 30 s was performed to reduce the contacts resistance. Current–voltage (*IV*) measurements were carried using an Agilent Source-Meter Unit.

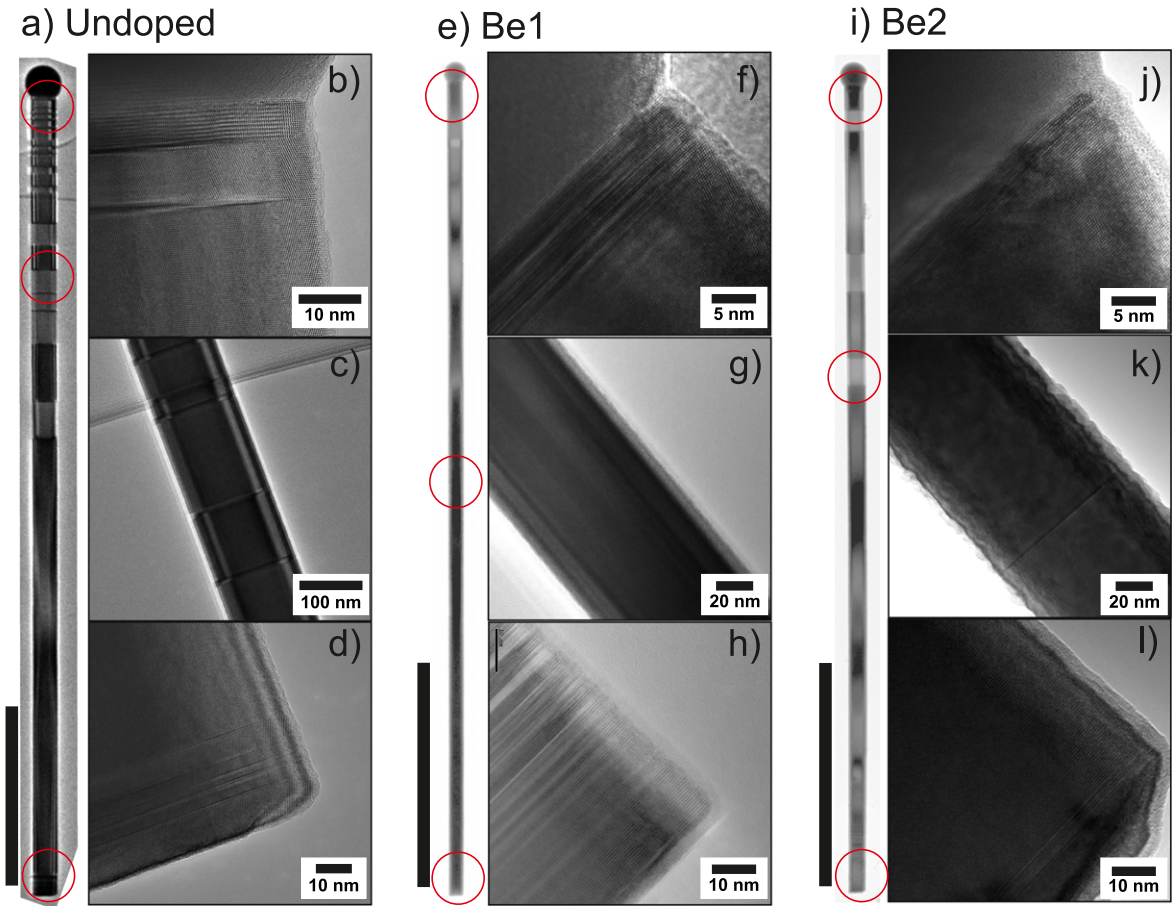

Figure 1. HR-TEM images of (a)–(d) undoped, (e)–(h) Be1, and (i)–(l) Be2 NWs. The red circles in (a), (e) and (i) indicate the different positions corresponding to the higher magnification images in (b)–(d), (f)–(h) and (j)–(l). The scale bars are 1 μm in (a), (e) and (i). The other scale bars sizes are indicated on each figure.

3. Results and discussion

3.1. Structural properties

TEM and HR-TEM images from selected areas of undoped and Be-doped GaAs NWs were obtained to evaluate the influence of Be incorporation on the microstructural properties of the NWs. The results are summarized in figures 1(a)–(d) for undoped NWs, in figures 1(e)–(h) for Be1 NWs, and in figures 1(i)–(l) for Be2 NWs. The bright-field (BF) TEM image of undoped NW in figure 1(a) shows that the twin plane density increases towards the NW/droplet interface, region at which the contact angle between the Ga droplet and NW tip decreases due to lateral growth favoring the twin plane formation [12]. HR-TEM imaging of the root region in figure 1(d) shows a 100 nm long section of stacking faults and polytypism, followed by a 2 μm long center region of pure zincblend (ZB) GaAs, as shown in figure 1(c). A short wurtzite (WZ) section (~5 nm) was formed at the interface of the Ga droplet and the NW body (figure 1(b)), which is commonly observed in self-catalyzed growth of GaAs NWs due to rapid changes in the growth conditions after switching off the Ga and As fluxes and subsequent ramp down of the sample temperature [12].

The BF images of Be1 and Be2 NWs are shown in figures 1(e) and (i), respectively. The twin plane density at the center-tip regions is smaller than in the undoped sample shown in figure 1(a), which has been previously reported for self-catalyzed Be-doped GaAs NWs [19]. The root regions of Be1 and Be2 NWs, shown in figures 1(h) and (l), are composed of ZB structure with twin planes and stacking faults due to instabilities related to early-stages of the epitaxial growth, such as Ga droplet composition. It is evident that the incorporation of Be suppresses the twin plane formation in the center [figures 1(g) and (k)] and NW-droplet interface [figures 1(f) and (j)] regions when compared to the undoped sample. The formation of twin planes and WZ segments in self-catalyzed GaAs NWs is commonly attributed to the droplet contact angle [9, 21, 22]. However, the post growth analysis of the distributions of droplet contact angles reveals no significant difference between the Be-doped and undoped NWs (see figure S1 in the supplementary data is available online at stacks.iop.org/NANO/30/335709/mmedia). The mean values of contact angles and the standard deviations for Be1, Be2, and undoped NWs are 123.5° ± 4.6°, 126.4° ± 6.2° and 127.8° ± 5.3°, respectively. Furthermore, Be has been reported to suppresses the formation of WZ segments during Ga droplet crystallization [23], which is

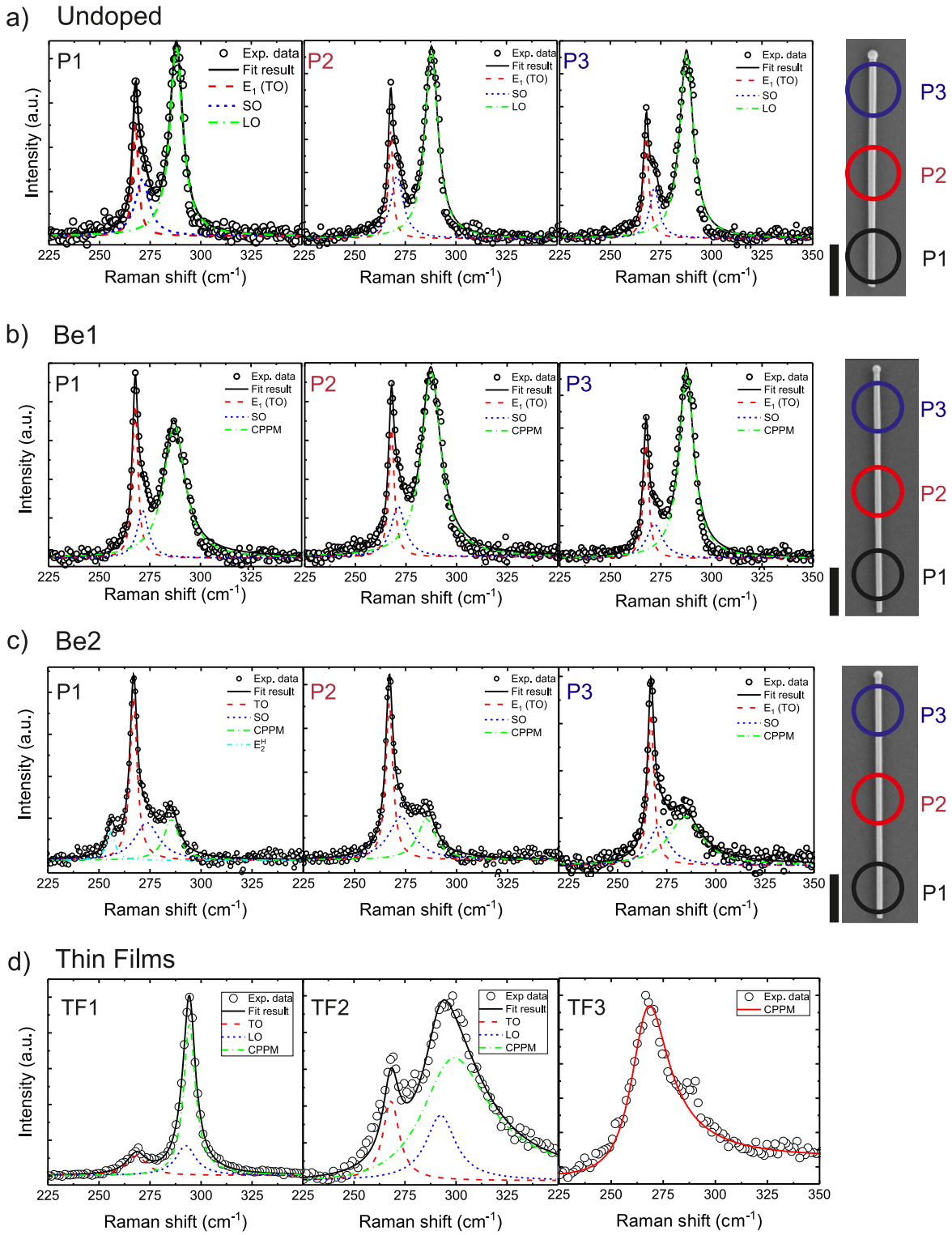

Figure 2. Raman spectra of (a) undoped, (b) Be1, (c) Be2 GaAs NWs, and (d) Be-doped GaAs TF samples. The spectra P1, P2, and P3 were collected from the regions indicated in the SEM pictures of the right sides of (a)–(c). The scale bars in the SEM pictures are 1 μm.

another indication that the influence of Be on the ZB crystal phase purity cannot be explained merely by a change of droplet contact angle. Therefore, the reduction of twinning and WZ stacking probability in the Be-doped NWs is most likely related to a more complex change of energetics in the VLS system, leading to an increase of ZB nucleation probability over WZ stacking and twin formation. Furthermore, the NWs grown with high Be flux [Be2 in figure 1(k)] exhibit roughening of the (110) sidewall planes along the whole NW length. The selected area electron diffraction patterns

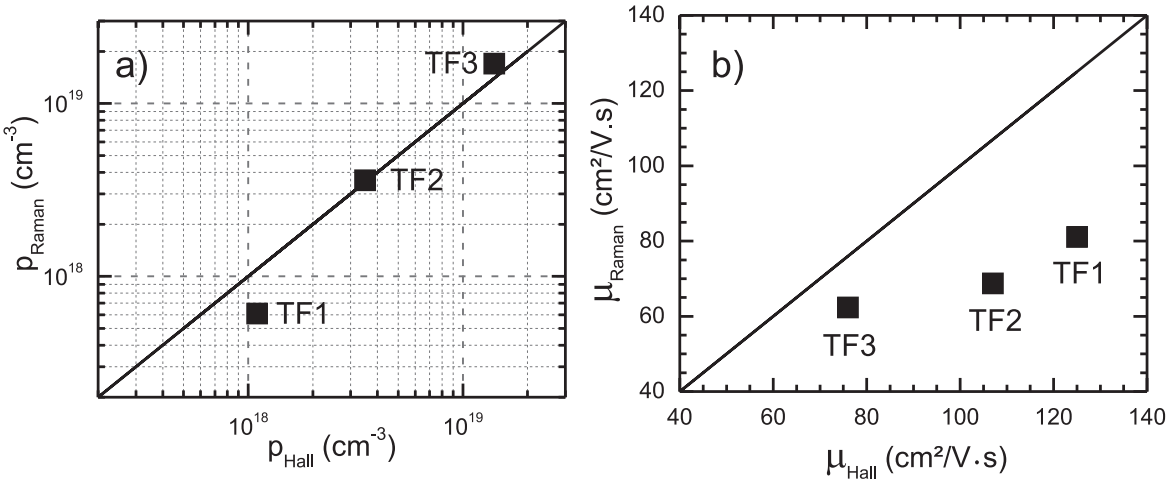

Figure 3. (a) Carrier concentration and (b) hole mobility comparison between Hall effect data and fit of CPPM peak from Raman spectra of TF samples. The symbols represent the fit results and the solid lines, indicating one-to-one relation between Hall and Raman values, are for illustrational purposes.

corresponding to the HR-TEM images of the bottom, center and tip regions of undoped, Be1 and Be2 NWs can be found in figure S2 in the supplementary data.

3.2. Raman spectroscopy

Single-NW Raman spectroscopy with microscopic resolution allows to investigate the effect of Be doping in different regions of the NW. Figure 2 shows Raman spectra of undoped, and two samples of Be-doped NWs (namely Be1 and Be2) collected from three different positions along the NW axes. The decomposition of the experimental data in Lorentzian peaks of undoped NWs in figure 2(a) reveals the transversal optical (TO), the surface optical (SO) and the longitudinal optical (LO) vibration modes of ZB GaAs centered at 268, 272 and 288 cm^{-1}, respectively. The SO modes are commonly observed in nanostructures with high surface-to-volume ratio. Its frequency depends on the surrounding medium [24] and density of defects, such as twin planes [25]. It was also reported that doping does not affect SO mode frequency and linewidth [25]. It is worth mentioning that LO is a forbidden mode in Raman backscattering from (110) surface of ZB crystals [26], but this selection rule is relaxed to some extent for NWs due to finite size effects and hexagonal geometry of the cross-section [24]. This allows to analyze the screening of the LO mode due to the presence of free carriers caused by Be incorporation on the NWs lattice [27].

In doped polar semiconductors, such as GaAs, the LO mode can couple to collective oscillations of free carriers producing a coupled-phonon-plasmon mode (CPPM) [28]. The line shape analysis of the CPPM can be used to estimate the free carriers concentrations and holes mobility for p-type GaAs epilayers [28, 29] and NWs [18, 27, 30, 31]. The Raman scattering intensity of the CPPM can be described by [32]:

$$I(\omega) = A\omega\Gamma_p\omega_p[\omega_{TO}^2(1+C) - \omega^2]^2/D \qquad (1)$$

with:

$$D = [\omega^2(\omega_{LO}^2 - \omega^2) - \omega_p^2(\omega_{TO}^2 - \omega^2) + \gamma\Gamma_p\omega^2]^2 + [\Gamma_p\omega(\omega_{LO}^2 - \omega^2) + \gamma\omega(\omega_p^2 - \omega^2)]^2. \qquad (2)$$

In this formulation, ω_{TO} and ω_{LO} are the TO and LO wavenumbers of an undoped reference sample respectively, A is a frequency independent parameter, $C = -0.49$ is the Faust–Henry coefficient for GaAs at room temperature for 532 nm laser excitation [33] and γ is the natural LO mode damping constant. The hole mobility μ_p can be calculated from the plasmon-damping constant $\Gamma_p = e/\mu_p m_p^*$ and the free carrier concentration p is obtained from the plasma oscillation frequency of the free carriers $\omega_p^2 = pe^2/\epsilon_0\epsilon_\infty m_p^*$. The remaining symbols have the usual meanings: e is the elementary electron charge, $m_p{}^*$ is the hole effective mass, ε_∞ is the high-frequency dielectric constant for GaAs and ε_0 is the vacuum permittivity.

Figures 2(b) and (c) show Raman spectra measured at three different positions of representative Be1 and Be2 NWs respectively. The figures include the spectral components related to TO, SO and CPPM modes that best fit the experimental data. On the right side are the corresponding SEM images indicating the region of the NW from where Raman spectra were measured. The TO peak positions and linewidths are consistent with the undoped sample and the SO position is in accordance to the NW diameters and stacking faults/twin plane densities [24, 25] observed in the HR-TEM images. The spectral position and linewidth of the CPPM mode is dependent on the carrier concentration and mobility [28]. The Raman peak at 256 cm^{-1} observed at the root section (P1) of Be2 NW in figure 2(c) corresponds to E_2^H TO mode of WZ phase of GaAs [34] which is consistent with the results from the HR-TEM in figure 1(l).

In order to evaluate the fit method applied to the Be1 and Be2 NWs, we analyzed the Raman spectra of TF samples considering the contribution of CPPM calculated through

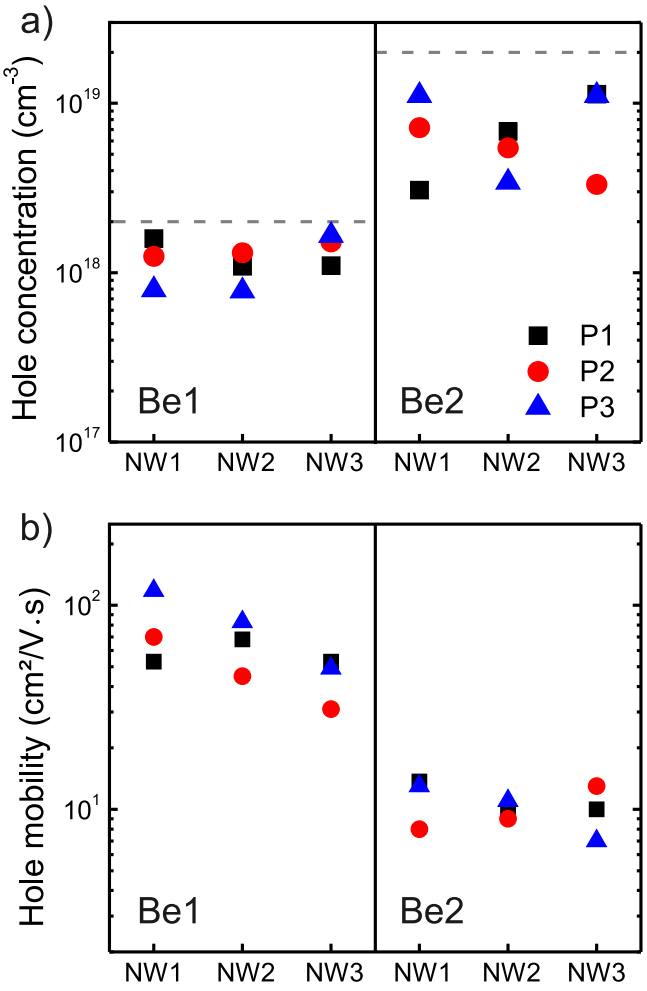

Figure 4. (a) Hole concentration and (b) hole mobility, obtained from the fit of CPPM line shape to the Raman spectra for three different NWs extracted from Be1 and Be2 samples. The NW1 data points in (a) and (b) corresponds to the spectra presented in figures 2(b) and (c), respectively. The spectra corresponding to the NW2 and NW3 data points are shown in figure S3. The symbols represent the different positions of the NWs from which the Raman spectrum was measured: bottom region (P1), center region (P2) and tip region (P3). The grey dashed lines (a) represent the nominal Be concentration of each sample.

equation (1) and comparing the results with the Hall effect data. The results are summarized in figure 3 for the carrier concentration (figure 3(a)) and the hole mobility (figure 3(b)). The carrier concentrations obtained from Raman and Hall effect experiments in figure 3(a) are in good agreement, whereas the hole mobilities in figure 3(b) are clearly underestimated by Raman spectroscopy when compared with the Hall effect data. Similar results were previously reported for Zn-implanted GaAs [28] and p-type GaP [35]. In [35] the differences between values of hole mobility estimated by Raman and Hall effect are attributed to the contributions of several other factors that may cause an apparent decrease in the hole mobility at room temperature estimated by Raman spectroscopy, such as non-polar optical and acoustic phonons, polar optical phonons and ionized impurities [35, 36].

By applying the same fitting procedure to the spectra in figures 2(b) and (c), we calculated the charge carrier concentrations and the hole mobilities of three representative NWs of each nominal doping level. The results of carrier concentration and hole mobility are presented in figures 4(a) and (b), respectively. The Raman spectra of the additional NWs from Be1 and Be2 samples are included in figure S3 in the supplementary data. The dashed lines in figure 4(a) represent the nominal doping level of Be1 and Be2 samples. The hole concentrations from the NWs in figure 4(a) ranges from 8×10^{17} to 1.6×10^{18} cm^{-3} for Be1 NWs (nominal 2×10^{18} cm^{-3}) and from 3.4×10^{18} to 1.1×10^{19} cm^{-3} for Be2 NWs (nominal 2×10^{19} cm^{-3}). There is no consistent spatial dependence of Be concentration that would suggest a doping profile along the NW axis, but the variation of values obtained for different axial positions are rather large for all investigated NWs. Some uncertainty of the fitting results is expected due to overlapping of TO, SO and CPPM. As the dopant concentration increases, the CPPM mode gets broader and shifts to frequencies closer to the TO mode of ZB GaAs [28], which increases the uncertainty of the line shape analysis in which equation (1) is used as a component for spectral decomposition. Nevertheless, the fitting results were consistent with the same methodology applied to the TF samples supported by Hall effect measurements in figure 3.

The carrier concentrations of Be1 and Be2 NWs are shown in figure 4(a) and are compared with the nominal dopant concentrations, which are indicated by the dashed grey lines. On average, the carrier concentration of Be1 NW is 60% from the nominal doping whereas Be2 NW present 35% of the nominal doping level. Similar incorporation efficiency of Be-dopant in self-catalyzed GaAs NWs has been reported [30]. It is important to highlight that the Be fluxes used for nominal doping of the NWs are based on Hall effect data obtained from the (100) oriented GaAs epilayers and the Be incorporation rates are expected to be different for VS incorporation at the (110) oriented NW sidewalls and for the VLS mechanism through the droplet [18–20]. Moreover, the results from Be1 and Be2 NWs suggest a reduction of the incorporation efficiency at higher Be flux. On the other hand, the hole mobilities [figure 4(b)] obtained for Be1 NW are similar to the values from Raman spectroscopy of the TF samples having similar carrier concentration. However, the values obtained for the mobility of Be2 NWs were significantly lower than what is expected for similar dopant concentration of bulk Be-doped GaAs at room temperature. Similar result was also observed in Be-doped GaAs NWs and ascribed to scattering at the surface [27] that would considerably decrease the mean free path of the carriers. It should be noted that the charge carriers in highly doped NWs are expected to be more affected by the surface due to the small depletion layer width [18].

3.3. Transport properties

The spatial dependence of the transport properties of individual Be-doped NWs was investigated by manufacturing

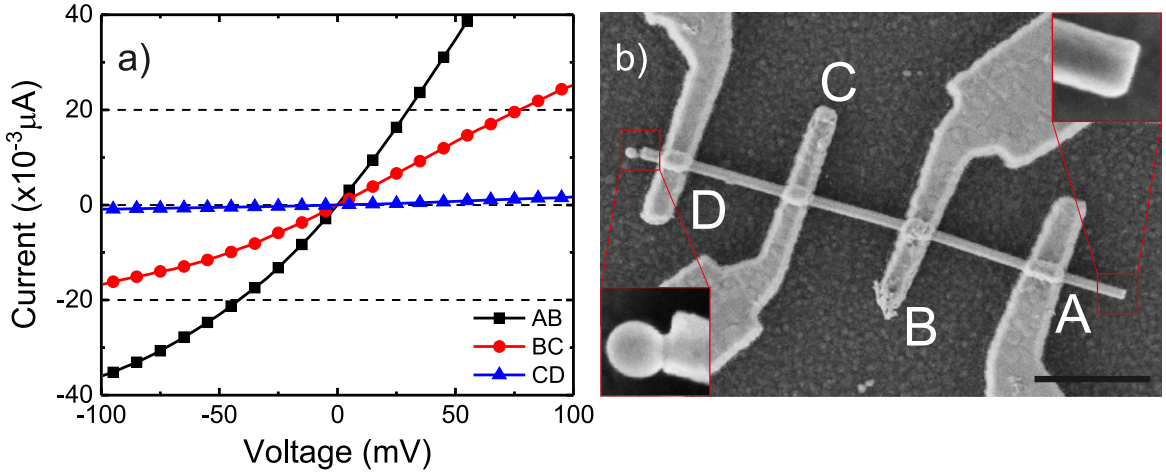

Figure 5. (a) *IV* characteristics of different channels along Be1 NW. (b) SEM image of measured device. Each channel in (a) corresponds to a pair of contacts as indicated in (b), with A being at the bottom and D at the tip region of the NW. The scale bar in (b) is 1 μm. The insets in (b) show higher magnification SEM pictures of the bottom (contact A) and tip (contact D) of the NW.

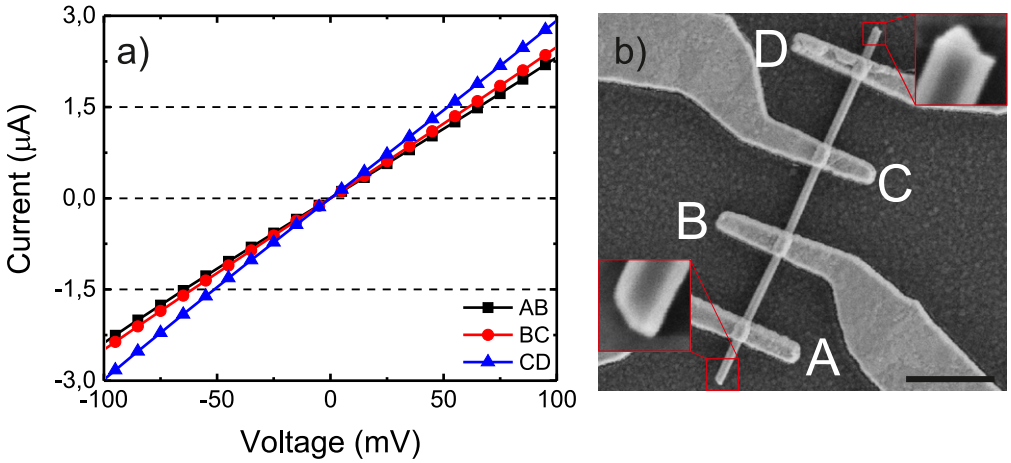

Figure 6. (a) *IV* characteristics of different channels along Be2 NW. (b) SEM image of measured device. Each channel in (a) corresponds to a pair of contacts as indicated in (b), with A being at the bottom and D at the tip region of the NW. The scale bar in (b) is 1 μm. The insets in (b) show higher magnification SEM pictures of the bottom (contact A) and tip (contact D) of the NW.

evenly spaced contacts and analyzing the *IV* characteristics of each channel along the NWs. Figure 5(a) shows representative *IV* curves from Be1 sample and the corresponding SEM image of the device in figure 5(b). The asymmetric *IV* indicate a Schottky-like behavior of the metal–semiconductor contacts. The current values in different positions along the Be1 NW in figure 5(a) indicate an increase in the values of the Schottky barrier heights in the contacts from the bottom (AB channel) to tip (CD channel) of the NW. This behavior can be associated to a dopant concentration profile which decreases from the root toward the tip of the NW. Such behavior was observed consistently for all investigated Be1 NWs, as shown in figures S4(a) and (e) in the supplementary data. It should be noted that most of the Ga droplets were removed in the contact fabrication process, unlike in the case of the NW shown in figure 5. In those cases, the bottom end of the NW was identified from the specific off-cut shape formed when the NWs were harvested from the substrate. The insets in figure 5(b) show higher magnification SEM pictures of the bottom (contact A) end with the off-cut shape and tip end (contact D) of the NW. More details can be found in figures S4, S5 and S6 in the supplementary data.

Figure 6 shows similar *IV* curves for Be2 NWs. In contrast to Be1, the *IV* curves are linear and exhibit smaller differences in the current values between different channels. This also confirms that the surface passivation by ammonium polysulfide and the choice of the metal layers used for device processing were successful in achieving ohmic contacts to p-GaAs NWs. The bottom (channel AB) and tip (channel CD) parts of the NW without the Ga droplet in figure 6(b) were identified by the same method previously described. The insets in figure 6(b) show higher magnification SEM pictures of the bottom (contact A) end with the off-cut shape and tip end (contact D) of the NW. The slope in the *IV* curve depends

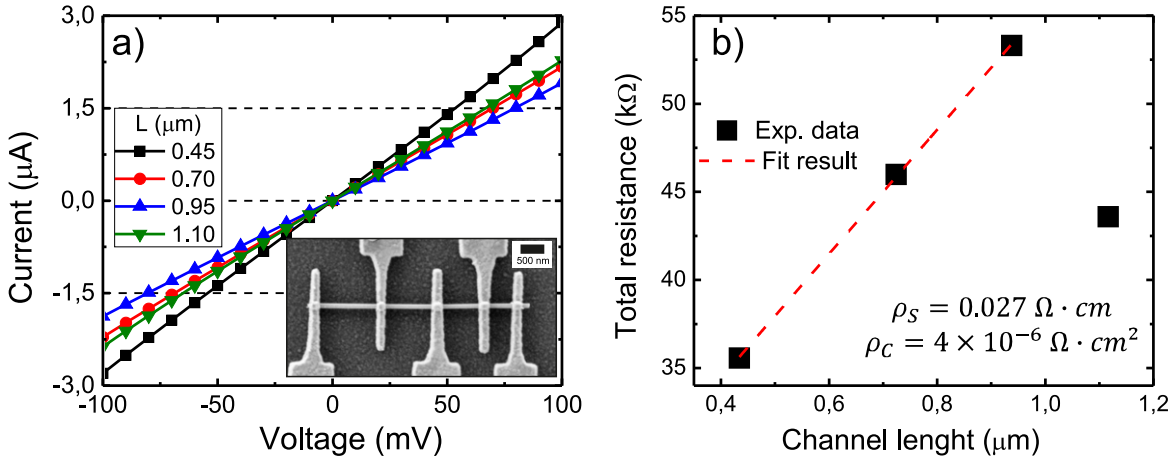

Figure 7. (a) *IV* characteristics of Be2 NW measured in TLM geometry. The inset shows a SEM image of the measured device. The scale bar is 500 nm. (b) Total resistances of individual channels as a function of channel length. The square points are obtained from the linear fit to the *IV* curves in (a) and the red dashed line is the fit result using equation (3).

on both contact resistance and semiconductor resistivity. Therefore, in the following we present another transport experiment for distinguishing these two values.

The ohmic character of the *IV*s from Be2 NWs allowed us to estimate simultaneously the contact specific resistance and the semiconductor resistivity by fabricating five electrical contacts with increasing channel length along the NW axial direction, also known as transmission line model (TLM) geometry [37]. In this configuration, the total resistance R_T of each channel was obtained from the slope of the *IV* curves and plotted as a function of channel length, the NW resistivity ρ_s and transfer length L_T were then obtained by fitting the pairs (R_T, L) using the relation [37, 38]:

$$R_T(L) = \frac{\rho_s}{\pi r^2}\left(2L_T \coth\left(\frac{W_C}{L_T}\right) + L\right), \quad (3)$$

where W_C is the contact width and r is the NW radius obtained by SEM imaging of the devices after transport measurements. This equation format was chosen over a linear fit of the experimental points to account for the reduced contacts width used in our devices due to NW length limitations [37]. The specific contact resistance ρ_c can be obtained from the equation:

$$\rho_c = \frac{3}{2}\frac{\rho_s}{r}L_T^2, \quad (4)$$

where the pre-factor 3/2 accounts for the fact the metal contact layer is not covering the whole NW surface [37]. The specific contact resistance obtained from TLM devices allowed us to calculate the NW resistivity of the devices similar to presented in figure 6(a) by using equation (5):

$$R_T = \rho_S \frac{L}{A} + 2R_C, \quad (5)$$

where A is the hexagonal cross-section area of the NW.

Figure 7(a) shows the *IV* of different channel lengths of Be2 NW in the TLM geometry, the inset shows the SEM picture of the device obtained after transport measurements. The total resistance of the longer channel ($L = 1.10\ \mu$m) was

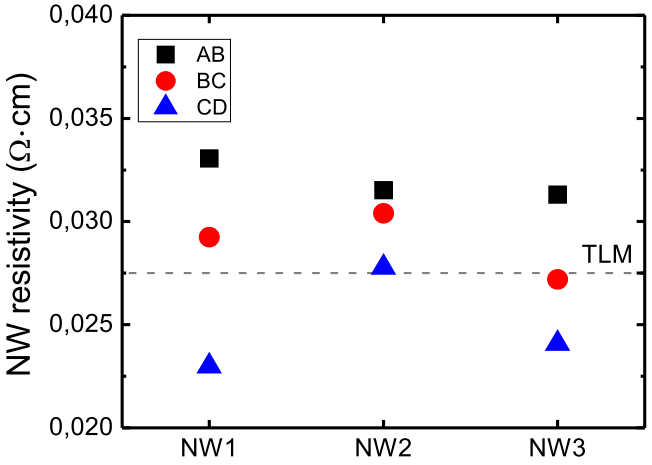

Figure 8. Nanowire resistivity of Be2 NWs from devices similar to presented in figure 6(a). The experimental points were calculated using equation (5) for each channel along the NW length, with A being at the bottom and D at the tip region of the NW. The dashed line indicates the NW resistivity value obtained by TLM.

unexpectedly smaller than the shorter center channels most likely as a result of the contact overlap with one of the ends of the NW, resulting in smaller contact resistance. Therefore, this data point is omitted from the fitting procedure. The fitting to the experimental data in figure 6(b) resulted in NW resistivity of $\rho_S = 0.027\ \Omega$ cm and specific contact resistance of $\rho_C = 4.5 \times 10^{-6}\ \Omega\ \text{cm}^2$, the transfer length resulting from the best-fit values was $L_T = 230$ nm. Based on the values of ρ_C obtained, the total contact resistance for each channel is 18 kΩ on average. Comparable results of contact resistance were previously reported for Zn-implanted p-type GaAs NWs with similar metal contact multilayer [39] and Be-doped GaAs TFs [40].

With the specific contact resistance value now determined, we are able to calculate the semiconductor resistivity for each channel of the evenly spaced contacts shown in figure 6 (NW1) and other NWs from the same sample (NW2 and NW3, figure S5 of supplementary data) using

equation (5). The NW diameters were measured by SEM images obtained after transport measurements and a hexagonal cross-section area was considered. Figure 8 shows the resistivity from channels AB (bottom region), BC (center region) and CD (tip region) of NW1, NW2 and NW3. The NW resistivity obtained from TLM is represented by the dashed line for comparison. The resistivity values range from 0.023 Ω cm to 0.033 Ω cm. It should be noted that the TLM calculations are based on NWs with circular cross-sections [37] whereas the resistivity was calculated assuming more realistic hexagonal cross-section for the devices with evenly spaced contacts. This explains slight deviation of the resistivity values obtained from the two methods, as can be seen from figure 8. Nevertheless, the resistivity calculated for the evenly spaced contacts allows us to investigate the Be concentration gradient in the axial direction for Be2 NWs. While there is some NW-to-NW variation in the resistivity values, we consistently observe lower resistivity for the upper part than for the lower part of the NW, indicating axial Be concentration gradient which increases towards the tip, which is contrary to what was observed for Be1.

From the *IV* analysis of the NW devices in figures 5(a), 6(a) and 8 it is clear that the Be-dopant gradient is opposite in Be1 and Be2 samples grown with lower and higher Be flux, respectively. The *IV* data of Be1 indicates a dopant gradient with decreasing concentration from bottom to tip. The thickness of the VS grown shell is larger at the bottom than at the tip region of the NW, as the NWs grow constantly in thickness but are not tapered [13, 41]. Thus, in sample Be1, the Be dopants incorporate predominantly through the NW sidewalls via VS growth, as reported in [18]. Predominant Be incorporation via VLS mechanism through the Ga droplet would result in a dopant gradient which increases from bottom to tip [19, 20], as the thickness of the VLS grown core increases from bottom to tip [41]. This is indeed what we observe for Be2. Therefore, we conclude that the predominant dopant incorporation pathway depends on the Be flux so that lower Be fluxes favorably incorporate via VS growth and higher fluxes via VLS growth. In case of the lower Be flux, the VLS incorporation can be limited by capture of Be atoms only by direct impingement to the Ga droplet, while the axial VLS growth rate is more than 10-times larger than the nominal growth rate of 0.3 μm h^{-1} for which the nominal doping level is calibrated, thus leading the predominant VS incorporation. As for the high Be flux, it should be noted that, according to the Raman results shown in figure 4(a), the total incorporation efficiency decreases when the Be flux is increased. Therefore, the difference between the dopant gradients of Be1 and Be2 NWs is more likely due to a reduction of the VS incorporation than an increase of the VLS incorporation when the Be flux is increased. Such saturation of the VS incorporation can be attributed to the onset of Be segregation on the GaAs surface. In the planar VS growth of Be-doped GaAs, the segregation at high Be fluxes causes an increase of surface roughness [42–44], which is indeed observed in figure 1(k) in the TEM micrographs of the NWs grown with high Be flux. When planar layers are grown by VS with typical 1 μm h^{-1} growth rates, the segregation effects are expected at high doping levels in the 10^{19}–10^{20} cm^{-3} range. However, the radial growth rate on the NW sidewalls by the VS mechanism is significantly lower and, according to the thermodynamic model presented in [43], low growth rates lead to an onset of segregation at lower doping levels. The same model also predicts that the onset of Be segregation depends on the As flux and growth temperature, which further emphasizes the influence of growth conditions on the Be incorporation in self-catalyzed GaAs NW growth.

4. Conclusions

We have investigated the effect of Be-dopant incorporation in self-catalyzed GaAs NWs using a lithography-free fabrication technique of Si/SiO$_x$ templates. The presence of Be impurities was found to suppress the formation of twin planes and stacking faults in the NWs. Using spatially resolved single-NW Raman spectroscopy and transport characterization, we were able to assess the dopant incorporation and axial dopant gradients formed in NWs grown with higher and lower Be fluxes. We have shown that with low Be flux the dopant concentration decreases towards the NW tip, while for high Be flux the gradient is opposite. These results suggest that the Be dopants incorporate predominantly via VS growth at the NW sidewalls with low Be flux, while the relative contribution of the VLS mechanism becomes more significant when the Be flux is increased.

Acknowledgments

MRP acknowledges CAPES/CNPq process 88887.100549/2015-00, HVAG and YGG acknowledge FAPESP grants 18/01808-5, 16/10668-7 and 14/50513-7. MRP, EK, TH, and MG acknowledge financial support from the Academy of Finland Project NESP (decision number 294630), and NanoLight (decision number 310985) and the Vilho, Yrjö and Kalle Väisälä Foundation of the Finnish Academy of Science and Letters. This work made use of Tampere Microscopy Center facilities at Tampere University.

ORCID iDs

Marcelo Rizzo Piton https://orcid.org/0000-0002-3972-7202
Eero Koivusalo https://orcid.org/0000-0001-5029-4658
Teemu Hakkarainen https://orcid.org/0000-0001-6758-2496
Helder Vinicius Avanço Galeti https://orcid.org/0000-0002-5217-8367
Ariano De Giovanni Rodrigues https://orcid.org/0000-0003-0294-6775
Soile Talmila https://orcid.org/0000-0002-2353-3761
Yara Galvão Gobato https://orcid.org/0000-0003-2251-0426
Mircea Guina https://orcid.org/0000-0002-9317-8187

References

[1] Joyce H J *et al* 2011 III–V semiconductor nanowires for optoelectronic device applications *Prog. Quantum Electron.* **35** 23–75

[2] Zhang A, Zheng G and M Lieber C 2016 *Nanowires: Building Blocks for Nanoscience and Nanotechnology* (New York: Springer International Publishing)

[3] Dimakis E *et al* 2014 Coaxial multishell (In, Ga)As/GaAs nanowires for near-infrared emission on Si substrates *Nano Lett.* **14** 2604–9

[4] Svensson C P T, Mårtensson T, Trägårdh J, Larsson C, Rask M, Hessman D, Samuelson L and Ohlsson J 2008 Monolithic GaAs/InGaP nanowire light emitting diodes on silicon *Nanotechnology* **19** 305201

[5] Aberg I *et al* 2016 A GaAs nanowire array solar cell with 15.3% efficiency at 1 sun *IEEE J. Photovolt.* **6** 185–90

[6] van Dam D, van Hoof N J J, Cui Y, van Veldhoven P J, Bakkers E P A M, Gómez Rivas J and Haverkort J E M 2016 High-efficiency nanowire solar cells with omnidirectionally enhanced absorption due to self-aligned indium–tin-oxide mie scatterers *ACS Nano* **10** 11414–9

[7] Thompson M D *et al* 2016 Low leakage-current InAsSb nanowire photodetectors on silicon *Nano Lett.* **16** 182–7

[8] Colombo C, Spirkoska D, Frimmer M, Abstreiter G and Fontcuberta i Morral A 2008 Ga-assisted catalyst-free growth mechanism of GaAs nanowires by molecular beam epitaxy *Phys. Rev.* B **77** 155326

[9] Cirlin G E *et al* 2010 Self-catalyzed, pure zincblende GaAs nanowires grown on Si(111) by molecular beam epitaxy *Phys. Rev.* B **82** 035302

[10] Bullis W M 1966 Properties of gold in silicon *Solid-State Electron.* **9** 143–68

[11] Hakkarainen T V, Schramm A, Mäkelä J, Laukkanen P and Guina M 2015 Lithography-free oxide patterns as templates for self-catalyzed growth of highly uniform GaAs nanowires on Si(111) *Nanotechnology* **26** 275301

[12] Koivusalo E, Hakkarainen T and Guina M 2017 Structural investigation of uniform ensembles of self-catalyzed GaAs Nanowires fabricated by a lithography-free technique *Nanoscale Res. Lett.* **12** 192

[13] Koivusalo E S, Hakkarainen T V, Guina M D and Dubrovskii V G 2017 Sub-poissonian narrowing of length distributions realized in Ga-catalyzed GaAs nanowires *Nano Lett.* **17** 5350–5

[14] Tauchnitz T, Nurmamytov T, Hübner R, Engler M, Facsko S, Schneider H, Helm M and Dimakis E 2017 Decoupling the two roles of Ga droplets in the self-catalyzed growth of GaAs Nanowires on SiO_x/Si(111) substrates *Cryst. Growth Des.* **17** 5276–82

[15] Tan S L, Genuist Y, den Hertog M I, Bellet-Amalric E, Mariette H and Pelekanos N T 2017 Highly uniform zinc blende GaAs nanowires on Si(111) using a controlled chemical oxide template *Nanotechnology* **28** 255602

[16] Küpers H, Bastiman F, Luna E, Somaschini C and Geelhaar L 2017 Ga predeposition for the Ga-assisted growth of GaAs nanowire ensembles with low number density and homogeneous length *J. Cryst. Growth* **459** 43–9

[17] Dayeh S A, Chen R, Ro Y G and Sim J 2017 Progress in doping semiconductor nanowires during growth *Mater. Sci. Semicond. Process.* **62** 135–55

[18] Casadei A *et al* 2013 Doping incorporation paths in catalyst-free Be-doped GaAs nanowires *Appl. Phys. Lett.* **102** 013117

[19] Zhang Y *et al* 2018 Doping of self-catalyzed nanowires under the influence of droplets *Nano Lett.* **18** 81–7

[20] Dastjerdi M H T, Fiordaliso E M, Leshchenko E D, Akhtari-Zavareh A, Kasama T, Aagesen M, Dubrovskii V G and LaPierre R R 2017 Three-fold symmetric doping mechanism in GaAs nanowires *Nano Lett.* **17** 5875–82

[21] Krogstrup P, Curiotto S, Johnson E, Aagesen M, Nygård J and Chatain D 2011 Impact of the liquid phase shape on the structure of III–V nanowires *Phys. Rev. Lett.* **106** 1–4

[22] Jacobsson D, Panciera F, Tersoff J, Reuter M C, Lehmann S, Hofmann S, Dick K A and Ross F M 2016 Interface dynamics and crystal phase switching in GaAs nanowires *Nature* **531** 317–22

[23] Zhang Y *et al* 2017 Growth of pure zinc-blende GaAs(P) core–shell nanowires with highly regular morphology *Nano Lett.* **17** 4946–50

[24] Spirkoska D, Abstreiter G and Fontcuberta i Morral A 2008 Size and environment dependence of surface phonon modes of gallium arsenide nanowires as measured by Raman spectroscopy *Nanotechnology* **19** 435704

[25] Venkatesan S, Mancabelli T, Krogstrup P, Hartschuh A, Dehm G and Scheu C 2017 Surface optical phonon propagation in defect modulated nanowires *J. Appl. Phys.* **121** 085702

[26] Steele J A, Puech P and Lewis R A 2016 Polarized Raman backscattering selection rules for (hhl)-oriented diamond- and zincblende-type crystals *J. Appl. Phys.* **120** 055701

[27] Ketterer B, Uccelli E and Fontcuberta i Morral A 2012 Mobility and carrier density in p-type GaAs nanowires measured by transmission Raman spectroscopy *Nanoscale* **4** 1789

[28] Irmer G, Wenzel M and Monecke J 1997 Light scattering by a multicomponent plasma coupled with longitudinal-optical phonons: Raman spectra of p-type GaAs:Zn *Phys. Rev.* B **56** 9524–38

[29] Mlayah A, Carles R, Landa G, Bedel E and Muñoz-Yagüe A 1991 Raman study of longitudinal optical phonon-plasmon coupling and disorder effects in heavily Be-doped GaAs *J. Appl. Phys.* **69** 4064–70

[30] Goktas N I, Fiordaliso E M and LaPierre R R 2018 Doping assessment in GaAs nanowires *Nanotechnology* **29** 234001

[31] Amaduzzi F *et al* 2016 Tuning the response of non-allowed Raman modes in GaAs nanowires *J. Phys. D: Appl. Phys.* **49** 095103

[32] Mlayah A, Carles R, Landa G, Bedel E and Muñoz-Yagüe A 1991 Raman study of longitudinal optical phonon-plasmon coupling and disorder effects in heavily Be-doped GaAs *J. Appl. Phys.* **69** 4064–70

[33] Zekeng S, Prevot B and Schwab C 1988 Raman determination of the Faust–Henry coefficient of GaAs in the 1.9 to 2.7 eV range at ordinary and low temperatures *Phys. Status Solidi* **150** 65–72

[34] Zardo I, Conesa-Boj S, Peiro F, Morante J R, Arbiol J, Uccelli E, Abstreiter G and Fontcuberta i Morral A 2009 Raman spectroscopy of wurtzite and zinc-blende GaAs nanowires: polarization dependence, selection rules, and strain effects *Phys. Rev.* B **80** 245324

[35] Irmer G *et al* 1991 Determination of the hole concentration and mobility of p-GaP by hall and by raman measurements *Semicond. Sci. Technol.* **6** 1072–8

[36] Wenzel M, Irmer G, Monecke J and Siegel W 1997 Hole mobilities and the effective hall factor in p-type GaAs *J. Appl. Phys.* **81** 7810–6

[37] Mohney S E, Wang Y, Cabassi M A, Lew K K, Dey S, Redwing J M and Mayer T S 2005 Measuring the specific contact resistance of contacts to semiconductor nanowires *Solid-State Electron.* **49** 227–32

[38] Park H, Beresford R, Hong S and Xu J 2010 Geometry- and size-dependence of electrical properties of metal contacts on semiconducting nanowires *J. Appl. Phys.* **108** 094308

[39] Gutsche C, Regolin I, Blekker K, Lysov A, Prost W and Tegude F J 2009 Controllable p-type doping of GaAs

nanowires during vapor–liquid–solid growth *J. Appl. Phys.* **105** 024305

[40] Stareev G 1993 Formation of extremely low resistance Ti/Pt/Au ohmic contacts to p-GaAs *Appl. Phys. Lett.* **62** 2801–3

[41] Küpers H, Lewis R B, Tahraoui A, Matalla M, Krüger O, Bastiman F, Riechert H and Geelhaar L 2018 Diameter evolution of selective area grown Ga-assisted GaAs nanowires *Nano Res.* **11** 2885–93

[42] Xu J, Towe E, Yuan Q and Hull R 1999 Beryllium doping and silicon amphotericity in (110) GaAs-based heterostructures: structural and optical properties *J. Cryst. Growth* **196** 26–32

[43] Ivanov S V, Kop'ev P S and Ledentsov N N 1991 Interplay of beryllium segregation and diffusion in heavily doped GaAs and AlGaAs grown by molecular beam epitaxy (thermodynamic analysis) *J. Cryst. Growth* **108** 661–9

[44] Pao Y C, Franklin J and Harris J S 1989 Influence of As4/Ga flux ratio on Be incorporation in heavily doped GaAs grown by molecular beam epitaxy *J. Cryst. Growth* **95** 301–4

Be-dopant gradients in self-catalyzed GaAs nanowires

Supplementary Data

Marcelo Rizzo Piton[1,2], Eero Koivusalo[2], Teemu Hakkarainen[2], Helder V. A. Galeti[3], Ariano D. Rodrigues[1], Soile Talmila[2], Sergio Souto[4], Donald Lupo[5], Yara Galvao Gobato[1,6] and Mircea Guina[2]

[1] *Physics Department, Federal University of São Carlos, São Carlos-SP, Brazil*

[2] *Optoelectronics Research Centre, Physics Unit, Tampere University, Tampere, Finland*

[3] *Electrical Engineering Department, Federal University of São Carlos, São Carlos-SP, Brazil*

[4] *FZEA/ZAB, University of São Paulo, Pirassununga-SP, Brazil*

[5] *Electronics and Communications Engineering, Tampere University, Tampere, Finland*

[6] *High Field Magnetic Laboratory, Radboud University, The Netherlands*

E-mail: marcelo.rizzopiton@tuni.fi

1. Nanowire-droplet contact angle statistics

Figure S1 shows the post growth Ga droplet contact angle statistics analysis of undoped, Be1 and Be2 NWs. The contact angles were measured from SEM images of the lateral view of 50-70 NWs from each sample. All the SEM images were obtained using the same electron acceleration voltage, working distance and magnification. The NWs were oriented in such way that the (110) facets were facing towards the in lens detector of the SEM. The mean values of contact angles and the standard deviations for undoped, Be1, and Be2 NWs are 127.8°±5.3°, 123.5°±4.6° and 126.4°±6.2° respectively.

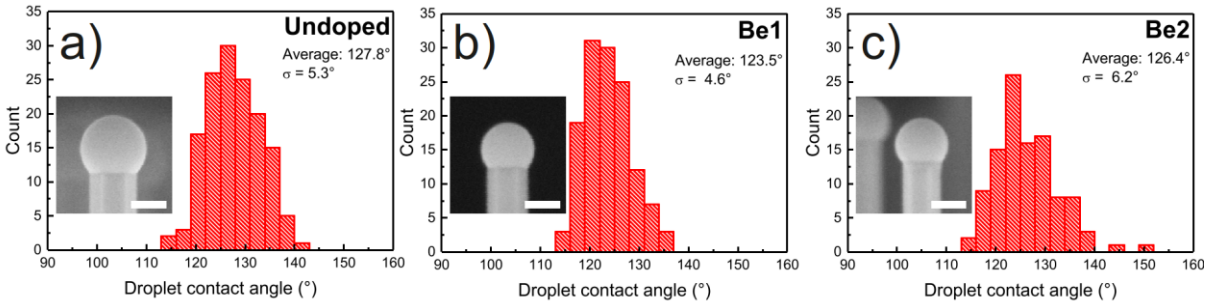

Figure S1: Droplet contact angle statistics of (a) undoped, (b) Be1 and (c) Be2 NWs. The insets show SEM images of representative NWs from each sample and the scale bars correspond to 100 nm.

2. Transmission Electron Microscopy

Figure S2 shows the selected area electron diffraction patterns (SAED) from the same position from of the HR-TEM images of undoped, Be1 and Be2 NWs in figure 1 of the main text. The SAED in figures S2(d), S2(h) and S2(l) show the high disorder of the bottom region of undoped, Be1 and Be2 NW respectively. The SAED of the center and tip regions of Be1 and Be2 NWs further confirm the lower density of twinned ZB GaAs in comparison to the undoped reference NW.

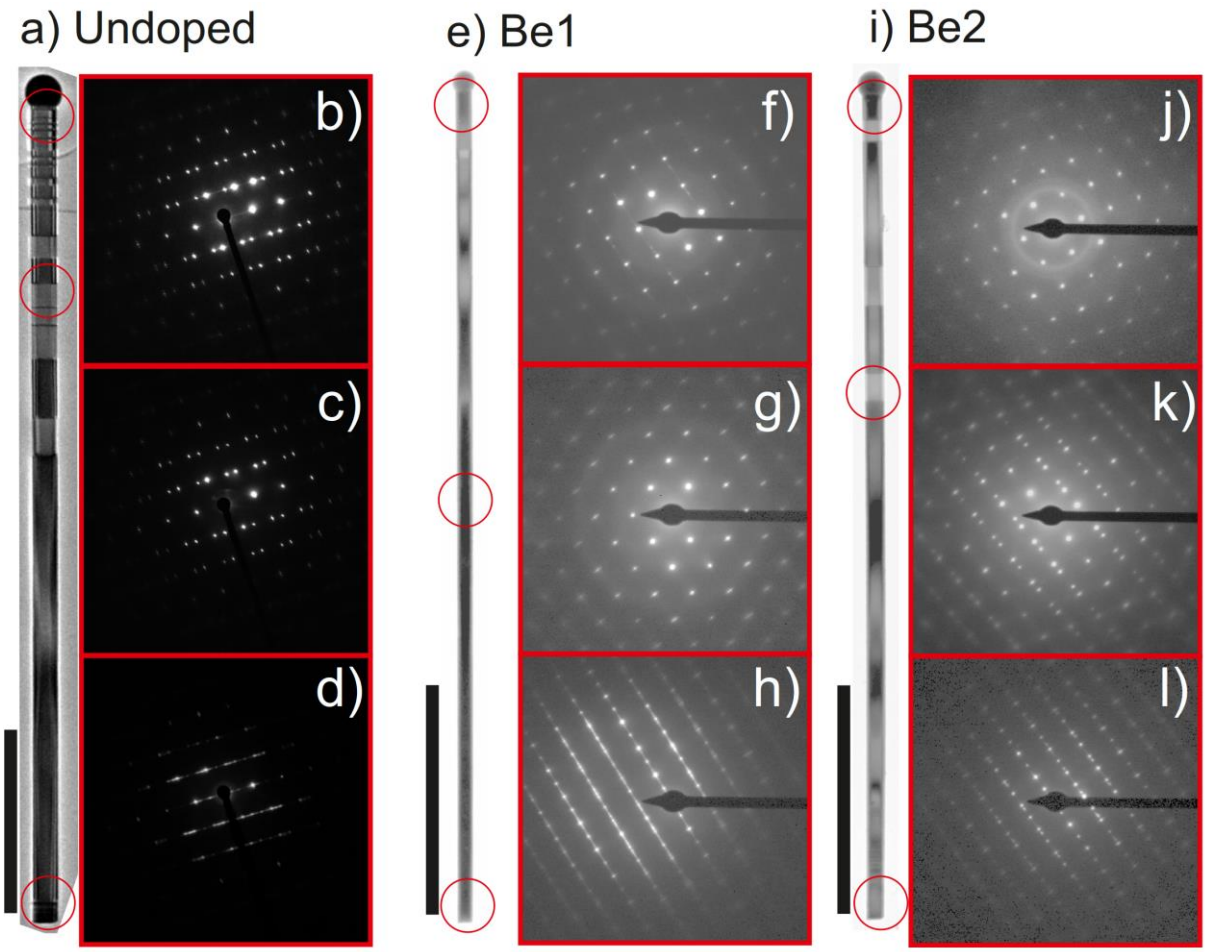

Figure S2: Low magnification HR-TEM images and SAED patterns of (a)-(d) undoped, (e)-(h) Be1 and (i)-(l) Be2 NWs. The red circles in (a), (e) and (i) indicate the position in the NW from where the SAED patterns in (b)-(d), (f)-(h) and (j)-(l) were obtained.

3. Raman spectroscopy

Figure S3 shows additional Raman data of similar Be-doped NWs. The SEM images on the right side of the spectra indicate the axial position of each NW from where the spectra were measured. The plasma frequency and damping constant obtained from the fit of the CPPM peak of each position in figure S3 were used to calculate the carrier concentrations and hole mobilities presented in figures 4(a) and 4(b) respectively.

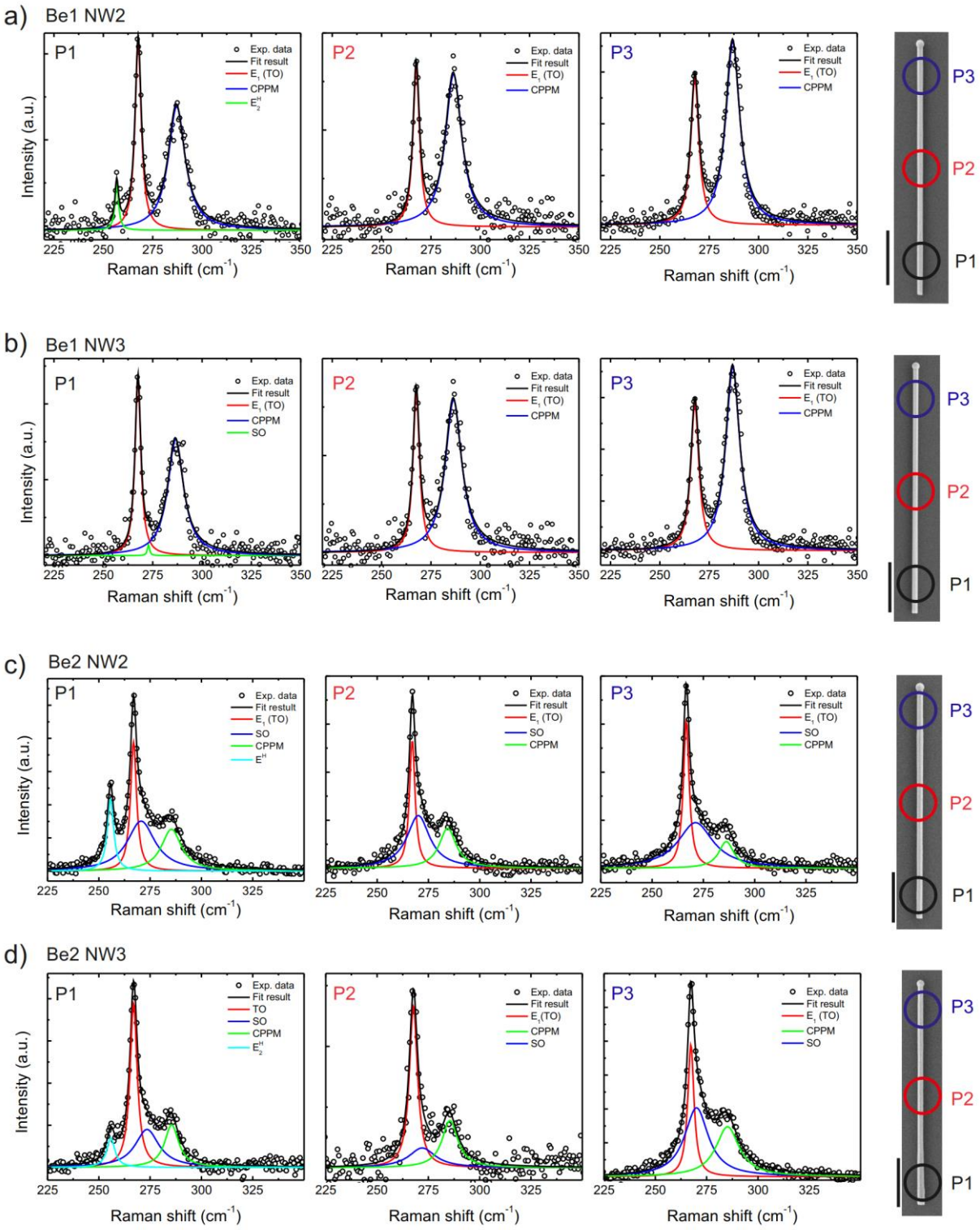

Figure S3: Raman spectra from three different axial positions of Be-doped NWs. (a) Be1 NW2, (b) Be1 NW3, (c) Be2 NW2 and (d) Be2 NW3. The spectra P1, P2, and P3 were collected from the regions indicated in the SEM pictures of the right sides of (a)-(d). The scale bars in the SEM pictures are 1 μm.

4. Transport properties

Figures S4 and S5 show additional IV and SEM data from devices with four evenly spaced contacts for NW samples Be1 and Be2, respectively. The IVs from Be1 NW2 and NW3 in figures S4(a) and S4(e) exhibit similar trend to the data presented in figure 5: asymmetric IV and different current values in different positions along the NWs. This behavior is associated to an increase in the values of the Schottky barrier heights in the metal-semiconductor contacts from bottom (AB channels) to tip (CD channels) of the NWs. Figures S5(a) and S5(e) show IV for Be2 NW2 and NW3 respectively. For these devices, the resistivity of the AB, BC, and CD channels were obtained from equation (5) and presented in figure 8.

As was discussed in Section 3.3, the Ga droplets were removed from some of the NWs during the contact fabrication process. The bottom and tip ends of the NWs in the devices shown in figures S4(b), S4(f), S5(b) and S5(f) were identified by the off-cut shape formed at the bottom end of the NWs, which was a consistent characteristic of the undoped and Be-doped NWs. This characteristic feature was observed in the TEM micrographs as well as in the SEM images of NWs used for Raman spectroscopy. Higher magnification SEM of the bottom region of the NWs are shown in figures S4(c), S4(g), S5(c), S5(g) and the tip region in figures S4(d), S4(h), S5(d) and S5(h). This trend in the NWs allowed us to identify with confidence the bottom and tip ends of the NWs, thus corroborating the results indicating different Be-dopant incorporation mechanisms discussed in the main text.

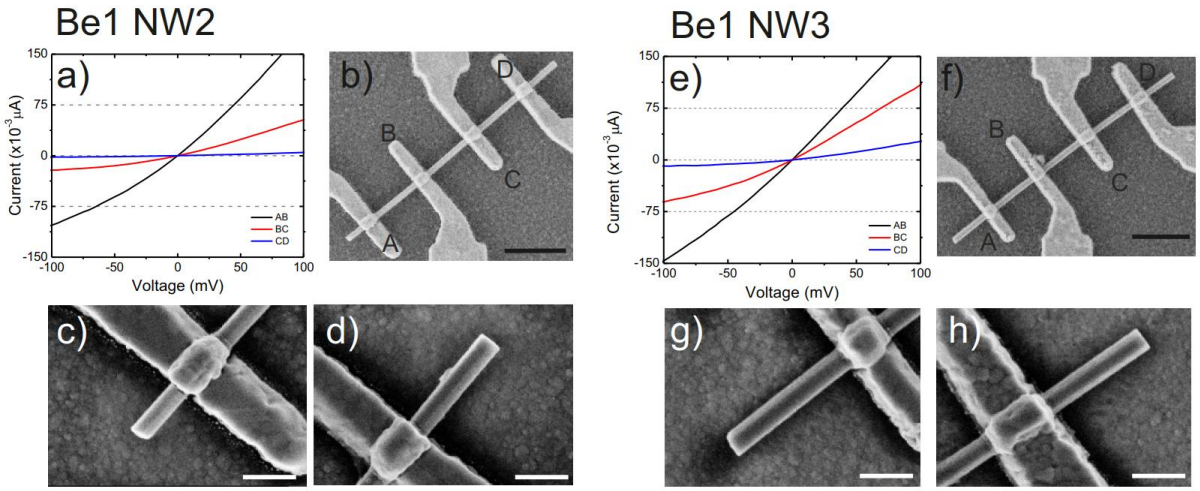

Figure S4: IV from Be1 NW2 (a) and NW3 (e) and the corresponding SEM images from the measured devices in (b) and (f). The A contact is close to the bottom and D contact close to the tip of the NW. The higher magnification SEM images of the NW ends were used to identify the bottom region of the NWs in (c),(g) and the tip region in (d) and (h). The scale bars are 1 µm in (b) and (f) and 250 nm in (c), (d), (g) and (h).

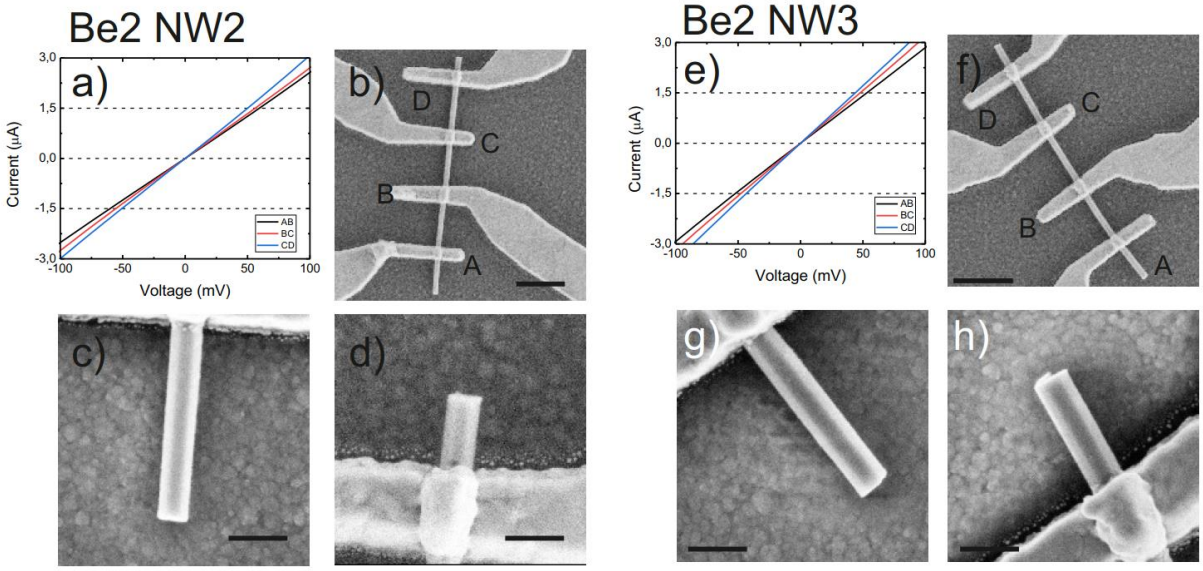

Figure S5: IV from Be2 NW2 (a) and NW3 (e) and the corresponding SEM images from the measured devices in (b) and (f). The A contact is close to the bottom and D contact close to the tip of the NW. The higher magnification SEM images of the NW ends were used to identify the bottom region of the NWs in (c),(g) and the tip region in (d) and (h). The scale bars are 1 µm in (b) and (f) and 250 nm in (c), (d), (g) and (h).

Since the off-cut at the bottom end of Be2 NW2 in figure S5(c) is not as evident as for the other NWs presented in figures S4 and S5, we show additional SEM images of Be2 NW2 from different perspectives in order to further confirm the bottom and top ends of the NW. Figures S6(a)-(d) show 30° tilted SEM pictures from a perspective perpendicular to the NW axis, obtained by properly aligning the NW in respect to the SEM detector and tilting the sample holder. From this perspective, we are able to identify the off-cut in figures S6(a) and (b) from the A contact in figure S5(b), which was ascribed to the bottom end of the NW. In contrast, figures S6(c) and (d) from D contact exhibit a flat surface at the end of the NW with residues of the Ga droplet, similar to observed in figure S5(h) from Be2 NW3, giving further confirmation that it was correctly ascribed to the top end of the NW. Figures S6(e)-(g) show additional SEM images of the bottom end (A contact), obtained by aligning the NW in a 45° in relation to the SEM detector and tilting the sample holder by 30°. The evidenced off-cut in figure S6(g) gives the necessary confirmation that the contact A indeed corresponds to the bottom end of the NW.

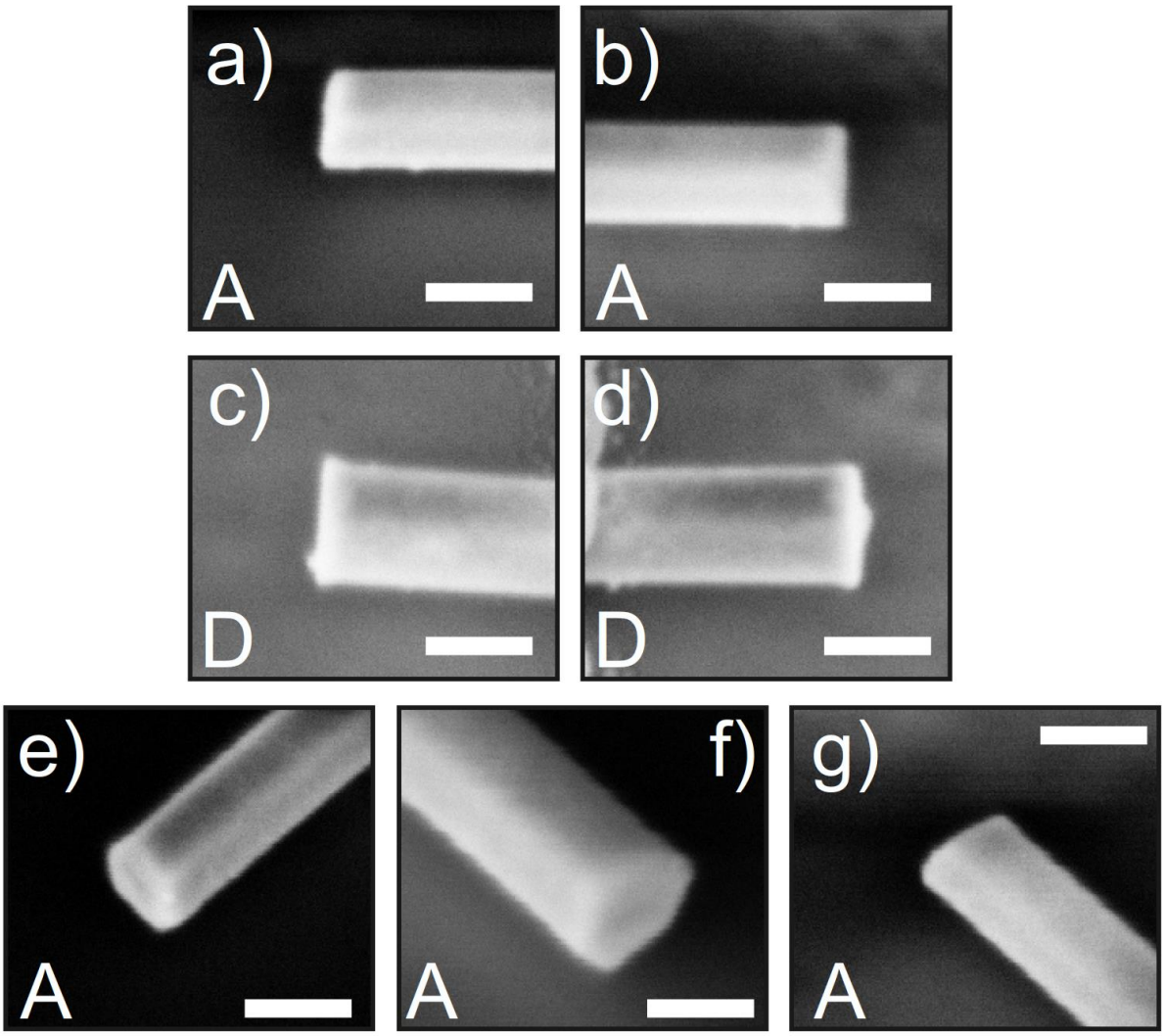

Figure S6: High magnification SEM images of NW end morphologies close to the A and D contacts of Be2 NW2 in figure S4 (a)-(d). The images were obtained from different perspectives by properly aligning the NW axis in respect to the SEM detector and tilting the sample holder by 30°. A perspective perpendicular to the NW axis is shown for the bottom region (A contact) in (a) and (b) and for the tip region (D contact) in (c) and (d). Additional perspectives on the A contact obtained by aligning the NW in a 45° angle in relation to the SEM detector and tilting the sample holder stage by 30° are shown in (e)-(g). The scale bars correspond to 100 nm.

PUBLICATION III

Optimization of Ohmic contacts to p-GaAs nanowires

Marcelo Rizzo Piton, Teemu Hakkarainen, Joonas Hilska, Eero Koivusalo, Donald Lupo, Helder V. A. Galeti, Yara G. Gobato and Mircea Guina

Nanoscale Research Letters **14**, 344 (2019)
DOI: 10.1186/s116710.1186/s11671-019-3175-81-019-3175-8

Nanoscale Research Letters

NANO EXPRESS Open Access

Optimization of Ohmic Contacts to p-GaAs Nanowires

Marcelo Rizzo Piton[1,2*], Teemu Hakkarainen[1], Joonas Hilska[1], Eero Koivusalo[1], Donald Lupo[3], Helder Vinicius Avanço Galeti[4], Yara Galvão Gobato[2] and Mircea Guina[1]

Abstract

The performance of Ohmic contacts applied to semiconductor nanowires (NWs) is an important aspect for enabling their use in electronic or optoelectronic devices. Due to the small dimensions and specific surface orientation of NWs, the standard processing technology widely developed for planar heterostructures cannot be directly applied. Here, we report on the fabrication and optimization of Pt/Ti/Pt/Au Ohmic contacts for p-type GaAs nanowires grown by molecular beam epitaxy. The devices were characterized by current–voltage (IV) measurements. The linearity of the IV characteristics curves of individual nanowires was optimized by adjusting the layout of the contact metal layers, the surface treatment prior to metal evaporation, and post-processing thermal annealing. Our results reveal that the contact resistance is remarkably decreased when a Pt layer is deposited on the GaAs nanowire prior to the traditional Ti/Pt/Au multilayer layout used for p-type planar GaAs. These findings are explained by an improved quality of the metal-GaAs interface, which was evidenced by grazing incidence X-ray diffraction measurements in similar metallic thin films deposited on GaAs (110) substrates. In particular, we show that Ti exhibits low degree of crystallinity when deposited on GaAs (110) surface which directly affects the contact resistance of the NW devices. The deposition of a thin Pt layer on the NWs prior to Ti/Pt/Au results in a 95% decrease in the total electrical resistance of Be-doped GaAs NWs which is associated to the higher degree of crystallinity of Pt than Ti when deposited directly on GaAs (110).

Keywords: Nanowires, GaAs, p-type doping, Ohmic contacts

Introduction

An important step in the fabrication of semiconductor electronic and optoelectronic devices is to obtain high-quality and reliable Ohmic contacts at the metal-semiconductor interface. To this end, GaAs is an important and widely used material in technological applications such as laser devices, solar cells, and photodetectors. Therefore, the fabrication of Ohmic contact to p-type- and n-type-doped GaAs layers has been the target of a large number of investigations [1]. Generally speaking, the fabrication of Ohmic contacts to semiconductor materials include four steps: (1) removal of the surface native oxide, (2) passivation of the surface states at the semiconductor-metal interface, (3) deposition of metallic layers acting as the electrical contacts, and (4) thermal annealing [2, 3]. Starting from the selection of metals that provide low contact resistance and excellent thermal stability, Au-based alloys have been widely exploited, specifically for p-type GaAs in the form of Au/Zn/Au [1, 3, 4] and Ti/Pt/Au [1, 5] layers. On the other hand, semiconductor III–V nanowires (NWs) have emerged as newer class of promising nanoscale materials for application as LEDs [6, 7], solar cells [8, 9], and photodetectors [10], and these have triggered specific developments on device processing.

Majority of the technology reported in the literature for Ohmic contact fabrication was developed for GaAs (100) thin films and bulk structures, while the self-catalyzed growth of GaAs NWs yields (110) surface orientation at the sidewalls [11–15]. Different surface orientations exhibit different electronic states [16] which affect the interface properties and Schottky barrier heights [17–19]. In addition, the surface orientation may

* Correspondence: marcelo.rizzopiton@tuni.fi
[1]Optoelectronics Research Centre, Physics Unit, Tampere University, Tampere, Finland
[2]Physics Department, Federal University of São Carlos, São Carlos, Sao Paulo, Brazil
Full list of author information is available at the end of the article

affect the crystallization dynamics of the deposited metal films. Good Ohmic contacts to p-GaAs NWs were previously reported [20–28] by using a variation of chemical treatments to remove the native oxide, surface passivation, and different metallic multilayers deposited on the NWs. Then, the use of Pt/Ti/Pt/Au electrical contacts to p-type GaAs thin films was reported to yield low Ohmic contact resistivity even for moderate dopant concentrations due to the low Schottky barrier height of Pt/GaAs [29]. In addition, Pt was found to be thermally stable with small reaction rates to GaAs for heat treatments with temperatures ranging from 300 to 500 °C [29–31]. Pt/Ti/Pt/Au metallic multilayer is the most frequently reported [20, 23, 25, 26, 28] Ohmic contact to p-GaAs NWs. However, a more comprehensive understanding of metal properties on Ohmic contact formation is the key to further improve the electrical contact quality on nanoscale devices. Due to the wide range of NW growth techniques and dopant concentrations in p-GaAs NWs recently reported, it would be unviable to make a comparison of the contact resistances, when they are available. Instead, a comprehensive investigation of different contact manufacturing routes on the same set of NW samples would be more suitable to exclude the effect of NW properties.

Here, we address the effects of different Pt- and Ti-based electrical contacts and surface treatments prior to metal evaporation on the overall current–voltage (IV) characteristics of self-catalyzed Be-doped GaAs NWs grown on Si substrates [11, 32]. We analyze the changes in the total resistance of the NW channels based on structural investigation by X-ray diffraction of Ti, Pt, and Pt/Ti thin films deposited on GaAs (110) substrates. We show that a high contact resistance is associated with a low degree of crystallinity of Ti when deposited directly on GaAs (110), while Pt/Ti/Pt/Au electrical contacts results in a remarkable decrease of the contact resistance, which is attributed to the improvement of the metal layer quality observed in the first Pt/Ti layers deposited on GaAs (110) surface.

Materials and Methods

Nanowire Growth

The self-catalyzed Be-doped GaAs NWs were grown by solid-source molecular beam epitaxy (MBE) on lithography-free oxide patterns fabricated on p-Si (111) substrates by droplet epitaxy and spontaneous oxidation [32]. The NW growth temperature was 640 °C, as determined by pyrometer, and a Ga flux corresponding to planar 0.3 μm/h growth rate on GaAs (100) was used. A 60 s Ga wetting preceded the NW growth, which was initiated by providing As_2 with V/III beam equivalent pressure ratio of 9 and Be flux corresponding to $2.0 \times 10^{19}\,cm^{-3}$ p-type doping concentration; this was determined from the growth of planar Be-doped GaAs (100) calibration samples by room temperature Hall measurements. The growth duration was 60 min. More details of the growth methodology and the structural properties of the undoped and Be-doped NWs can be found in Refs. [11, 32, 33]. In short, the NWs are composed of pure zinc blende GaAs with the formation of a few twin planes [33]. The NWs have hexagonal shape with sidewalls composed exclusively from (110) oriented facets, as it was previously determined from structural analysis of the Be-doped NWs [33] and further confirmed in undoped GaAs NWs grown under similar conditions [12].

Contacts Fabrication and Characterization

The NWs were mechanically transferred to a p-GaAs (100) substrate covered with a 200-nm-thick SiO_2 layer, which was pre-patterned by photolithography and electron beam evaporation of Ti/Au pads for transport characterization. The position of the transferred wires on the substrate was identified by low magnification scanning electron microscopy (SEM) imaging. Positive electron beam resist was spin-coated on the substrate and exposed with electron beam on the electrical contact areas. The resist was developed in MIBK:IPA solution after electron beam exposure and possibly followed by an oxygen plasma treatment to remove the residual resist of the NW sidewalls, as described in Table 1. The effects of the oxygen plasma treatment on the device performance will be later discussed in the text. Prior to metal evaporation of the contact layers, the samples were chemically treated to remove the native oxide and passivate the exposed NW sidewalls, as described later in the text. The lift-off was done by dipping the sample in heated acetone, rinsing in IPA and blow drying with nitrogen.

We have developed five distinct processes combining different surface treatments of the exposed NW sidewalls with different metallic multilayers used as electrical contacts. This allowed us to determine the individual contributions of each parameter in the resulting contact resistance when applied to the p-type GaAs NWs. For the surface native oxide removal, we used either a 2.8% NH_4OH or 3.7% HCl diluted in H_2O followed by H_2O rinsing. For the surface passivation, we used a 15% solution of $(NH_4)_2S_x$ diluted in H_2O (heated at 45 °C) followed by H_2O rinsing. The metallic multilayer were deposited using e-beam evaporation and were either Ti/Pt/Au (20/20/200 nm) or Pt/Ti/Pt/Au (5/10/10/200 nm). A rapid thermal annealing (RTA) of 400 °C for 30 s was used for the Pt/Ti/Pt/Au multilayer. The processes used for each sample are specified in Table 1. For each sample, 4 evenly spaced electrical contacts were fabricated along the NW axis. In this work, we restrict the IV analysis to the contact pairs located in the center region of the NW. The IV data was obtained at room temperature using a Keysight probe station.

Table 1 Fabrication details of electrical contacts used for transport characterization of Be-doped GaAs NWs

Process#	Oxygen plasma	Oxide removal	Surface passivation	Metal layers	RTA
P1	–	$NH_4OH:H_2O$	–	Ti/Pt/Au	–
P2	Yes	$HCl:H_2O$	$(NH_4)_2S_x$	Ti/Pt/Au	–
P3	–	$HCl:H_2O$	$(NH_4)_2S_x$	Ti/Pt/Au	–
P4	–	$HCl:H_2O$	$(NH_4)_2S_x$	Pt/Ti/Pt/Au	–
P5	–	$HCl:H_2O$	$(NH_4)_2S_x$	Pt/Ti/Pt/Au	400 °C, 30 s

Structural Investigation by Grazing Incidence X-ray Diffraction

In order to investigate the structural properties of the electrical contacts on the NWs, grazing incidence X-ray diffraction (GIXRD) patterns were measured from reference Ti, Pt, and Pt/Ti thin films evaporated on undoped GaAs (110) substrates. We prepared the thin film samples described in Table 2 using native oxide removal by HCl: H_2O and surface passivation by $(NH_4)_2S_x$ in the same way as for the NW devices. The small incidence angle of the X-rays used in GIXRD allows us to analyze metallic films with the same thickness as used in the NW contacts owing to the small penetration depth. The GIXRD patterns were measured using Cu Kα radiation with 1.54 Å wavelength and an incidence angle of $\omega = 0.75°$ in relation to the sample surface. The diffraction peak positions are indexed according to ICDD files #00-044-1294 and #00-004-0802 for hexagonal-close packed (HCP) Ti and face-centered cubic (FCC) Pt, respectively, and are corrected by accounting for the effect of refraction of the X-rays in GIXRD experiments as described in Ref. [34].

Results and Discussion

Figure 1a shows the IV characteristics for samples P1 to P5, and Fig. 1b an SEM image of a Be-doped GaAs NW with electrical contacts used for transport characterization. The almost symmetric, nonlinear shape of the IVs for P1 to P4 in Fig. 1a indicates that the contacts are of Schottky type with similar barrier heights for each contact [35]. The nonlinearity of the IV for sample P1 evidently shows that the standard p-GaAs process as in P1 does not yield Ohmic contacts as is the case for GaAs planar thin films. Usually, in doped GaAs NWs, HCl oxide removal is used, possibly followed by $(NH_4)_2S_x$ surface passivation prior to metal evaporation for Ohmic contact formation [20, 21, 36, 37] instead of NH_4OH. In addition, oxygen plasma treatment of the exposed NW surface has been previously used to remove the residual resist from the NW sidewalls [36, 38]. However, as a side effect, this process can induce surface defects in GaAs such as As vacancies, resulting in donor-like traps that are responsible for carrier compensation and therefore increasing the depletion layer width [5].

Table 2 Description of surface chemical treatments and metal layers deposited on GaAs (110) substrates for GIXRD analysis

Sample#	Oxide removal	Surface passivation	Metal layers
S1	$HCl:H_2O$	–	Ti (20 nm)
S2	$HCl:H_2O$	$(NH_4)_2S_x$	Ti (20 nm)
S3	$HCl:H_2O$	$(NH_4)_2S_x$	Pt (5 nm)
S4	$HCl:H_2O$	$(NH_4)_2S_x$	Pt/Ti (5/20 nm)

To evaluate the effect of the oxygen plasma treatment on the contact resistance of p-GaAs NWs, we compare the IV of a sample with (P2) and without (P3) oxygen plasma cleaning prior to the surface treatment by HCl and $(NH_4)_2S_x$ in Fig. 1a. P2 yields the worst IV performance (defined as the electrical current value for the same applied voltage) in all samples but sample P3 by its turn exhibits better IV performance than the standard p-GaAs process P1, and the oxygen plasma cleaned P2. This implies two significant results: (i) the effect of the oxygen plasma treatment is detrimental on the contact resistance, and (ii) the P3 with HCl oxide removal combined with $(NH_4)_2S_x$ surface passivation adds up to a lower Schottky barrier height of the metal-semiconductor interface compared to P1.

The IV performance and Ohmic character (evaluated qualitatively by the IV linearity) was strongly enhanced in P4 when compared to P3 by adding a 5-nm Pt layer under the Ti/Pt/Au multilayer, as can be seen from Fig. 1a. The contact resistance is further decreased in P5 after RTA 30 s at 400 °C, achieving a linear IV behavior and improved IV performance when compared to P4.

In order to quantify the effect of the processing parameters on the contact resistance of samples P1–P5 (chemical treatments, metallic multilayer), we show in Fig. 2a the IVs from P1–P5 using a smaller bias range; in this case, the IVs exhibit linear behavior and are mainly governed by the contact resistance [35]. The total resistance from the channel (contacts + NW) in the 100 mV range from Fig. 2a was calculated from a linear fit of the IV characteristics curve, and the results are shown in Fig. 2b. Since the diameters of all investigated NWs are similar, and there is only small wire-to-wire variation in the dopant concentration, as we have previously reported [33], any changes of the total resistance were ascribed to the contact resistance. The higher resistance in P2 compared to P1 and P3 confirms the detrimental effect of oxygen plasma treatment from the qualitative

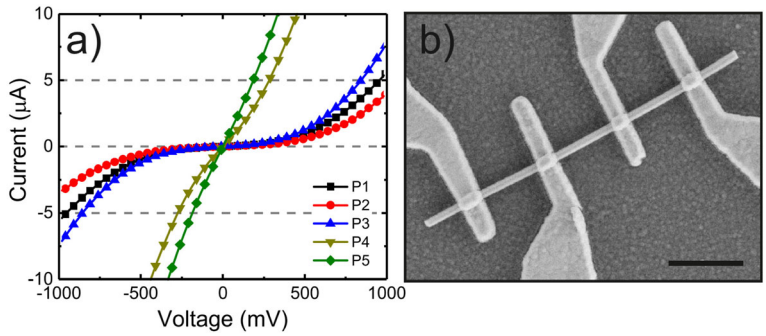

Fig. 1 **a** IV from Be-doped GaAs NWs with electrical contacts fabricated using the processes P1–P5 as described in Table 1. **b** SEM image of a representative Be-doped GaAs NW with four evenly spaced electrical contacts. The scale bar is 1 μm

analysis of the IVs in Fig. 1a. A remarkable result is the decrease in the total resistance from 1400 kΩ in P3 to 72 kΩ in P4 and a further decrease to 40 kΩ after RTA in P5, achieved by depositing an additional Pt layer prior to the Ti/Pt/Au multilayer used in samples P1–P3.

A more comprehensive understanding of the metal-semiconductor interface microstructure after the contact manufacturing is required to establish a correlation of the changes in the contact resistance observed in samples P1–P5. The use of Ti and Pt in Ohmic contact fabrication to GaAs has been previously reported [39, 40], and the structural properties of thin Ti and Pt films evaporated to GaAs (100) surface [41] and amorphous glass substrates [42, 43] have also been analyzed. However, no such detailed studies were found for GaAs (110) surface. The different surface orientation is expected to influence the crystallization dynamics of the Ti and Pt thin films. In addition, the surface chemical passivation by $(NH_4)_2S_x$ could further influence the resulting thin films. The degree of crystallization of Pt (5 nm), Ti (20 nm), and Pt/Ti (5/20 nm) thin films deposited on undoped GaAs (110) substrate was investigated by GIXRD in order to obtain information of the structural properties of the first metallic layers in contact to the NWs in P1–P5. Prior to the metal evaporation, the GaAs (110) substrates went through the native oxide removal by HCl:H_2O and the $(NH_4)_2S_x$ surface passivation steps as the NW samples P3–P5. The details of the surface treatments and metallic thin films evaporated on GaAs (110) substrate are summarized in Table 2.

The GIXRD patterns from samples S1–S4 are shown in the 30 to 60° diffraction angle range in Fig. 3a and in the 60 to 90° range in Fig. 3b. The diffraction patterns in Fig. 3 are vertically shifted and separated in two diffraction angle ranges to provide a better scaling for visualization. First, we focus on the effect of $(NH_4)_2S_x$ surface passivation on the degree of crystallinity of Ti films evaporated on GaAs (110) substrate by comparing samples S1 and S2. In Fig. 3a, we observe overlapping low intensity Ti (002) and Ti (101) peaks centered at 38.4 and 40.2°, respectively, for both S1 and S2. Furthermore, a significantly broader Ti (102) peak centered at 53.0 ° is also observed for both samples, which suggests an amorphous character. The Ti (103) peak centered at 70.6° in Fig. 3b is only observed for S1, which is the only significant disparity between the samples. In general, the low intensities and broad peaks of S1 and S2 indicate a poor crystallinity of the Ti films when deposited on GaAs (110) surface after HCl oxide removal and regardless of the use of $(NH_4)_2S_x$ passivation. In case of S3, for which Pt was deposited on GaAs (110) substrate with the same surface treatment as in S2, we observe much

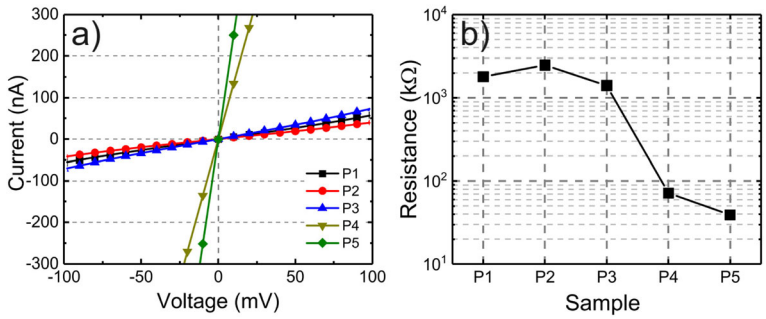

Fig. 2 **a** IV from P1 to P5 in the 100 mV applied voltage range. **b** Total channel resistance of the P1–P5 obtained from linear fit of the IVs in **a**

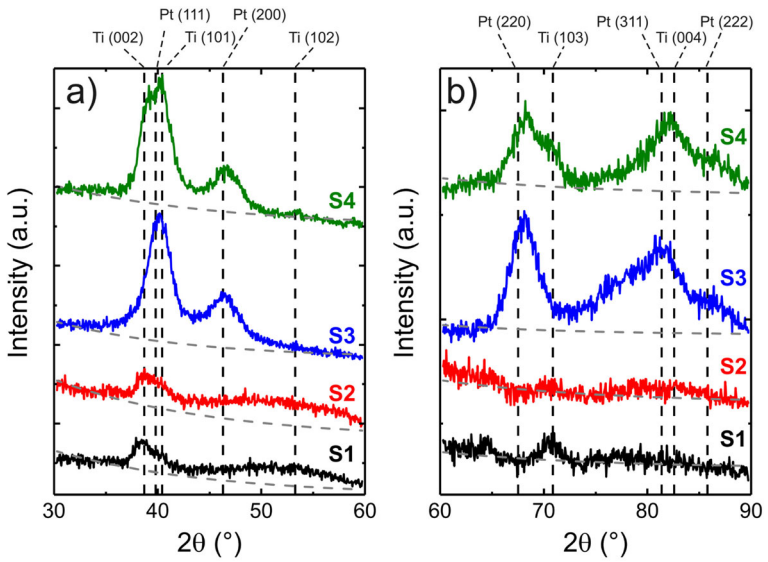

Fig. 3 GIXRD patterns from samples S1–S4 of the **a** 30 to 60° diffraction angle range and (**b**) 60 to 90° range. The dashed gray lines represent exponential decay baselines that originate from diffuse X-ray scattering. The vertical dashed black lines correspond to the different diffraction planes of Ti and Pt, labeled at the top of **a** and **b**

more pronounced Pt (111), Pt (200), Pt (220), Pt (311), and Pt (222) diffraction peaks centered at 39.8°, 46.3°, 67.5°, 81.3°, and 85.7°, respectively. This indicates that the Pt film in S3 exhibits a higher degree of crystallinity in comparison to the Ti samples. The same applies to S4 which shows similar Pt diffraction signatures as S3 in Fig. 3a, b. The broad and asymmetric peaks between 35°–45°, 65°–75°, and 75°–90° for S4 are formed due to the overlapping of Ti (002)-Ti (101)-Pt (111), Ti (103)-Pt (220), and Ti (004)-Pt (311)-Pt (222) diffraction peaks, respectively. A qualitative comparison of the GIXRD patterns from S2, S3, and S4 implies that the degree of crystallinity of Ti in S4 is at least on the same level as in S1. The Ti (103) peak at 70.6° is observed as a clear shoulder on the Pt (220) peak in Fig. 3b and the Ti (102) peak at 53.0° in Fig. 3a is present with low intensity but narrow linewidth in S4 while exhibiting a very broad, amorphous-like, peak in S1 and S2. This result suggests an improved degree of crystallinity of Ti when deposited on Pt instead of the GaAs (110) surface, which will in the following be directly correlated to the electrical contacts properties described in Figs. 1 and 2.

The GIXRD analysis of the metallic layers in S1–S4 allows us to correlate the degree of crystallinity of Ti and Pt deposited on GaAs (110) substrate and the total resistance results from P1–P5 in Fig. 2b. It is important to stress that in this work, we base our correlations of the changes in the total resistance of P1–P5 primarily on the GIXRD data obtained from S1–S4. We assume that other factors, such as the metal-NW interface quality due to the hexagonal geometry of the NWs sidewalls, have negligible contributions in the total resistance changes observed in P1–P5. The $(NH_4)_2S_x$ surface passivation has a beneficial effect on the properties of the GaAs-metal interface as seem by comparing the IV and total resistance of samples P1 and P3, but with a low degree of crystallinity of the Ti film when deposited directly on GaAs (110) surface, as observed in S1 and S2. This could be the result of a reaction of sulfur with the overgrown Ti. In addition, it has been reported that Ti is highly reactive with the remaining impurities in the evaporation chamber during metal deposition [41], forming additional layers between the metal/GaAs and therefore increasing the contact resistance [5]. As previously discussed, the increase in contact resistance in P2 was ascribed to the possible surface damages caused by the oxygen plasma cleaning. The addition of a thin Pt layer between the Ti and GaAs (110) surface as in S4 results in a higher degree of crystallinity of the Ti film when compared to S1 and S2. This result can be correlated to the decrease of the total channel resistance from 1400 kΩ in P3 to 72 kΩ in P4 which is associated to a decrease of the contact resistance. The RTA further decreases the total channel resistance to 40 kΩ in P5 in addition to the increase of the Ohmic character of the IV shown in Fig. 2a. This result indicates that no detrimental reactions occur between Pt and GaAs surface in the annealing temperature and time used [29–31].

Conclusions

The influence of surface chemical treatment prior to metal evaporation and the formation of Ohmic contacts to Be-doped self-catalyzed GaAs NWs was investigated

by correlating transport characterization of single NWs and structural analysis of Ti, Pt, and Pt/Ti thin films deposited on GaAs substrates.We show that Ti exhibits low degree of crystallinity when deposited on GaAs (110) surface which directly affects the contact resistance of the NW devices. The deposition of a thin Pt layer on the NWs prior to Ti/Pt/Au results in a 95% decrease in the total electrical resistance of Be-doped GaAs NWs which is associated to the higher degree of crystallinity of Pt than Ti when deposited directly on GaAs (110). In addition, we show that thermal annealing of the metallic layers further decreases the contact resistance. These findings are of technological importance when designing Ohmic contacts to GaAs NWs-based devices and show the individual contributions of each processing step, described in Table 1, in the total resistance and Ohmic character of the NW devices. To further improve the device performance, a systematic optimization of the parameters of each individual step would be required. In particular, we show that the metal-semiconductor interface at the NW sidewalls plays a major role in the device performance and opens the way to further investigations of the crystallization process of metallic thin films deposited on different surface orientations of III–V semiconductor materials.

Abbreviations

FCC: Face-centered cubic; GIXRD: Grazing incidence X-ray diffraction; HCP: Hexagonal-closed packed; IV: Current–voltage; NW: Nanowire; RTA: Rapid thermal annealing; SEM: Scanning electron microscopy

Acknowledgements

M.R.P. acknowledges CAPES/CNPq process 88887.100549/2015-00, and H. V. A.G. and Y.G.G. acknowledge FAPESP grants 18/01808-5, 16/10668-7, and 14/50513-7. M.R.P., E.K., T.H., and M.G. acknowledge financial support from the Academy of Finland Project NESP (#294630), and NanoLight (#310985) and the Vilho, Yrjö, and Kalle Väisälä Foundation of the Finnish Academy of Science and Letters. The work is part of the Academy of Finland Flagship Programme PREIN (#320168").

Authors' Contributions

MRP was responsible for manufacturing the electrical contacts on the NWs, preparation of the metallic thin films deposited on GaAs (110) substrate, SEM imaging, and organizing the manuscript. TH and EK were responsible for MBE growth of NWs. JH was responsible for GIXRD experiments. TH supervised the electrical contact fabrication processes. DL provided the infrastructure for transport characterization. MG, YGG, and HVAG initiated the research and were responsible for supervising the work. All authors read and approved the final manuscript.

Funding

This work was funded by CAPES/CNPq process 88887.100549/2015-00, FAPESP grants 18/018085, 16/10668-7, and 14/50513-7, Academy of Finland Project NESP (decision number 294630), and NanoLight (decision number 310985), and the Vilho, Yrjö and Kalle Väisälä Foundation of the Finnish Academy of Science and Letters.

Availability of Data and Materials

The datasets supporting the conclusions of this study are included in within the article.

Competing Interests

The authors declare that they have no competing interests.

Author details

[1]Optoelectronics Research Centre, Physics Unit, Tampere University, Tampere, Finland. [2]Physics Department, Federal University of São Carlos, São Carlos, Sao Paulo, Brazil. [3]Electronics and Communications Engineering, Tampere University, Tampere, Finland. [4]Electrical Engineering Department, Federal University of São Carlos, São Carlos, Sao Paulo, Brazil.

Received: 19 June 2019 Accepted: 4 October 2019
Published online: 14 November 2019

References

1. Baca A, Ren F, Zolper J et al (1997) A survey of ohmic contacts to III-V compound semiconductors. Thin Solid Films 308:599–606
2. Piotrowska A (1993) Ohmic contacts to GaAs: fundamentals and practice. Acta Phys Pol A 84:491–504
3. Cox RH, Strack H (2002) Ohmic contacts for GaAs devices. Solid State Electron 10:1213–1218
4. Lu Y (1989) Rapid thermal alloyed Ohmic contacts to p-type GaAs. J Electrochem Soc 136:3123
5. Stareev G (1993) Formation of extremely low resistance Ti/Pt/Au ohmic contacts to p-GaAs. Appl Phys Lett 62:2801–2803
6. Dimakis E, Jahn U, Ramsteiner M et al (2014) Coaxial multishell (In,Ga)As/GaAs anowires for near-infrared emission on Si substrates. Nano Lett 14:2604–2609
7. Svensson CPT, Mårtensson T, Trägårdh J et al (2008) Monolithic GaAs/InGaP nanowire light emitting diodes on silicon. Nanotechnology 19:305201
8. Aberg I, Vescovi G, Asoli D et al (2016) A GaAs nanowire array solar cell with 15.3% efficiency at 1 sun. IEEE J Photovoltaics 6:185–190
9. van Dam D, van Hoof NJJ, Cui Y et al (2016) High-efficiency nanowire solar cells with Omnidirectionally enhanced absorption due to self-aligned indium–tin–oxide Mie Scatterers. ACS Nano 10:11414–11419
10. LaPierre RR, Robson M, Azizur-Rahman KM, Kuyanov P (2017) A review of III–V nanowire infrared photodetectors and sensors. J Phys D Appl Phys 50:123001
11. Koivusalo E, Hakkarainen T, Guina M (2017) Structural investigation of uniform ensembles of self-catalyzed GaAs nanowires fabricated by a lithography-free technique. Nanoscale Res Lett 12:192
12. Koivusalo ES, Hakkarainen TV, Galeti HVA et al (2019) Deterministic switching of the growth direction of self-catalyzed GaAs nanowires. Nano Lett 19:82–89
13. Hilse M, Ramsteiner M, Breuer S et al (2010) Incorporation of the dopants Si and be into GaAs nanowires. Appl Phys Lett 96:193104
14. Zhang Y, Sun Z, Sanchez AM et al (2018) Doping of self-catalyzed nanowires under the influence of droplets. Nano Lett 18:81–87
15. Dastjerdi MHT, Fiordaliso EM, Leshchenko ED et al (2017) Three-fold symmetric doping mechanism in GaAs nanowires. Nano Lett 17:5875–5882
16. Joannopoulos JD, Cohen ML (1974) Intrinsic surface states of (110) surfaces of group IV and III-V semiconductors. Phys Rev B 10:5075–5081
17. Dinan JH, Galbraith LK, Fischer TE, Haven N (1971) Electronic properties of clean cleaved {110} GaAs surfaces. Surf Sci 26:587–604
18. Allen LTP, Weber ER, Washburn J, Pao YC (1987) Device quality growth and characterization of (110) GaAs grown by molecular beam epitaxy. Appl Phys Lett 51:670–672
19. Newman N, Van Schilfgaarde M, Kendelwicz T et al (1986) Electrical study of Schottky barriers on atomically clean GaAs (110) surfaces. Phys Rev B 33:1146–1159
20. Dheeraj DL, Munshi AM, Christoffersen OM et al (2013) Comparison of Be-doped GaAs nanowires grown by Au- and Ga-assisted molecular beam epitaxy. J Cryst Growth 378:532–536
21. Cifuentes N, Limborço H, Viana ER et al (2016) Electronic transport in p-type Mg-doped GaAs nanowires. Phys Status Solidi 5:1–5
22. Han N, Wang F, Hou JJ et al (2012) Controllable p-n switching behaviors of GaAs nanowires via an interface effect. ACS Nano 6:4428–4433
23. Gutsche C, Niepelt R, Gnauck M et al (2012) Direct determination of minority carrier diffusion lengths at axial GaAs nanowire p–n junctions. Nano Lett 12:1453–1458
24. Casadei A, Krogstrup P, Heiss M et al (2013) Doping incorporation paths in catalyst-free be-doped GaAs nanowires. Appl Phys Lett 102:013117

25. Stichtenoth D, Wegener K, Gutsche C et al (2008) P-type doping of GaAs nanowires. Appl Phys Lett 92:163107–113117
26. Gutsche C, Regolin I, Blekker K et al (2009) Controllable p-type doping of GaAs nanowires during vapor-liquid-solid growth. J Appl Phys 105:024305
27. Ullah AR, Meyer F, Gluschke JG et al (2018) P-GaAs nanowire metal–semiconductor field-effect transistors with near-thermal limit gating. Nano Lett 18:5673–5680
28. Lysov A, Vinaji S, Offer M et al (2011) Spatially resolved photoelectric performance of axial GaAs nanowire pn-diodes. Nano Res 4:987–995
29. Okada H, Shikata S, Hayashi H (1991) Electrical characteristics and reliability of Pt/Ti/Pt/au Ohmic contacts to p-type GaAs. Jpn J Appl Phys 30:L558–L560
30. Coleman DJ, Wisseman WR, Shaw DW (1974) Reaction rates for Pt on GaAs. Appl Phys Lett 24:355–357
31. Kumar V (1975) Reaction of sputtered Pt films on GaAs. J Phys Chem Solids 36:535–541
32. Hakkarainen TV, Schramm A, Mäkelä J et al (2015) Lithography-free oxide patterns as templates for self-catalyzed growth of highly uniform GaAs nanowires on Si (111). Nanotechnology 26:275301
33. Rizzo Piton M, Koivusalo E, Hakkarainen T et al (2019) Gradients of be-dopant concentration in self-catalyzed GaAs nanowires. Nanotechnology 30: 335709
34. Toney MF, Brennan S (1989) Observation of the effect of refraction on x rays diffracted in a grazing-incidence asymmetric Bragg geometry. Phys Rev B 39:7963–7966
35. Zhang Z, Yao K, Liu Y et al (2007) Quantitative analysis of current-voltage characteristics of semiconducting nanowires: decoupling of contact effects. Adv Funct Mater 17:2478–2489
36. Orrù M, Repiso E, Carapezzi S et al (2016) A roadmap for controlled and efficient n-type doping of self-assisted GaAs nanowires grown by molecular beam epitaxy. Adv Funct Mater 26:2836–2845
37. Gutsche C, Lysov A, Regolin I et al (2011) Ohmic contacts to n-GaAs nanowires. J Appl Phys 110:014305
38. Chang C-C, Chi C-Y, Yao M et al (2012) Electrical and optical characterization of surface passivation in GaAs nanowires. Nano Lett 12:4484–4489
39. Cole MW, Han WY, Casas LM et al (1994) Pt/Ti/Ge/Pd ohmic contacts to GaAs: a structural, chemical, and electrical investigation. J Vac Sci Technol A Vacuum, Surfaces, Film 12:1904–1909
40. Marvin DC, Ives NA, Leung MS (1985) In/Pt ohmic contacts to GaAs. J Appl Phys 58:2659–2661
41. Wu X, Yang ES, Theodore ND (1990) Structural characterization of Ti and Pt thin films on GaAs (100) substrate. J Electron Mater 19:821–823
42. Cai K, Müller M, Bossert J et al (2005) Surface structure and composition of flat titanium thin films as a function of film thickness and evaporation rate. Appl Surf Sci 250:252–267
43. Arshi N, Lu J, Lee CG et al (2013) Thickness effect on properties of titanium film deposited by d.c. magnetron sputtering and electron beam evaporation techniques. Bull Mater Sci 36:807–812

Publisher's Note

PUBLICATION IV

Evidence of Optical Circular Dichroism in GaAs-Based Nanowires Partially Covered with Gold

Grigore Leahu, Emilija Petronijevic, Alessandro Belardini, Marco Centini, Concita Sibilia, Teemu Hakkarainen, Eero Koivusalo, Marcelo R. Piton, Soile Suomalainen and Mircea Guina

Advanced Optical Materials 5:1601063 (2017)
DOI: 10.1002/adom.201601063

ADVANCED OPTICAL MATERIALS
www.advopticalmat.de

Evidence of Optical Circular Dichroism in GaAs-Based Nanowires Partially Covered with Gold

Grigore Leahu, Emilija Petronijevic, Alessandro Belardini, Marco Centini, Concita Sibilia, Teemu Hakkarainen, Eero Koivusalo, Marcelo Rizzo Piton, Soile Suomalainen, and Mircea Guina*

Semiconductor nanostructures hybridized with metals have been known to offer new opportunities in nonlinear optics, plasmonics, lasing, biosensors; among them GaAs-based nanowires (NWs) hybridized with gold can offer new functionalities, as chiral sensing and light manipulation, as well as circular polarization sources. This study investigates GaAs–AlGaAs–GaAs NWs fabricated by self-catalyzed growth on Si substrates, and partially covered with gold, thus inducing the symmetry breaking and a potential chiral response. Three different samples are investigated, each of them with a different morphology, as the length and the overall diameter ranging from 4.6 to 5.19 μm and from 138 up to 165 nm, respectively. The samples are first characterized by measuring the absorption spectra by using a scattering-free photoacoustic (PA) technique. Then, the circular dichroism (CD) is investigated by measuring PA absorption for circularly polarized light under different incident angles at 532 and 980 nm. An efficient CD is found for proper configurations, and results are in good agreement with extrinsic chiral theory predictions and numerical simulations. It is therefore proven that these samples exhibit chiral behavior, and can be further optimized. Moreover, PA technique can be used as an extremely sensitive and efficient technique to characterize their "extrinsic" chirality.

1. Introduction

Nanostructures with broken symmetry put in interaction with circularly polarized light can mimic the chiral response present in important molecules and DNA. Engineering these structures thus paves the way for the important applications spreading from negative refraction,[1–3] chiral sensing[4,5] to production of optical field carrying out optical angular momentum for quantum information applications.[6] It has been shown that plasmonic nanostructures forming 1D[7] elements, 2D metasurfaces,[8–10] and 3D metamaterials[11] can exhibit linear chiral response due to their own, intrinsic chirality. Also semiconductor nanostructures can exhibit chiral features.[12–16] From the optical point of view, chiral structures possess the ability to rotate the plane of the polarization of electromagnetic waves (optical activity), and give rise to circular dichroism—i.e., the difference in the absorption of right- and left-handed circular polarized light.

Apart from 3D chiral objects, the possibility to obtain optical chirality, i.e., optical activity, with nonchiral elements was studied in the past,[17] but only recently reconsidered.[18,19] This phenomenon is obtained when the experimental configuration composed by both the nonchiral object and the optical incident field is nonsuperimposable on its mirror image.[20] This is called "extrinsic" chirality; in our previous works we have investigated this type of chirality in tilted golden nanowires by means of both linear (reflection and absorption) and nonlinear (second harmonic generation) measurements.[20–23]

III–V semiconductor nanowires (NWs) have been widely investigated since they exhibit good waveguiding properties thus offering a light manipulation at nanoscale. Coupling of the incident light to the discrete leaky waveguide modes above the bandgap in NWs leads to increased resonant absorption, thus paving the way for important applications such as energy harvesting, spectral selectivity, lasing, spin angular momentum generation, etc.[24–27] Metallic NWs have also been investigated for plasmonic laser applications[28–30] and possibility of surface plasmon polaritons excitation.[31] One step further is the partial covering of such NWs with gold: this can induce, along with the proper experiment setup, the symmetry breaking which leads to chiral response.

In this paper, for the first time to our knowledge, we report on a circular dichroism behavior from semiconductor hexagonal

Dr. G. Leahu, E. Petronijevic, Dr. A. Belardini, Dr. M. Centini, Prof. C. Sibilia
SBAI Department
Sapienza University of Rome
Via Antonio Scarpa 16, Rome 00161, Italy
E-mail: concita.sibilia@uniroma1.it
Dr. T. Hakkarainen, E. Koivusalo, M. Rizzo Piton, Dr. S. Suomalainen, Prof. M. Guina
Optoelectronics Research Centre
Tampere University of Technology
Korkeakoulunkatu 3, 33720 Tampere, Finland
M. Rizzo Piton
Departamento de Física
Universidade Federal de São Carlos
CP 676 São Carlos, SP, Brazil

DOI: 10.1002/adom.201601063

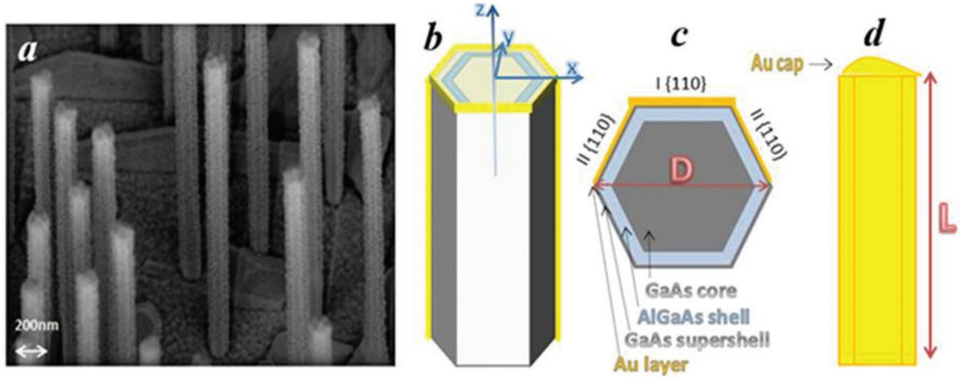

Figure 1. GaAs-based NWs partially covered with Au. a) Tilted (30°) SEM image of 3D distribution of S2. b) 3D schematic of the NW from the side not covered with Au (Au tip is made transparent to show GaAs–AlGaAs–GaAs configuration). c) *x*–*y* cross section with characteristic parameters: overall diameter *D*, which comprises GaAs core, AlGaAs shell, GaAs supershell. Au layer thickness on the sidewalls depends on the Au flux – the (110) sidewalls in the azimuthal flux direction (I{110}) are t_{gold_1} = 20 nm thick, while two other neighboring (110) facets (II{110}) are t_{gold_2} = 10 nm thick. d) *x*–*z* cross section from the Au-covered side. The Au cap is shaped depending on the direction of the flux, and its thickness varies from 20 to 40 nm.

nanowires partially covered by gold. The NWs were fabricated by means of molecular beam epitaxy on p-Si(111) using a lithography-free oxide patterning. This technique enables fabrication of highly uniform NW ensembles with tailorable NW density.[32] They were then exposed to a tilted flux of Au that resulted in nonuniform gold layers above the three sides and the tip of the NWs. The light that impinges on such structures under a proper oblique angle will be differently absorbed for circular polarizations of opposite handedness; this optical activity is usually indirectly measured as a difference in power transmitted/reflected by the chiral nanostructure-setup. More recently, we have shown that photoacoustic technique can be applied to directly measure circular dichroism in arrays of tilted gold NWs[23] as well as size-dependent resonant absorption properties of semiconductor NWs.[33] Here, we apply the same technique to investigate the "extrinsic" chirality in GaAs-based metal–semiconductor hybrid NWs under two wavelengths, 532 and 980 nm, corresponding to optical region of different light absorption by GaAs. Such composite material opens several interesting possibilities compared to metal NWs. The semiconductor NW not only acts as a waveguide and scaffolding for the metal structure but can also effectively convert photons to electron–hole-pairs and vice versa. This property is exploited in NW solar cells, photodetectors, and light-emitting diodes by incorporating a pn-junction within the NW. We believe that hybrid nanostructures combining the chiral optical response provided by the asymmetric metal and optoelectronic functionality of the semiconductor NWs can lead to nanophotonic applications in chiral sensing and light manipulation, as well as circular polarization sources.

2. Sample Fabrication

The coaxial GaAs–AlGaAs core–shell nanowires were grown by molecular beam epitaxy on p-Si(111) wafers using lithography-free Si/SiO_x patterns for defining the nucleation sites. The GaAs core was first grown by self-catalyzed growth mode. Then, the Ga catalyst droplet was consumed in As_2-flux in order to terminate axial growth. The $Al_{0.3}Ga_{0.7}As$ shell and GaAs supershell were then grown around the NW core using growth conditions that promote radial growth. The details of the Si/SiO_x pattern fabrication and NW growth are explained in details in ref. [24]. The NWs exhibit remarkably phase-pure zincblende crystal structure with the exception of short wurtzite segments formed at the tip of the NW during droplet crystallization when changing from axial to radial growth, see high-resolution transmission electron microscopy images and high-resolution X-ray diffraction spectra on similar samples in our recent paper.[34] The Au film was deposited on the NWs by electron beam evaporation. The incident angle of the Au-flux was 14° with respect to the NW axis. The NWs have hexagonal cross-section defined by (110)-facetted sidewalls. One of the (110) facetted NW sidewalls was selected as the azimuthal direction of the Au flux. The nominal Au thickness on this facet is t_{gold_1} = 20 nm, while on the neighboring (110) facets the Au thickness is t_{gold_2} = 10 nm due to flux geometry.

In **Figure 1**a, the tilted (30°) scanning electron microscopy (SEM) image of 3D distribution of one of the samples (S2 in **Table 1**) is shown. The 3D schematic and the *x*–*y* cross section are shown in Figure 1b,c, respectively. Characteristic geometric parameters are the NW length *L*, the overall diameter *D*, AlGaAs shell thickness t_{AlGaAs}, and GaAs supershell thickness t_{GaAs}. In Figure 1d, *x*–*z* cross section from the Au-covered side is shown. The Au cap is shaped depending on the direction of the flux, and its thickness varies from 20 to 40 nm. We test three samples having different lengths and diameters in order to experimentally

Table 1. Characteristic geometric parameters for the three samples together with their standard deviations. The samples exhibit low fabrication error margins.

Sample	*L* [nm]	*D* [nm]	t_{AlGaAs} [nm]	t_{GaAs} [nm]	t_{gold_1} [nm]	t_{gold_2} [nm]
S1	4750 ± 34	138 ± 5	3.5	0.7	20	10
S2	5190 ± 64	151 ± 5	8.6	1.7	20	10
S3	4600 ± 52	165 ± 6	11.7	5.8	20	10

evaluate the dependence of the CD signal to the geometrical parameters of the nanostructures and the fabrication tolerances (see Table 1 for geometrical data of the three samples—the Au evaporation parameters are equal for all the samples).

3. Photoacoustic Technique and Linear Characterization

We first experimentally characterize our samples by measuring their absorption by means of the photoacoustic (PA) technique. This technique is based on the generation of heat when a sample absorbs an incoming light beam. If the light intensity is modulated in time, a cycle of heating up and cooling down will correspond to changes in pressure that further produces an acoustic signal. The acoustic signal is then converted into electrical one by a sensitive microphone. This microphone is connected to the cell through a small tunnel, so that the scattered light cannot significantly contribute to PA signal, as shown in the inset of **Figure 2**a. Therefore, PA technique directly measures scattering independent absorption in the samples. It has been widely applied to characterize plasmonic nanoparticles and metasurfaces.[35–39]

We recently applied this technique to measure the resonant absorption in the NW samples of same geometric parameters before they had been exposed to Au flux.[33] Similar PA setup is shown in Figure 2a: the samples are shined from the air side by a Xenon arc lamp source followed by a monochromator, which provides the spectral range from 300 to 1100 nm. We show normal incidence absorption spectra for the samples S1–S3 in Figure 2b. The absorption maxima around 700–800 nm and 450–500 nm originate from HE_{11} and HE_{12} guided modes present in GaAs-based dielectric hexagonal NWs; however, due to the nonuniform Au layer and the interaction between close NWs, these maxima are significantly broadened. To simulate the absorption cross section of a single GaAs–AlGaAs–GaAs NW covered with Au we have used Lumerical finite difference time domain (FDTD). To take into account the interaction between the closely spaced NWs, we simulate two NWs whose distance is taken from the nearest neighbor statistics from top SEM images. The good agreement between numerical and PA spectra allows the assumption that the calculations will fit the PA experiments for circular incident light too.

4. Chiral Absorption Results

4.1. PA Circular Dichroism Setup

Since Au does not uniformly and symmetrically cover the hexagonal NWs, under oblique incidence, these structures promise to exhibit chiral effects under proper configurations. Therefore, we change our PA setup in order to be able to scan polarization and incidence angles, **Figure 3**a. We use two laser wavelengths: 532 nm to report on the range where all of the NW materials and Au strongly absorb energy, and 980 nm, where

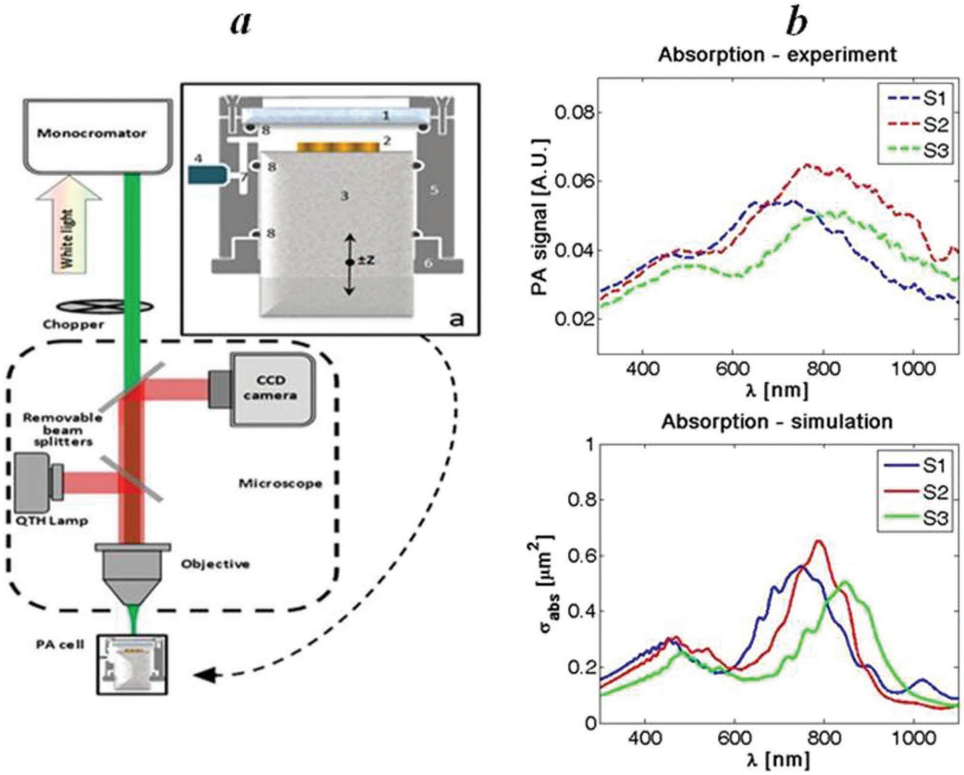

Figure 2. a) Experimental setup of the photoacoustic measurement. Inset (a): Variable volume photoacoustic cell, 1-quartz window, 2-sample, 3-quartz cylinder, 4-microphone, 5-inox cell body, 6-threaded flange, 7-sound labyrinth, 8-O-ring. b) PA spectra (dashed lines) and simulated absorption cross section (solid lines) of the three samples (S1 blue curves, S2 red curves, S3 green curves).

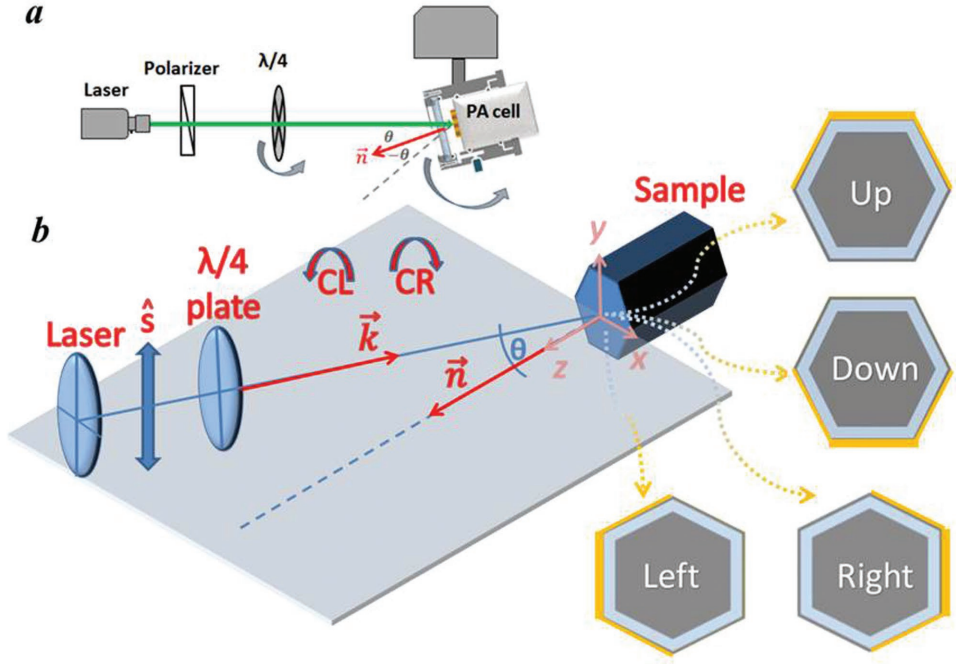

Figure 3. a) Top view of the circular dichroism measurements setup. Laser light at the wavelength of 532 or 980 nm is polarized so that it impinges with $\hat{s}$ polarization on a quarter wave plate. Rotational stage allows for the incident angle scan. b) 3D view of the experiment with four x–y plane configurations when primary I{110} sidewall is in: y_+ region – Up, y_- – Down, x_+ – Right, and x_- – Left.

GaAs and AlGaAs are almost nonabsorbing, while Au strongly reflects light (Si substrate is the only material that absorbs at 980 nm). The laser light is polarized before the quarter wave plate, so that it is $\hat{s}$-polarized when the fast wave plate's axis is at 0°. Fast axis wave plate scans the angles from −180° to 180°, where −45° represents left-handed circular polarization (CL) and 45° represents right-handed circular polarization (CR). PA cell is mounted on a rotational stage, which enables the incidence angle scan from $\theta = -56°$ to 56°, as well as four different NW configurations (see Figure 3b); NW primary sidewall covered with Au can be in xz plane toward y_+ direction (Up configuration), xz plane toward y_- direction (Down configuration), yz plane toward x_+ direction (Right configuration), and yz plane toward x_- direction (Left configuration).

4.2. CD Dependence on the Incidence Angle

As a figure of merit that defines the level of circular dichroism in PA measurements, we use

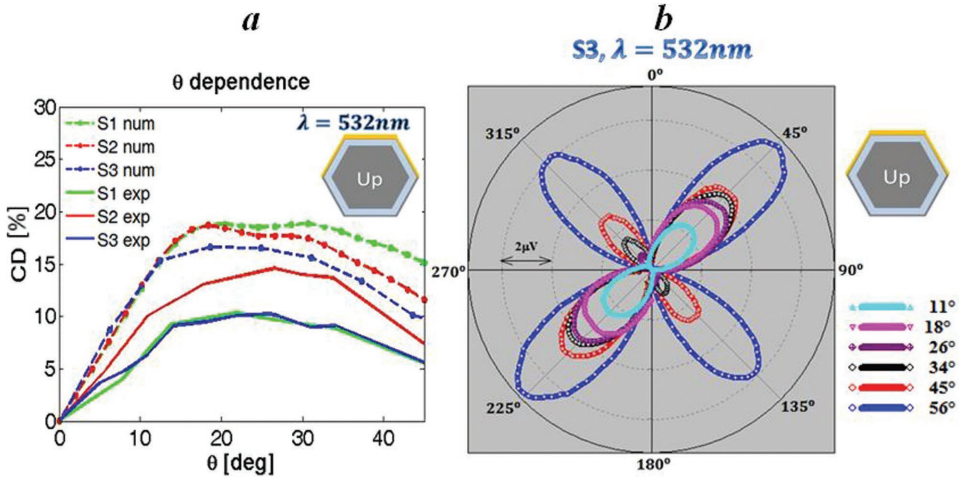

Figure 4. a) CD incidence angle dependence (experimental measured values in solid lines, numerical values in dashed lines) for the samples S1–S3 for the Up configuration at 532 nm; Sample S1 in green, S2 in red, S3 in blue. b) PA polar plots for S3 at 532 nm in Up configuration for various angles of incidence: 11° cyan, 18° magenta, 26° violet, 34° black, 45° red, 56° blue.

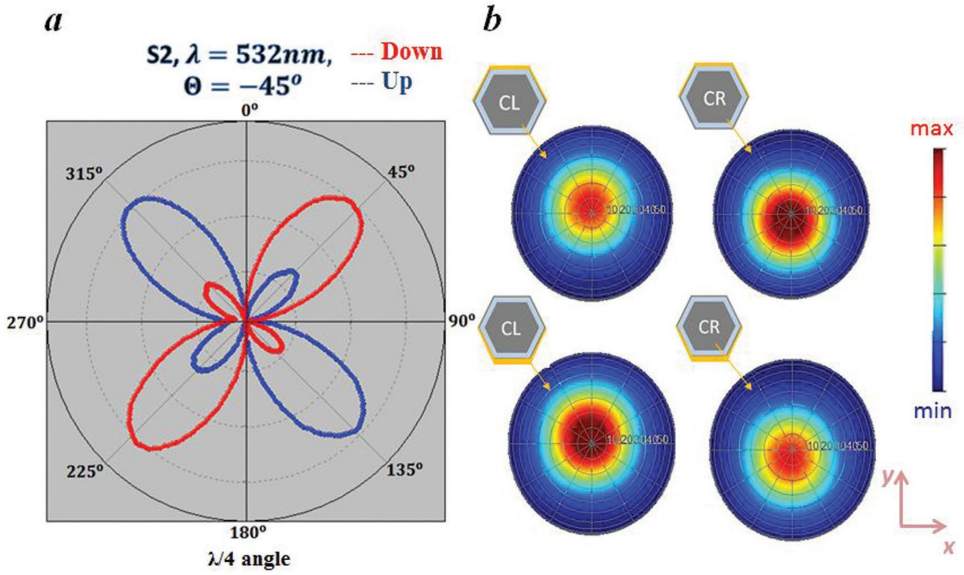

Figure 5. a) Polar plots of PA signal for Up (blue curve) and Down (red curve) configurations of S2 at 532 nm and −45° incidence. CD switches sign between the two configurations. b) Reflection far field intensity at 45° incidence for CL and CR impinging light in Up and Down configurations; we see that changing the input polarization from CL to CR we can control the reflected field intensity and direction (the centers of the plots indicate the specular reflection).

$$\mathrm{CD}[\%] = \frac{A_{\mathrm{CL}} - A_{\mathrm{CR}}}{A_{\mathrm{CL}} + A_{\mathrm{CR}}} \times 100 \quad (1)$$

where A_{CL} (A_{CR}) stands for the PA signal amplitude for CL (CR) polarization. In **Figure 4**a, we show measured (solid lines) and calculated (dashed lines) CD as a function of the incident angle for the three samples at 532 nm in Up configuration. We see that in all three samples CD increases from 0% at normal incidence, since both the setup and the structure are symmetric; in both Left and Right configurations, as well as for NWs samples without the asymmetric gold cover, CD is negligible, as the circularly polarized light does not see the symmetry breaking. CD

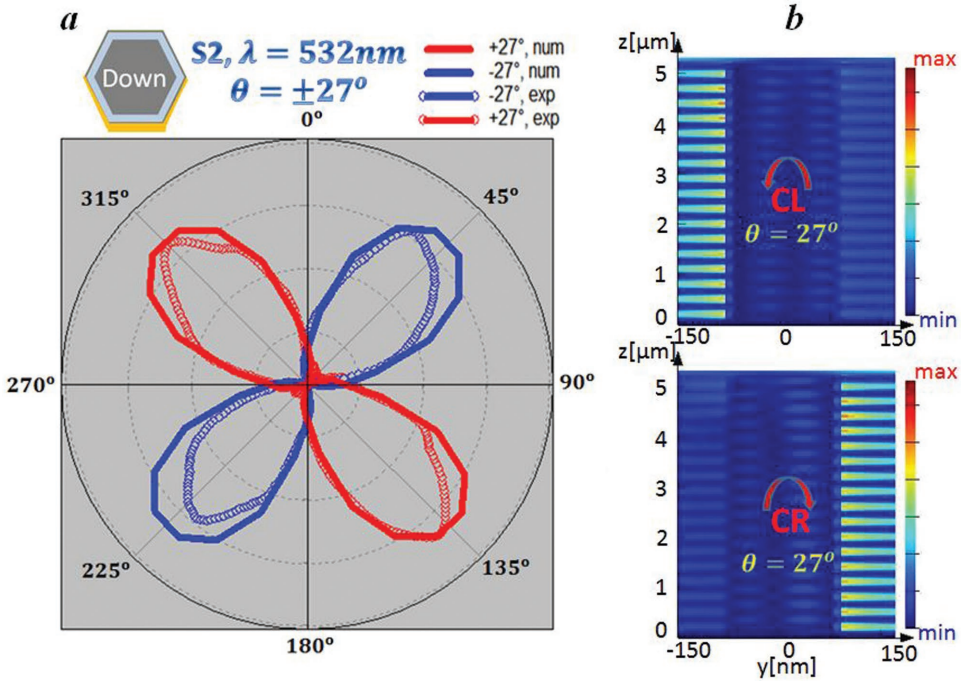

Figure 6. a) Polar plots (experimental values in open circles and numerical ones in solid lines) for Down configurations of S2 at 532 nm for −27° (blue) and 27° (red) incidence. CD has a 90° shift between these two configurations. b) Intensity of the electric field in *y*–*z* cross section when S2 is excited with CR or CL at 27°.

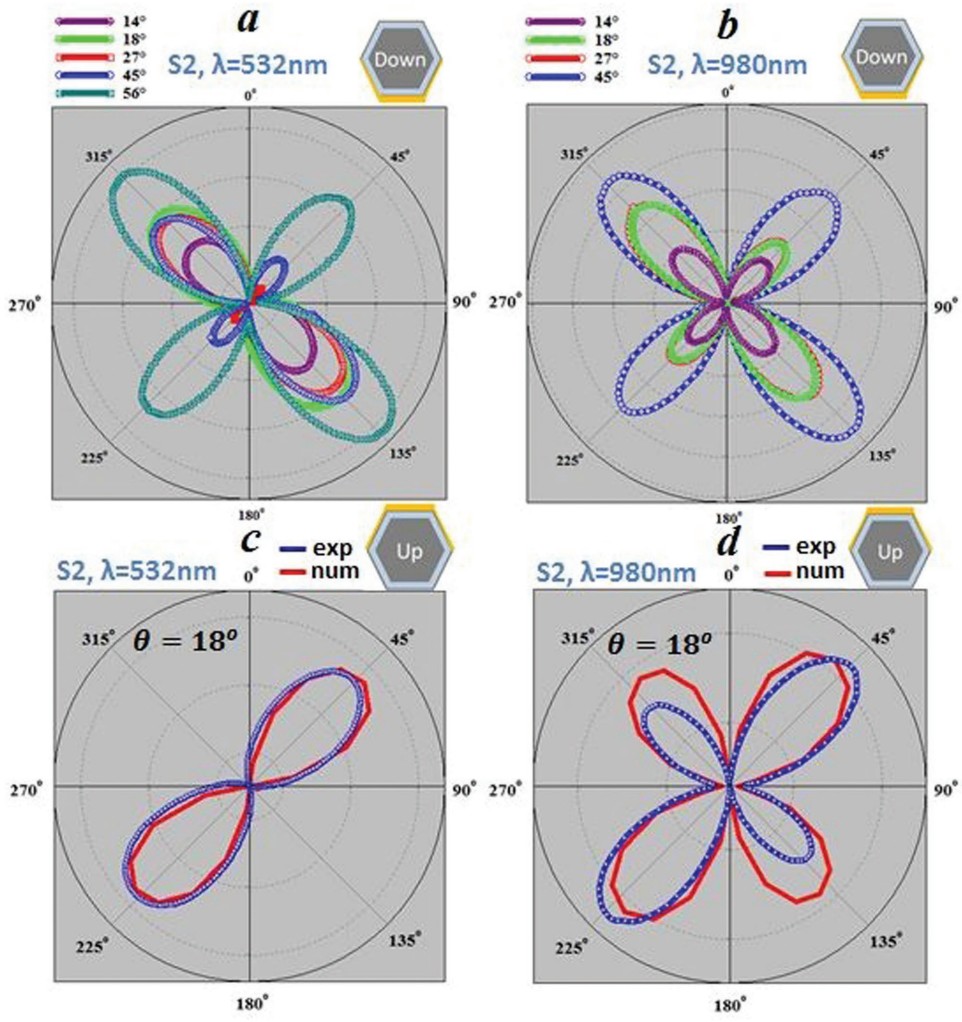

Figure 7. a) Polar plots of the PA signal obtained on sample S2 in Down configuration for different incidence angles at the wavelength of 532 nm. b) Polar plots of the PA signal obtained on sample S2 in Down configuration for different incidence angles at the wavelength of 980 nm. c) Numerical (red curve) and experimental (blue curve) PA signal for sample S2 at 18° of incidence at 532 nm in Up configuration. d) Numerical (red curve) and experimental (blue curve) PA signal are shown for sample S2 at 18° of incidence at 980 nm in Up configuration.

follows the form of the numerically calculated dependence, and the experimental maximum CD of 8% is reached for S2 at 27°; this sample has the longest L, while S1 and S3 have similar shorter L, which leads to a smaller CD. Thus, the results of the measurements in Figure 4a indicate that the dominant parameter in CD signal is attributed to the length of NWs, while the diameter does not have a strong influence on the chiral response. On the contrary, the diameter strongly affects the linear response of gold-free NWs.[33] However, PA signal has also a high contribution of a nonchiral Si substrate, while the simulations take into account just its small depth (limited by the calculation region), thus slightly overestimating CD. We attribute the other discrepancies to the fact that single NW simulations cannot completely catch the collective behavior due to the NW interactions and to the variations of fabrication parameters such as Au cap thickness. In Figure 4b, the polar plot of the PA signal is shown for S3 at 532 nm in Up configuration (0° corresponds to $\hat{s}$-polarized light) for different input angles of the impinging light. The difference between the lobes corresponding to CL and CR is strong at 11°, 18°, and 26°, while from 34° this difference decreases. Similar plots have been obtained for S1 and S2 samples.

Since sample S2 gives rise to the higher CD signal, in what follows we perform more detailed measurements on S2 by looking at different experimental geometries.

4.3. CD for Up and Down Configurations

In **Figure 5**a, we present polar plots of PA signals for the angle of incidence $\theta = -45°$, at 532 nm, for Down (red curve) and Up (blue curve) configurations. As expected from the theory of "extrinsic" chirality, the circular dichroism reverses its sign passing from Up to Down configuration. This influences also on the shape of the electromagnetic field reflected from the structure. In Figure 5b, we show the calculated reflection far field intensity at $\theta = 45°$ incidence for CL and CR illumination in Up and Down configurations. Both direction and intensity

of the reflected light change in these four combinations with respect the specular reflection direction, which indicates as possible applications of such NWs, the control the direction and intensity of the light.

4.4. Maximum CD at Opposite Incidence Angles

In **Figure 6**a, we show PA polar plot for the Down configuration, in the conditions where the maximum CD is achieved which is obtained for the sample S2 at around $\theta = 27°$ at 532 nm (see Figure 4a). As expected, the chiral feature shows 90° shift in polarization for the incidence angle of $\theta = -27°$. The "extrinsic" chirality is strong and we see no additional lobes.

It is also interesting to evaluate the field profile in the NW when the CD occurs. In Figure 6b, the simulations of the electric field intensity are shown if S2 is excited under $\theta = 27°$ at 532 nm wavelength. For CR the field is concentrated on the gold-covered sidewalls, while for CL it is concentrated on the opposite side. This suggests that these NWs could provide light path and polarization control. In particular, they could enable a completely new approach for chiral sensing in the form of hot electron Schottky photodetector[40] exploiting the circular polarization dependent plasmonic absorption at GaAs–Au interface.

4.5. Maximum CD at Different Wavelengths

We further examine the behavior at two different wavelengths: 532 and 980 nm. Since at 532 nm both Au and NW materials contribute to the absorption, while at 980 nm NWs are transparent and Au strongly reflects light, we expect CD to be significantly greater at 532 nm.

Indeed, angular dependence, gave CD values 50% lower at 980 nm with respect to 532 nm. In **Figure 7**, we report the comparison among the polar plots obtained at the above-mentioned wavelengths. In Figure 7a are shown the polar plots of the PA signal obtained on sample S2 in Down configuration for different incidence angles at the wavelength of 532 nm. In Figure 7b, we show the polar plots of the PA signal obtained in the same conditions at the wavelength of 980 nm. In Figure 7c, both numerical (red curve) and experimental (blue curve) PA signal are shown for sample S2 at $\theta = 18°$ of incidence at 532 nm in Up configuration; in Figure 7d, PA signal in the same condition at the wavelength of 980 nm is reported. We see that FDTD numerical simulations can efficiently predict the chiral behavior of these NW ensembles. This means that we can improve our fabrication parameters to optimize CD at wanted wavelengths, leading to unprecedented applications in chiral NW-based devices.

5. Conclusions

We experimentally investigate the effective chiral behavior of GaAs-based nanowire ensembles partially covered by gold. The employed fabrication process allows for the fabrication of highly uniform GaAs–AlGaAs NW ensembles; exposing them to the tilted Au flux leads to the asymmetric structure that exhibits CD behavior. The "extrinsic" chiral behavior was confirmed by measuring the differences in absorption of circular incident light of opposite handedness. Our scattering-independent PA setup directly measures the absorption and allows scanning of incidence angles and polarization. We have measured configurations with different symmetry and incidence angles, under two particular wavelengths, and numerically confirmed results by means of FDTD simulations. NW fabrication parameters can be further easily optimized to improve CD. By testing three samples having different dimensions, we infer that the NW diameter does not have a strong influence on the chiral response, while the length has a major effect; the strongest chiral response is observed for the longest NWs.

We strongly believe that bringing together the advantages of a semiconductor optoelectronics platform, waveguiding properties of vertical NWs, and chiral behavior when their symmetry is broken could lead to new perspectives in control of light at nanoscale and in developing new chiral sensing devices. To this end, our current efforts are dedicated to the development of prototype chiral photodetectors based on asymmetrically metal coated GaAs NWs including pn-junctions for collecting charge carriers.

Acknowledgements

The funding from the Academy of Finland Project NESP (decision number 294630) and NANoS (decision number 260815) is acknowledged.

Received: December 15, 2016
Revised: January 18, 2017
Published online:

[1] J. B. Pendry, *Science* **2004**, *306*, 1353.
[2] J. Zhou, J. Dong, B. Wang, T. Koschny, M. Kafesaki, C. M. Soukoulis, *Phys. Rev. B* **2009**, *79*, 121104 (R).
[3] S. Zhang, Y. Park, J. Li, X. Lu, W. Zhang, X. Zhang, *Phys. Rev. Lett.* **2009**, *102*, 023901.
[4] A. Kuzyk, R. Schreiber, Z. Fan, G. Pardatscher, E. Roller, A. Högele, F. C. Simmel, A. O. Govorov, T. Liedl, *Nature* **2012**, *483*, 311.
[5] Y. He, K. Lawrence, W. Ingram, Y. Zhao, *Chem. Commun.* **2016**, *52*, 2047.
[6] A. M. Yao, M. J. Padgett, *Adv. Opt. Photonics* **2007**, *446*, 3.
[7] H. K. Bisoyi, Q. Li, *Acc. Chem. Res.* **2014**, *47*, 3184.
[8] C. Wu, N. Arju, G. Kelp, J. A. Fan, J. Dominguez, E. Gonzales, E. Tutuc, I. Brener, G. Shvets, *Nat. Commun.* **2014**, *5*, 3892.
[9] V. K. Valev, J. J. Baumberg, B. De Clercq, N. Braz, X. Zheng, E. J. Osley, S. Vandendriessche, M. Hojeij, C. Blejean, J. Mertens, C. G. Biris, V. Volskiy, M. Ameloot, Y. Ekinci, G. A. E. Vandenbosch, P. A. Warburton, V. V. Moshchalkov, N. C. Panoiu, T. Verbiest, *Adv. Mater.* **2014**, *26*, 4074.
[10] V. K. Valev, J. J. Baumberg, C. Sibilia, T. Verbiest, *Adv. Mater.* **2013**, *25*, 2517.
[11] J. K. Gansel, M. Thiel, M. S. Rill, M. Decker, K. Bade, V. Saile, G. von Freymann, S. Linden, M. Wegener, *Science* **2009**, *325*, 1513.
[12] Y. Zhou, M. Yang, K. Sun, Z. Tang, N. A. Kotov, *J. Am. Chem. Soc.* **2010**, *132*, 6006.
[13] Y. Xia, Y. Zhou, Z. Tang, *Nanoscale* **2011**, *3*, 1375.

[14] Y. Zhou, Z. Zhu, W. Huang, W. Liu, S. Wu, X. Liu, Y. Gao, W. Zhang, Z. Tang, *Angew. Chem., Int. Ed.* **2011**, *50*, 11456.
[15] Y. Li, Y. Zhou, H. Y. Wang, S. Perrett, Y. Zhao, Z. Tang, G. Nie, *Angew. Chem., Int. Ed.* **2011**, *50*, 5860.
[16] Z. Zhu, J. Guo, W. Liu, Z. Li, B. Han, W. Zhang, Z. Tang, *Angew. Chem., Int. Ed.* **2013**, *52*, 13571.
[17] T. Verbiest, M. Kauranen, Y. van Rompaey, A. Persoons, *Phys. Rev. Lett.* **1996**, *77*, 1456.
[18] E. Plum, X.-X. Liu, V. A. Fedotov, Y. Chen, D. P. Tsai, N. I. Zheludev, *Phys. Rev. Lett.* **2009**, *102*, 113902.
[19] S. N. Volkov, K. Dolgaleva, R. W. Boyd, K. Jefimovs, J. Turunen, Y. Svirko, B. K. Canfield, M. Kauranen, *Phys. Rev. A* **2009**, *79*, 043819.
[20] M. Bertolotti, A. Belardini, A. Benedetti, C. Sibilia, *J. Opt. Soc. Am. B* **2015**, *32*, 1287.
[21] A. Belardini, M. C. Larciprete, M. Centini, E. Fazio, C. Sibilia, *Phys. Rev. Lett.* **2011**, *107*, 257401.
[22] A. Belardini, M. Centini, G. Leahu, E. Fazio, C. Sibilia, J. W. Haus, A. Sarangan, *Faraday Discuss.* **2015**, *178*, 357.
[23] A. Belardini, M. Centini, G. Leahu, D. C. Hooper, R. Li Voti, E. Fazio, J. W. Haus, A. Sarangan, V. K. Valev, C. Sibilia, *Sci. Rep.* **2016**, *6*, 31796.
[24] B. Mayer, D. Rudolph, J. Schnell, S. Morkötter, J. Winnerl, J. Treu, K. Müller, G. Bracher, G. Abstreiter, G. Koblmüller, J. J. Finley, *Nat. Commun.* **2013**, *4*, 2931.
[25] B. Mayer, L. Janker, B. Loitsch, J. Treu, T. Kostenbader, S. Lichtmannecker, T. Reichert, S. Morkötter, M. Kaniber, G. Abstreiter, C. Gies, G. Koblmüller, J. J. Finley, *Nano Lett.* **2016**, *16*, 152.
[26] S. Mokkapati, D. Saxena, H. H. Tan, C. J. Jagadish, *Sci. Rep.* **2015**, *5*, 15539.
[27] M. H. Alizadeh, B. M. Reinhard, *Opt. Express* **2016**, *24*, 8471.
[28] T. P. H. Sidiropoulos, R. Röder, S. Geburt, O. Hess, S. A. Maier, C. Ronning, R. F. Oulton, *Nat. Phys.* **2014**, *10*, 870.
[29] X. Wu, Y. Xiao, C. Meng, X. Zhang, S. Yu, Y. Wang, C. Yang, X. Guo, C. Z. Ning, L. Tong, *Nano Lett.* **2013**, *13*, 5654.
[30] R. F. Oulton, V. J. Sorger, T. Zentgraf, R. Ma, C. Gladden, L. Dai, G. Bartal, X. Zhang, *Nat. Lett.* **2009**, *461*, 629.
[31] S. Zhang, H. Wei, K. Bao, U. Håkanson, N. J. Halas, P. Nordlander, H. Xu, *Phys. Rev. Lett.* **2011**, *107*, 096801.
[32] T. V. Hakkarainen, A. Schramm, J. Mäkelä, P. Laukkanen, M. Guina, *Nanotechnology* **2015**, *26*, 275301.
[33] G. Leahu, E. Petronijevic, A. Belardini, M. Centini, R. Li Voti, T. Hakkarainen, E. Koivusalo, M. Guina, C. Sibilia, **2017**, unpublished.
[34] E. Koivusalo, T. Hakkarainen, M. Guina, **2017**, arXiv:1701.04264. arXiv.org e-Print archive. https://arxiv.org/abs/1701.04264 (accessed: February 2017).
[35] R. Inagaki, K. Kagami, E. T. Arakawa, *Phys. Rev. B* **1981**, *24*, 3644R.
[36] R. Inagaki, K. Kagami, E. T. Arakawa, *Appl. Opt.* **1982**, *21*, 949.
[37] T. El-Brolossy, T. Abdallah, M. Mohamed, S. Abdallah, K. Easawi, S. Negm, H. Talaat, *Eur. Phys. J.: Spec. Top.* **2008**, *153*, 361.
[38] R. Li Voti, G. Leahu, M. C. Larciprete, C. Sibilia, M. Bertolotti, I. Nefedov, I. V. Anoshkin, *Int. J. Thermophys.* **2015**, *36*, 1342.
[39] S. J. Zelewski, J. Kopaczek, W. M. Linhart, F. Ishikawa, S. Shimomura, R. Kudrawiec, *Appl. Phys. Lett.* **2016**, *109*, 182106.
[40] W. Li, J. G. Valentine, *Nanophotonics* **2017**, *6*, 177.

PUBLICATION V

Demonstration of extrinsic chirality of photoluminescence with semiconductor-metal hybrid nanowires

Teemu Hakkarainen, Emilija Petronijevic, Marcelo Rizzo Piton and Concita Sibilia

Scientific Reports 9:1-8 (2019)
DOI: 10.1038/s41598-019-41615-1

SCIENTIFIC REPORTS

OPEN

Demonstration of extrinsic chirality of photoluminescence with semiconductor-metal hybrid nanowires

Received: 24 January 2019
Accepted: 8 March 2019
Published online: 25 March 2019

Teemu Hakkarainen[1], Emilija Petronijevic[2], Marcelo Rizzo Piton[1,3] & Concita Sibilia[2]

Chiral optical response is an inherent property of molecules and nanostructures, which cannot be superimposed on their mirror images. In specific cases, optical chirality can be observed also for symmetric structures. This so-called extrinsic chirality requires that the mirror symmetry is broken by the geometry of the structure together with the incident or emission angle of light. From the fabrication point of view, the benefit of extrinsic chirality is that there is no need to induce structural chirality at nanoscale. This paper reports demonstration extrinsic chirality of photoluminescence emission from asymmetrically Au-coated GaAs-AlGaAs-GaAs core-shell nanowires fabricated on silicon by a completely lithography-free self-assembled method. In particular, the extrinsic chirality of PL emission is shown to originate from a strong symmetry breaking of fundamental HE_{11} waveguide modes due to the presence of the asymmetric Au coating, causing preferential emission of left and right-handed emissions in different directions in the far field.

Chirality is an intrinsic property of structure that cannot be superimposed on its mirror image[1]. Such lack of mirror symmetry is found in DNA, proteins, sugars, viruses, and amino acids among other important molecules and building blocks of life. The interaction of chiral molecules with light is different for left and right-handed circular polarizations[2]. This so-called circular dichroism (CD) of chiral molecules is typically observed in light absorption[3]. The optical response of chiral molecules can be mimicked with artificial nanostructures with chiral shape[4] fabricated using nanolithography[5], focused ion beam-induced deposition[6] and other nanofabrication methods. On the other hand, chiral optical response can be accessed also with structures that themselves are not chiral, given that specific conditions are fulfilled. This extrinsic optical chirality requires that the geometry of the structure and, for example, the incidence angle of light together break the mirror symmetry, as it has been demonstrated for absorption[7], transmission[8], reflection[9], optical activity[10,11] and non-linear response[12]. The benefits of extrinsic chirality include easier fabrication and freedom of design, as it is not required to induce structural chirality at nanoscale. Furthermore, same structure can be used to interact with both circular polarizations by changing incidence angle or orientation of the structure. The chiral optical response can be extended also to light emission. Luminescent chiral molecules can emit preferentially either left-handed or right-handed circular polarization depending on their handedness[13,14], while in semiconductors circular polarized photoluminescence (PL) is associated with different spin states of charge carriers[15]. There are only few reports of extrinsic chiral effects in light emission. Yokoyama *et al.* reported circular polarization dependence of excitation in photoluminescence from carbon nanotubes placed on nanostructured silicon surface[16], while Yan *et al.* used extrinsic chirality provided by an array of metal nanoantennas for splitting left and right-handed circular polarizations of fluorescence from achiral fluorophores in different direction in the far field[17].

In the application point of view, the semiconductors have significant benefits in the integration with the existing optoelectonic and microelectronic technologies. In particular, direct bandgap III-V semiconductor nanowires (NW) of high optical and electrical quality can be grown directly on silicon substrates by Au-catalyzed[18,19] and self-catalyzed[20] vapor-liquid-solid method[21]. Owing the their geometry and high refractive index, semiconductor

[1]Optoelecronics Research Centre, Physics Unit, Tampere University, Korkeakoulunkatu 3, FI-33720, Tampere, Finland. [2]Department S.B.A.I., Sapienza Università di Roma, Via A. Scarpa 14, I-00161, Rome, Italy. [3]Departamento de Física, Universidade Federal de São Carlos, CP 676 São Carlos, São Paulo, Brazil. Correspondence and requests for materials should be addressed to T.H. (email: teemu.hakkarainen@tuni.fi)

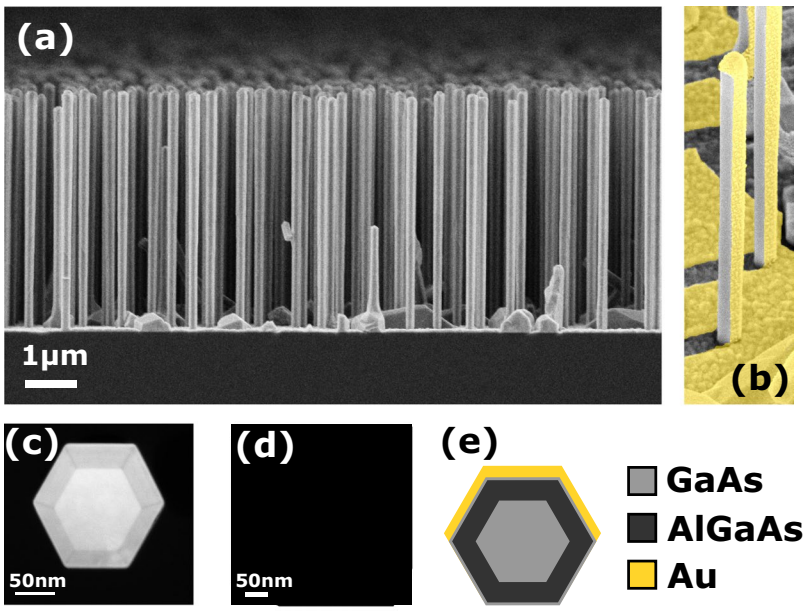

Figure 1. Structural details of the investigated NWs. (**a**) SEM edge view the sample with NWs 4690 ± 80 nm long, of the overall diameter 197 ± 9 nm. (**b**) False color SEM image of the NWs after Au deposition. (**c**) Cross-sectional dark-field TEM micrograph showing GaAs core, AlGaAs shell and GaAs supershell. (**d**) Cross-sectional TEM image of the NW asymmetrically covered by Au. (**e**) Cross-sectional sketch of the NW materials.

NWs can effectively confine and manipulate electromagnetic fields in the visible and near infrared wavelengths. These properties are essential for several NW device concepts[22–26], where coupling of the light to the resonant modes of the nanostructure[27,28] can tailor the light absorption[29,30], extraction and directionality of emission[31–35], as well as stimulated emission[36,37]. More recently, we have shown that asymmetrically Au-coated NWs exhibit extrinsic chirality and CD in absorption at the wavelengths where the incident light is coupled to the waveguide modes[38].

Here, we demonstrate extrinsic chirality of PL emission from hybrid semiconductor-metal structures consisting of asymmetrically Au-coated GaAs-AlGaAs core-shell NWs grown on silicon substrates. The chiral PL emission from the GaAs core with linear polarized excitation originates from a strong symmetry breaking of HE_{11} modes due to the presence of Au on three of the six (111) sidewalls, leading to a preferential directionality of left and right-handed circular polarizations in different angles in the far field. A unique property of this concept is that the intrinsic waveguiding properties of the NWs are modified with the external Au layer to provide extrinsic chirality of light emission. Furthermore, they are fabricated with a completely lithography-free, self-assembled technique and potentially also allow electrical injection for LED operation by incorporating a PN-junction in the NW, thus providing a chiral light manipulation platform for applications spanning from quantum information technology to biology and chemistry.

Experimental Methods

The investigated sample consists of vertically standing NWs grown by molecular beam epitaxy on Si(111) wafers using lithography-free Si/SiOx patterning technique for defining the nucleation sites[39]. This technique has been recently proven to provide vertical NW forests with highly uniform dimensions[40,41]. Consequently, the optical response of the ensemble is strongly governed by the single NW response simulated assuming the mean values of the NW dimensions[30,38]. The NW structure includes a GaAs core, an AlGaAs shell and an GaAs supershell. The overall diameter of the NW is $D = 197 \pm 9$ nm, which includes a 27.7 nm thick AlGaAs passivation shell, and a 5.5 nm GaAs supershell. The length is 4690 ± 80 nm and density around 1×10^8 cm^{-2}. These structural parameters are mean values from statistical analysis of a large number of NWs[30]. Figure 1a shows an edge-view scanning electron microscope (SEM) image of the NWs investigated in this work. The growth of the GaAs-AlGaAs-GaAs core-shell heterostructure NWs is reported in ref.[39]. The semiconductor-metal hybrid structures were obtained by growing a thin Au layer on the NWs using electron beam evaporation. The NW sample was tilted in a 14° angle in order to obtain the asymmetric structure presented in Fig. 1b. The Au flux angle was chosen based on the average length and nearest neighbor statistics of the NWs, thus minimizing the shadowing effects as shown in the Supplementary Fig. S1. The sample orientation with respect to the Au flux and the deposition time were chosen in such way that one of the NW side facets would get nominally a 20 nm thick and the two side adjacent facets a 10 nm thick Au layer. Figure 1d shows a cross-sectional transmission electron microscopy (TEM) micrograph of the resulting metal-semiconductor structure while the complete layer structure is schematically presented in Fig. 1e.

In the optical experiments, the Au-coated NWs are excited by a 640 nm diode laser operating in continuous wave. The NWs were tilted by an angle θ in the xz-plane with respect to the optical axis represented by the wave

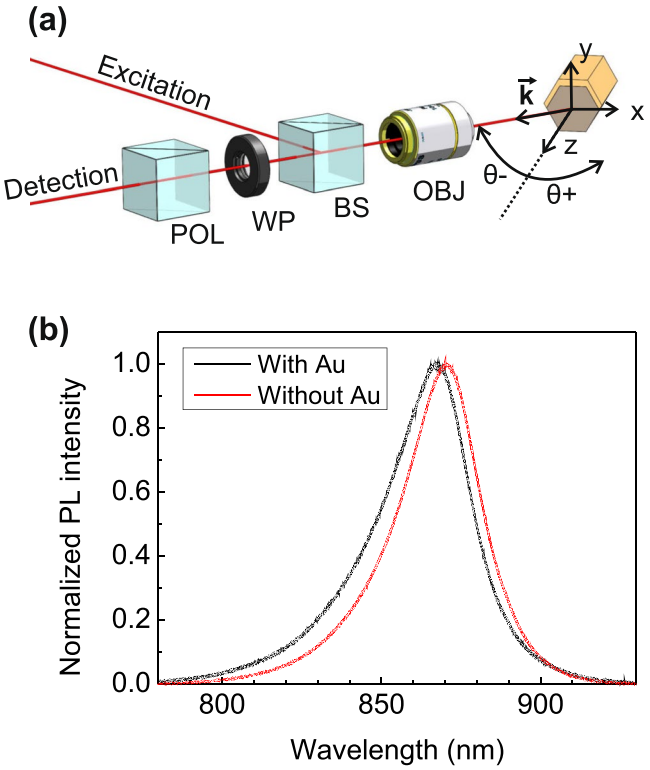

Figure 2. (**a**) Polarized detection set-up: NWs are tilted in *xz*-plane by angle θ with respect to the detection line consisting of a microscope objective (OBJ), a rotating quarter-wave plate (WP), a fixed linear polarizer (POL), and a detection part which includes a spectrometer and a CCD camera. (**b**) Unpolarized photoluminescence spectra for NWs with and without Au at $\theta = 0°$.

vector **k**, as shown in Fig. 2a. The emitted light was collected from the far field with a 10X magnifying objective ($NA = 0.22$). The circular polarization of the photoluminescence (PL) emission was resolved using a rotating broadband quarter-wave plate and a fixed linear polarizer. The PL signal was dispersed with a 750 mm spectrograph equipped with a 1200 l/mm grating and detected with a TE-cooled CCD array. A detailed description of the experimental setup is presented in Supplementary Fig. S2. All measurements were carried out at room temperature. Both the as-grown and Au-coated NWs exhibit a typical GaAs band edge PL emission around with a peak at around 870 nm, as shown in Fig. 2b. A slight blueshift is observed in the presence of Au, most likely due to effect of Au on band bending[42] and consequent change of PL transition energy. In the following we will focus on the polarization properties of the light emitted at 868 nm. It should be noted that, while use of circular polarized excitation affects the absorption efficiency of the asymmetrically Au-coated NWs[38] and thus influence the generation rate of the photoexcited electron-hole pairs, it does not affect the extrinsic chirality of the PL emission, as shown in the Supplementary Fig. S3. Therefore, the optical experiments discussed in this work were carried out using linear polarized excitation.

Experimental Results

An achiral nanostructure can exhibit chiral optical response if the light wave vector **k**, the vector pointing in the direction of anisotropy of the structure, and the surface normal of the sample do not lie in the same plane[7,12]. This phenomenon is called extrinsic chirality, because the breaking of mirror symmetry is not an intrinsic property of the material, but a property of the experiment and the sample together. In the Au-coated NW samples, the extrinsic chiral behavior can observed given a proper orientation of the NW and its Au-coated sides with respect to the light to be absorbed or emitted: the average anisotropy of the structure is in the *y*-direction, the NW axis (the surface normal) is in the *z*-direction, while the wave-vector of the emitted light lies in *xz*-plane in such way that **k** is not parallel with the *z*-axis. In the actual experiment we tilt the sample stage in such way that it equals to rotation of nanowire axis around the *y*-axis in the geometry presented in Fig. 2a. The amount rotation is measured by the angle θ with respect to the k direction. The quarter-wave plate then scans the polarization, with 45° representing right-handed and 135° left-handed circular polarization.

In Fig. 3 we present polar plots of the detected PL intensity as a function of the wave plate angle. As shown in Fig. 3a, the NWs without Au do not show any difference between the left and right-handed polarizations, as expected from the lack of anisotropy between the *x* and *y*-directions. The sample with Au shows a clear left-handed polarization with an intense lobe at 135° and significantly smaller intensity at 45° for $\theta = 30°$, and the polarization changes to right-handed when the sample is rotated to $\theta = -30°$. It should be noted that PL intensity includes a linear polarized contribution that is summed in the circular polarized signal, and therefore

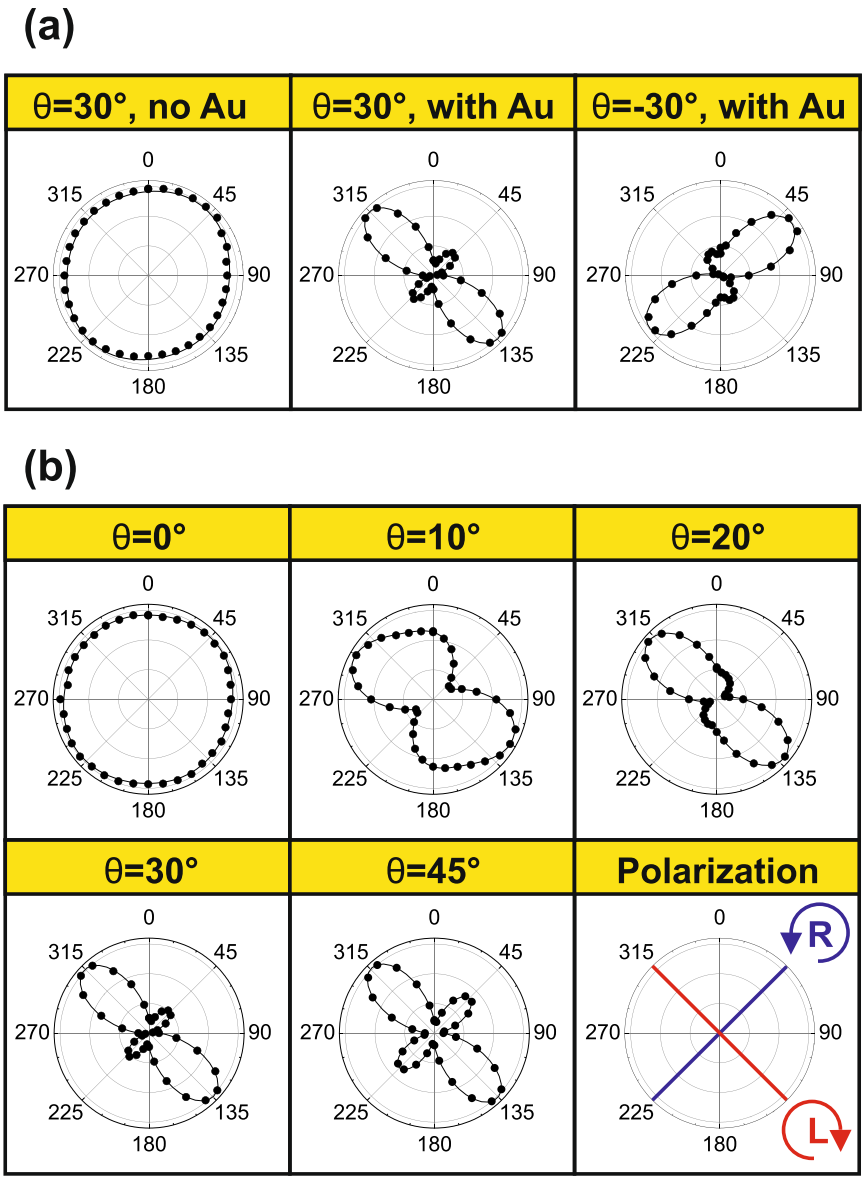

Figure 3. Chirality of photoluminescence emission with polarized detection presented as polar plots of normalized intensity versus $\lambda/4$ waveplate angle: (**a**) for NWs without Au and for NWs with Au for positive and negative tilt angles (θ). (**b**) Different tilt angles for NWs with Au. The dots represent experimental data and the continuous lines are double sinusoidal fits. The radial scale in each plot ranges from 0.7 to 1.02. The last panel in (**b**) presents the WP angles corresponding the right-handed (R) and left-handed (L) polarizations.

polar plots in Fig. 3a exhibit some degree of ellipticity. Nevertheless, these observations clearly manifest extrinsic chiral behavior[10]. Next, we investigate the influence of the tilt angle θ on the polarization of the Au-coated NWs (Fig. 3b). In case of $\theta = 0°$, all three vectors discussed before lie in the same plane, and therefore we do not observe the extrinsic chirality. For tilt angles $\theta > 0$ we observe left-handed polarization which increases as a function of θ, reaches maximum at 20°, and then decreases again at larger tilt angles. The extrinsic chirality in this system is therefore detected as a difference in circular polarization of the PL emission for different emission angles in the far field hemisphere, meaning that the Au layer can control the direction and the handedness of the emission from GaAs core. The degree of polarization and its dependence on the tilt angle θ will be discussed on a more quantitative level in the following as we introduce a theoretical model for PL emission from the Au-coated NWs.

Model

The coupling of emitted light to the NW modes and its influence on CD was investigated using two numerical packages from Lumerical[43]. First, we use MODE solver to calculate complex refractive indices and field profiles of the guided modes supported in the PL peak wavelength (see Supplementary Info for the details). The NWs investigated in this work have an average diameter of 197 nm and they support the fundamental HE_{11}-like mode at emission wavelength of 868 nm. Au strongly breaks the degeneracy of this mode between the x and y-directions,

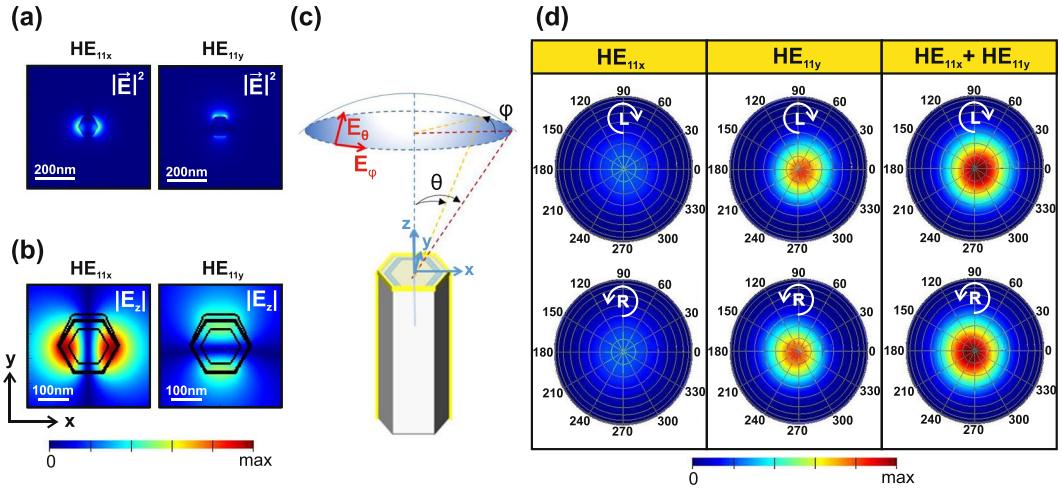

Figure 4. Electric field intensities (**a**) $|\mathbf{E}|^2$ and (**b**) $|\mathbf{E_z}|$ for HE_{11x} and HE_{11y} modes supported at 868 nm. (**c**) Illustration of the far field simulation geometry. (**d**) Simulated left-handed (L) and right-handed (R) polarizations of the far field intensities emitted from HE_{11x} and HE_{11y} modes. The tilt axis θ in (**d**) ranges from 0° to 90° with 10° steps while the azimuthal axis φ presents a full rotation around the NW axis.

leading to a significant difference between properties of the HE_{11x} and HE_{11y} modes, as show in Fig. S7 and in Supplementary Information. The density of the investigated NWs is $1 \times 10^8\,cm^{-2}$ and they have average nearest neighbor distance of 500 nm (Supplementary Fig. S6). In ref.[30] we investigated the resonant absorption properties of similar NWs without Au and showed that the NW ensemble exhibits modal properties governed by single NW dimensions, which can be accurately described by the statistical average values due to the NW size uniformity. It should also be noted that mode spreading is less pronounced in Au-coated than in bare NWs (Supplementary Fig. S7). Consequently, as shown in Fig. 4a, the HE modes that are weakly guided on the NW borders have spatial spreading to at most 180 nm from the center of the NW, which is significantly less than the nearest neighbor distance. Therefore, we can exclude the interaction between the NW neighbors in the following analysis. In Fig. 4b the E_z component along the polarization direction for HE_{11y} mode is higher in the vicinity of Au and asymmetric in the core, which provides the asymmetry required for extrinsic chirality.

Next, we use the finite 3D Finite Difference Time Domain (FDTD) solver to monitor the far field from the NW excited by the HE_{11x} and HE_{11y} modes at 868 nm. The polarization of the emission in a specific angle in the far field can be resolved by taking complex tangential components E_φ and E_θ, and multiplying them by Jones transfer matrices of the quarter-wave plate with rotation angles corresponding to the left and right-handed polarizations, and the linear polarizer, thus mimicking the experiment. In Fig. 4c the far field angles (θ,$\varphi = 0°$) and (θ,$\varphi = 180°$) correspond to the experimental tilting of θ and $-\theta$, respectively, as φ represents rotation around the NW axis. The emission from finite NWs is governed by the coupling of the emission centers to the modes, and it is usually investigated by placing a single dipole source inside the NW[28,34] and calculating the far field contribution of that simulation. For intrinsically isotropic systems, such as zincblende (ZB) one needs to superpose results from simulations with three dipole orientations[44]. This would be the case also with the ZB NWs investigated in this work, where the transitions produce both radially and axially polarized intensity, as proved by the linear PL measurements (Supplementary Fig. S5). Moreover, one would need to perform several simulations to average the contributions from a large number dipole positions across the NW volume to the far field polarization. This is required because of the different spacing of the antinodes of the HE_{11x} and HE_{11y} modes along z-direction due to their different λ_z, and the asymmetry of the field components in xy-cross-section. As the Au layer makes such averaging complicated and time-consuming, here we show that the mode solver and FDTD can be used in consecutively to model the extrinsic chirality of PL from the Au-coated NWs by performing only two simulations. Namely, the two modal fields, which contain complete complex electromagnetic field information in the NW xy-cross-section, are first calculated with the mode solver, and then imported as sources that excite the NW in FDTD solver. The intensity is then calculated for the specific quarter-wave plate angle at each point in the far field (see more details in Supplementary Information). As show in Fig. 4d, the results from the excitation with HE_{11x} mode show less intensity with respect to HE_{11y}, which is in agreement with its higher losses. Moreover, HE_{11x} mode does not contribute to CD (Supplementary Fig. S8). However, HE_{11y} has a significant difference between the left and right-handed intensities at oblique angles. The final result for the left and right-handed intensities is obtained by summing the contribution from both modes. Again, we see a clear difference between the left and right-handed intensities at oblique angles for the sum of the HE_{11x} and HE_{11y} modes, but it should be stressed that it arises solely from the HE_{11y} asymmetry. It should also be noted that these modes almost degenerate in the case of a bare NW, and therefore no circular polarization is observed for the NWs without Au (Supplementary Fig. S9).

We can further introduce a figure of merit for CD in the emission:

$$CD[\%] = \frac{I_L - I_R}{I_L + I_R} \cdot 100, \tag{1}$$

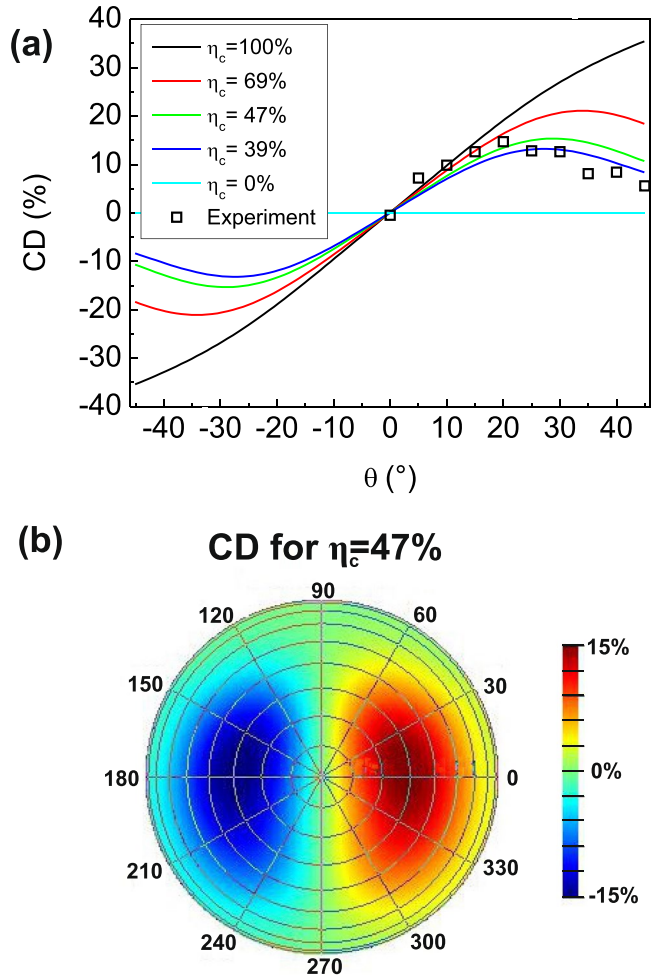

Figure 5. (**a**) The dependence of CD on tilt angle θ. The result of the far field model is fitted to the experimental data by introducing a coupling efficiency factor η_c as a fitting parameter. (**b**) Far field CD map $\eta_c = 47\%$, which produces the best fit. The tilt axis θ in (**b**) ranges from 0° to 90° with 10° steps.

where I_R and I_L are the left and right-handed intensities measured at the quarter-wave plate angles of 45° and 135°, respectively. These intensities contain contributions from both modes, and from the unpolarized, isotropic background that can be modelled with a Lambertian source[35] representing the uncoupled part PL emission, the contribution of which effectively lowers CD (see the complete definition of CD in Supplementary Information). We use the intensity of the Lambertian source as the only fitting parameter and present the results for different values of the coupling efficiency of the NW emission to HE_{11} modes defined as:

$$\eta_c = \frac{I_{HE11x} + I_{HE11y}}{I_{HE11x} + I_{HE11y} + I_{Lambert}}, \tag{2}$$

where I_{HE11x}, I_{HE11y} and $I_{Lambert}$ represent the total power emitted to the upper half-space by HE_{11x}, and HE_{11y} sources exciting the NW, and uncoupled intensity modelled with the Lambertian source, respectively. In Fig. 5a we show CD as a function of tilt angle θ for different values of η_c at $\varphi = 0°$. As expected, strong coupling leads to the increase of CD due to the high contribution of HE_{11y} to chirality. Lower coupling follows the experimentally measured CD, with $\eta_c = 47\%$ giving the best fit which reproduces the experimentally observed maximum CD of 15%. In Fig. 5b the far field CD for this coupling proves the concept of extrinsic chirality: it is equal to 0 for all θ at $\varphi = 90°$ and $\varphi = 270°$, as no breaking of symmetry takes place in such configuration, and it inverts the sign with the inversion of θ where CD exists. The presented model also provides means for further optimization for obtaining stronger polarization. Even larger values of CD could be achieved by (i) increasing the symmetry breaking between the x and y-directions, (ii), enhancing the coupling of the PL emission to the modes (e.g. by making the NW core thicker to increase the mode overlap with the emitting region), or (iii) confining the emitting material in the form of quantum dots[25] or superlattices[45] at the particular positions that lead to stronger CD (e.g. in the antinode of the HE_{11y}, as shown in Supplementary Information).

Conclusions

In summary, we have demonstrated extrinsic chirality of PL emission from asymmetrically Au-coated GaAs-AlGaAs-GaAs core-shell NWs fabricated using a completely lithography-free self-assembled technique. Splitting of left and right-handed polarizations in different directions in the far field was measured by circular polarization dependent detection for different sample tilt angles. The maximum value of CD = 15% was obtained at 20° tilt. The chiral luminescence from the semiconductor-metal hybrid system was modelled using a new approach based on solving the HE_{11} modes supported at the GaAs emission wavelength, and consecutively, using the modes as sources in FDTD simulation of the polarization response in the far field. From this theoretical investigation, we found out that the extrinsic chiral response of the investigated structure arises from the HE_{11y} mode due to the symmetry breaking provided by the metal. Furthermore, it was shown that 47% of the PL emission couples in the HE_{11} modes, while even higher values of CD could be achieved by further enhancing the coupling efficiency or by increasing the symmetry breaking. From the application point of view, a major benefit of using III-V semiconductor NWs as the light emitting material is that they can incorporate radial PN-junctions and thus provide means for the fabrication of chiral LEDs integrated on Si platform. We believe that these results pave way for compact and integrated chiral light sources, which have a broad range of applications quantum technology, biology, and chemistry.

Data Availability

The datasets generated during and/or analysed during the current study are available from the corresponding author on reasonable request.

References

1. Kelvin, L. The Molecular Tactics of a Crystal. (Clarendon Press, Oxford, 1894).
2. Quidant, R. & Kreuzer, M. Biosensing: plasmons offer a helping hand. *Nature Nanotechnology* **5**, 762 (2010).
3. Taniguchi, T. & Nakanishi, K. Circular Dichroism (CD) for Natural Products. In book *Wiley Encyclopedia of Chemical Biology*, https://doi.org/10.1002/9780470048672.wecb091 (John Wiley & Sons, Inc, 2008).
4. Wang, X. & Tang, Z. Circular Dichroism Studies on Plasmonic Nanostructures. *Small* **13**, 1601115 (2017).
5. Valev, V. K. *et al.* Plasmonic ratchet wheels: switching circular dichroism by arranging chiral nanostructures. *Nano Lett.* **9**, 3945 (2009).
6. Esposito, M. *et al.* Three dimensional chiral metamaterial nanospirals in the visible range by vertically compensated focused ion beam induced-deposition. *Adv. Opt. Mat.* **2**, 154 (2014).
7. Belardini, A. *et al.* Chiral light intrinsically couples to extrinsic/pseudo-chiral metasurfaces made of tilted gold nanowires. *Sci. Rep.* **6**, 31796 (2016).
8. De Leon, I. *et al.* Strong, spectrally-tunable chirality in diffractive metasurfaces. *Sci. Rep.* **5**, 13034 (2015).
9. Cao, T., Wei, C., Mao, L. & Li, Y. Extrinsic 2D chirality: giant circular conversion dichroism from a metal-dielectric-metal square array. *Sci. Rep.* **4**, 7442 (2014).
10. Verbiest, T., Kauranen, M., Van Rompaey, Y. & Persoons, A. Optical activity of anisotropic achiral surfaces. *Phys. Rev. Lett.* **77**, 1456 (1996).
11. Plum, E. *et al.* Metamaterials: Optical Activity without Chirality. *Phys. Rev. Lett.* **102**, 113902 (2009).
12. Belardini, A. *et al.* Circular dichroism in the optical second-harmonic emission of curved gold metal nanowires. *Phys. Rev. Lett.* **107**, 257401 (2011).
13. Riehl, J. P. & Richardson, F. S. Circularly polarized luminescence spectroscopy. *Chem. Rev.* **1**, 86 (1986).
14. Sanchez-Carnerero, E. M. *et al.* Circularly polarized luminescence from simple organic molecules. *Chem.–Eur. J.* **21**, 13488 (2015).
15. Dyakonov, M. I. (Ed.) Spin Physics in Semiconductors ISBN 978-3-319-65435-5 (Springer, 2017).
16. Yokoyama, A., Yoshida, M., Ishii, A. & Kato, Y. K. Giant Circular Dichroism in Individual Carbon Nanotubes Induced by Extrinsic Chirality. *Phys. Rev. X* **4**, 011005 (2014).
17. Yan, C., Wang, X., Raziman, T. V. & Martin, O. J. F. Twisting fluorescence through extrinsic chiral antennas. *Nano Lett.* **17**, 2265 (2017).
18. Mårtensson, T. Epitaxial III− V nanowires on silicon. *Nano Lett.* **4**, 1987 (2004).
19. Bakkers, E. P. A. M. *et al.* Epitaxial growth of InP nanowires on germanium. *Nature Mater.* **3**, 769 (2004).
20. Morral, A. F. Gold-free GaAs nanowire synthesis and optical properties. *J. Sel. Topics Quantum Electron.* **17**, 819 (2011).
21. Wagner, R. S. & Ellis, W. C. Vapor-Liquid-Solid Mechanism of Single Crystal Growth. *Appl. Phys. Lett.* **4**, 89 (1964).
22. Yan, R. X., Gargas, D. & Yang, P. D. Nanowire photonics. *Nat. Photonics* **3**, 569 (2009).
23. Aberg, I. *et al.* A GaAs Nanowire Array Solar Cell With 15.3% Efficiency at 1 Sun. *IEEE J. Photovolt.* **6**, 185 (2016).
24. LaPierre, R. R., Robson, M., Azizur-Rahman, K. M. & Kuyanov, P. A review of III–V nanowire infrared photodetectors and sensors. *J. Phys. D: Appl. Phys.* **50**, 123001 (2017).
25. Zadeh, I. E. *et al.* On-chip single photon filtering and multiplexing in hybrid quantum photonic circuits. *Nano Lett.* **16**, 2289 (2016).
26. Mayer, B. *et al.* Monolithically integrated high-β nanowire lasers on silicon. *Nano Lett.* **16**, 152 (2016).
27. Fountaine, K., Whitney, W. & Atwater, H. Resonant absorption in semiconductor nanowires and nanowire arrays: Relating leaky waveguide modes to Bloch photonic crystal modes. *J. Appl. Phys.* **116**, 153106 (2014).
28. Abujetas, D. R., Paniagua-Domíguez, R. & Sanchez-Gil, J. A. Unraveling the janus role of mie resonances and leaky/guided modes in semiconductor nanowire absorption for enhanced light harvesting. *ACS Photonics* **2**, 921 (2015).
29. Anttu, N. & Xu, H. Coupling of Light into Nanowire Arrays and Subsequent Absorption. *J. Nanoscience and Nanotechnology* **10**, 7183 (2010).
30. Leahu, G. *et al.* Photo-acoustic spectroscopy revealing resonant absorption of self-assembled GaAs-based nanowires. *Sci Rep.* **7**, 2833 (2017).
31. Bulgarini, G. *et al.* Nanowire waveguides launching single photons in a Gaussian mode for ideal fiber coupling. *Nano Lett.* **14**, 4102 (2014).
32. Kivisaari, P., Chen, Y. & Anttu, N. Emission enhancement, light extraction and carrier dynamics in InGaAs/GaAs nanowire arrays. *Nano Futures* **2**, 15001 (2018).
33. Henneghien, J. A., Gayral, B., Désieres, Y. & Gérard, J. M. Simulation of waveguiding and emitting properties of semiconductor nanowires with hexagonal or circular sections. *J. Opt. Soc. Am. B* **26**, 2396 (2009).
34. Paniagua-Domínguez, R., Grzela, G., Rivas, J. G. & Sánchez-Gil, J. A. Enhanced and directional emission of semiconductor nanowires tailored through leaky/guided modes. *Nanoscale* **5**, 10582 (2013).
35. van Dam, D. *et al.* Directional and Polarized Emission from Nanowire Arrays". *Nano Lett.* **15**, 4557 (2015).
36. Mayer, B. *et al.* Lasing from individual GaAs-AlGaAs core-shell nanowires up to room temperature. *Nat Commun.* **4**, 2931 (2013).
37. Saxena, D. *et al. Nature Photonics* **7**, 963 (2013),

38. Leahu, G. *et al*. Evidence of optical circular dichroism in GaAs-based nanowires partially covered with gold. *Adv. Opt. Mater.* **5**, 1601063 (2017).
39. Hakkarainen, T. V., Schramm, A., Mäkelä, J., Laukkanen, P. & Guina, M. Lithography-free oxide patterns as templates for self-catalyzed growth of highly uniform GaAs nanowires on Si(111). *Nanotechnology* **26**, 275301, (2015).
40. Koivusalo, E., Hakkarainen, T., Guina, M. & Dubrovskii, V. G. Sub-Poissonian narrowing of length distributions realized in Ga-catalyzed GaAs nanowires. *Nano Lett.* **17**, 5350 (2017).
41. Koivusalo, E., Hakkarainen, T. & Guina, M. Structural Investigation of Uniform Ensembles of Self-Catalyzed GaAs Nanowires Fabricated by a Lithography-Free Technique. *Nanoscale Res. Lett.* **12**, 192 (2017).
42. Songmuang, R. *et al*. Determination of the Optimal Shell Thickness for Self-Catalyzed GaAs/AlGaAs Core–Shell Nanowires on Silicon. *Nano Lett.* **16**, 3426 (2016).
43. Lumerical Solutions, Inc, http://www.lumerical.com/tcad-products/fdtd/.
44. Wilhelm, C., Larrue, A., Dai, X., Migas, D. & Soci, C. Anisotropic photonic properties of III–V nanowires in the zinc-blende and wurtzite phase. *Nanoscale* **4**, 1446 (2012).
45. Ren, D. *et al*. Single-Mode Near-Infrared Lasing in a GaAsSb-Based Nanowire Superlattice at Room Temperature. *Nano Lett.* **18**, 2304 (2018).

Acknowledgements

This work made use of Aalto University Nanomicroscopy Center (Aalto-NMC) facilities. T.H. acknowledges financial support from the Academy of Finland Project NESP (decision number 294630) and NanoLight (decision number 310985). E.P. acknowledges mobility support from the Nanoscale Quantum Optics Cost Action MP1403. The authors would like to thank A. Belardini and F.A. Bovino for discussions and valuable insight on the extrinsic chirality of photoluminescence.

Author Contributions

T.H. fabricated the semiconductor nanowires, carried out the optical experiments, and took main responsibility of writing the manuscript. E.P. and C.S. invented the methodology for optical simulations and carried out the simulations. M.R.P. designed the asymmetric Au-layers, optimized the Au deposition, and deposited Au on the samples investigated in the manuscript. All authors contributed to the preparation of the manuscript.

Additional Information

Supplementary information accompanies this paper at https://doi.org/10.1038/s41598-019-41615-1.

Competing Interests: The authors declare no competing interests.

Publisher's note: Springer Nature remains neutral with regard to jurisdictional claims in published maps and institutional affiliations.

Supplementary Information

Demonstration of extrinsic chirality of photoluminescence with semiconductor-metal hybrid nanowires

Teemu Hakkarainen[1,], Emilija Petronijevic[2], Marcelo Rizzo Piton[1,3], and Concita Sibilia[2]*

[1]Optoelecronics Research Centre, Physics Unit, Tampere University, Korkeakoulunkatu 3, FI-33720 Tampere, Finland

[2]Department S.B.A.I., Sapienza Università di Roma, Via A. Scarpa 14, I-00161 Rome, Italy

[3]Departamento de Física, Universidade Federal de São Carlos, CP 676 São Carlos, São Paulo, Brazil

*E-mail: teemu.hakkarainen@tuni.fi

1. Au-coated nanowires

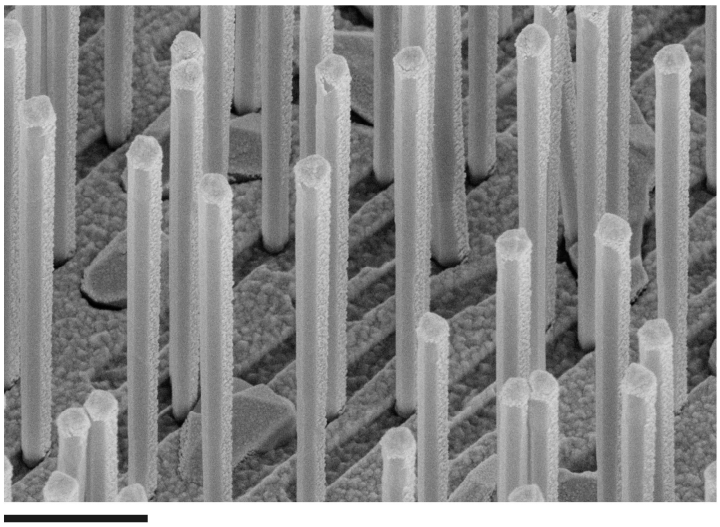

Figure S1. SEM picture showing the nanowires after the growth of the asymmetric Au-coating. The scale bar is 1 μm.

2. Experimental setup

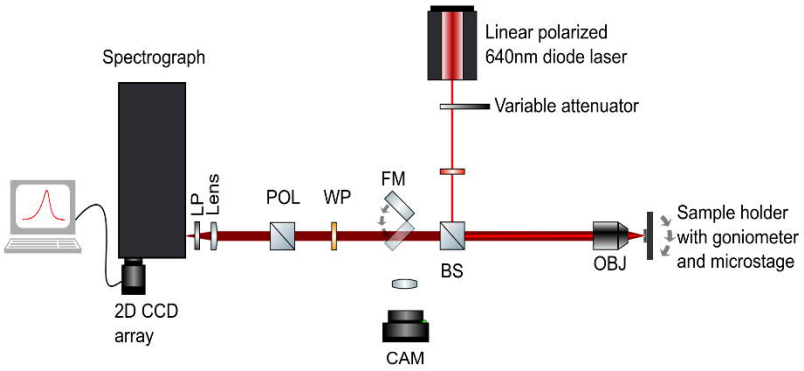

WP = Rotating broadband λ/4 waveplate
POL = Broadband cube polarizer
BS = Broadband non-polarizing beam splitter
OBJ = 10x magnifying microscope objective, NA 0.25
LP = 700nm longpass filter
FM = Flip mirror
CAM = Microscope camera equipped with a diffraction limited tube lens

Figure S2. Illustration of the experimental setup for circular polarized photoluminescence experiments.

3. Effect of circular polarized excitation

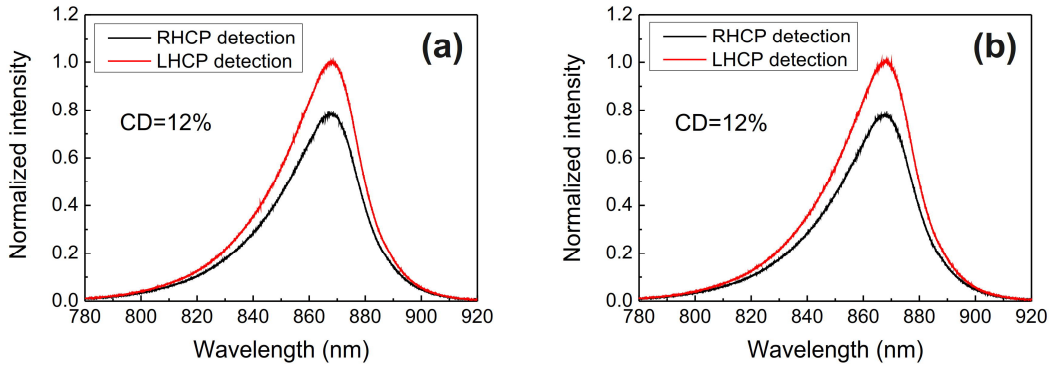

Figure S3. Effect of circular polarized excitation at 640 nm on the CD of photoluminescence emission: (a) with right-handed circular polarized (RHCP) excitation and (b) with left-handed circular polarized (LHCP) excitation, both showing CD=12% for tilt angle of 30°.

4. Linear polarization of the photoluminescence emission

A. Polarization anisotropy in the x-y plane

The linear polarization response of the photoluminescence (PL) emission for both Au-coated and Au-free NWs was measured using the experimental setup presented in Fi. S1. A broadband $\lambda/2$ waveplate was used for probing the linear polarization. The NWs were excited with a 20x microscope objective, which was used also for collecting the PL signal.

As, show in Fig. S4a, the NWs with Au show some degree of linear polarization in the direction of the Au deposition. Qualitatively, it can be expressed as the degree of linear polarization (*DOP*):

$$DOP = \frac{I_y - I_x}{I_y + I_x} \times 100\% = 5.1\% , \quad \text{(S1)}$$

Where I_y and I_x are the intensities for polarizations parallel and perpendicular to the Au deposition direction, respectively. The NWs without Au do not exhibit any polarization anisotropy, as shown in Fig. S4b, as expected from the crystal symmetry of zincblende (111) direction. The slight polarization of the Au-coated NWs can be attributed to the influence of Au on the local optical density of states.

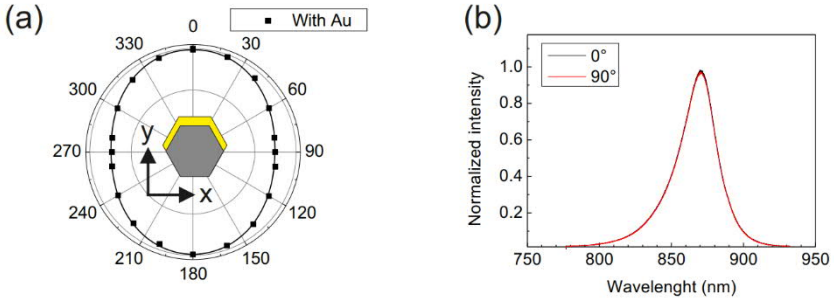

Figure S4. Linear polarization of NWs with and without Au measured in the direction parallel to the surface normal of the substrate. (a) Polar plot of normalized intensity with respect to polarization angle at GaAs peak wavelength for Au-coated NWs. The radial scale ranges from 0.5 to 1.02. The orientation of the structure is shown in the inset. (b) Linear polarized PL spectra for NWs without Au. The measurement was performed using the setup shown in Fig. S2 with a λ/2 waveplate and 10x magnifying microscope objective.

B. Polarization anisotropy: axial vs. radial

The polarization anisotropy between the axial and radial directions was measured using the experimental setup presented in Fig. S2. A broadband λ/2 waveplate was used for probing the linear polarization. A single NW transferred on a SiO_2 substrate was excited with a 40x microscope objective, which was used also for collecting the PL signal. An additional cylinder lens was place in the excitation beam path (in between the variable attenuator and beam splitter) in order to expand the excitation spot as a line which excited the whole volume of the NW. The NW was aligned in such way the emission from the whole NW was detected with the TE-cooled CCD camera.

As shown in Fig. S5, the NWs with and without Au show similar polarization along the NW axis. Qualitatively it can be expressed as the degree of linear polarization (*DOP*):

$$DOP = \frac{I_a - I_r}{I_a + I_r} \times 100\% = 23.5\% , \quad \text{(S2)}$$

Where I_a and I_r are the intensities of the polarizations in the axial and radial directions, respectively. Such linear polarization is typical for (111)-oriented zincblende NWs due to the crystalline symmetry and dielectric anisotropy arising from the 1-dimensional geometry of the structure[1]. We can conclude that the Au layer does not significantly alter the emission dipole orientation in the NW.

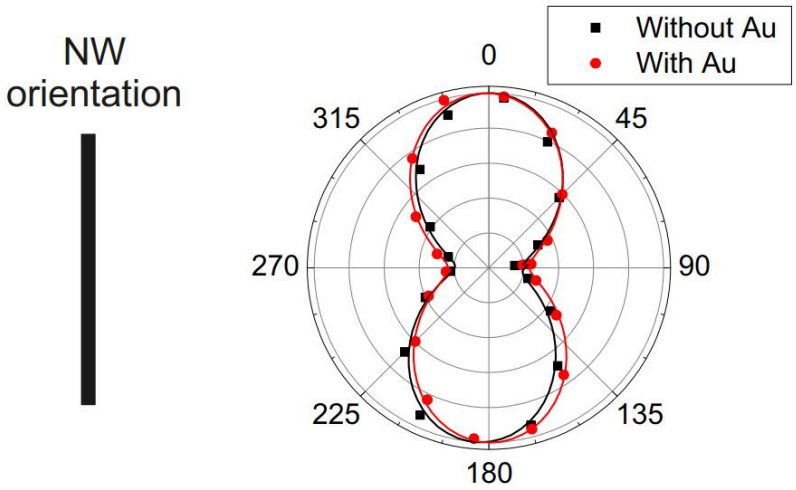

Figure S5. Linear polarization of a single NW with and without Au presented as polar plots of normalized intensity versus polarization angle at GaAs peak wavelength. The radial scale in each plot ranges from 0.5 to 1.02. The NWs were transferred on a SiO2 substrate and the measurement was performed in the direction normal to the NW sidefacet using the setup shown in Figure S1 with a λ/2 waveplate and a 40x magnifying microscope objective.

5. Nanowire density and nearest neighbor distribution

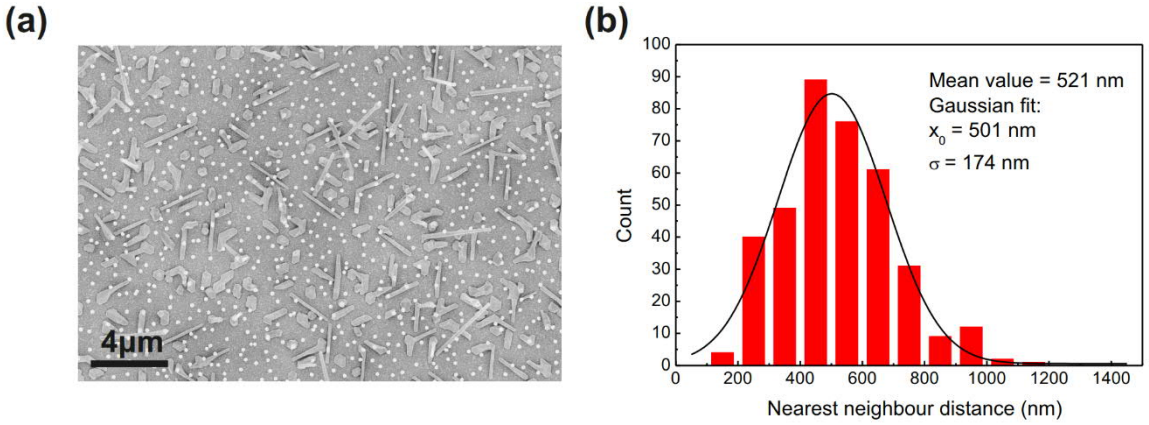

Figure S6. (a) Top-view scanning electron microscope (SEM) image of the NWs having density of $1x10^8$ cm-2. (b) Nearest neighbor distance statistics for the NWs in (a). The histogram includes the mean value of the data as well as the center (x_0) and standard deviation (σ) of the Gaussian fitting function.

6. Details on the simulation

Emission from finite NWs is governed by the coupling of the emission centers to the guided or leaky modes of the nanostructure, and it has been investigated both theoretically[2] and experimentally[3] for semiconductor NWs. We recently studied absorption properties of GaAs-based NW samples that were covered by Au by a similar process[4]: photo-acoustic spectroscopy showed that such samples still exhibit absorption resonances due to the semiconductor mode excitation, although they were much broader due to the asymmetric presence of Au. On the other hand, Au influences the confinement of the electric field, that directly governs the local density of states and hence PL. Therefore, in such structures the far field polarization and intensity of PL modelled by the dipoles is expected to highly depend on the dipole orientation and position with respect to the modal field [2].

We first use MODE solver by Lumerical to calculate the modes of infinitely long NWs, using statistically determined average values for NW dimensions, and to compare modal fields with and without the presence of Au. This tool uses the finite-difference eigenmode method to solve Maxwell's equations on a cross-sectional mesh of the waveguide, giving the effective index as an eigenvalue, and mode profile as an eigenvector. In both *x* and *y* direction the used mesh was 1 nm. Lower diameter GaAs NWs at wavelengths around 870 nm support only no-cutoff modes HE_{11x} and HE_{11y}, that are weakly guided, with the electric field confined on the borders. For the case without Au in Fig. S7a, these modes are almost degenerate with n_{HE11x}=1.557. Au layer strongly breaks the degeneracy, giving two distinct modes with n_{HE11x}=1.249+0.009i and n_{HE11y}=1.073+0.006i, with mode propagation wavelengths $\lambda_{z,HE11x}$=695nm, and $\lambda_{z,HE11y}$=809nm. Since the modes are not completely confined inside the NW (Fig. S7b), perfectly matched layers must be used for the simulation boundaries in *x* and *y* direction. Clearly, the Au layer leads to even lower confinement (the same color scale is used), and breaks the symmetry in y-direction, as can be seen especially from E_z component which is much stronger closer to Au layer. Moreover, the Au layer introduces propagation losses, as can be seen e.g. from 3D electric field intensity distribution in the NW excited with *y*-polarized field at the normal incidence, from the top. Note that for the modelling of the emission one should only consider emission from GaAs core, which effectively has a side of 65.3 nm; in Fig. S7c the electric field confinement in GaAs core follows the symmetry of the mode. Next, PL from a finite NW is modelled using Finite Difference Time Domain Solver by Lumerical. The NW and the source at 868nm are surrounded in all directions by perfect matching layers, placed at least half the wavelength from the borders of the NW to prevent from the instabilities due to the evanescent fields. A near field profile monitor placed 50nm above the NW projects the electric field components at 1 m far-field hemisphere. In order to model the experiment, these complex far fields at different angles (θ,φ) are saved as matrix, and multiplied by the Jones matrices of the lambda quarter plate and linear polarizer (Figure S7d). The matrices depend on the quarter wave plate rotation such that quarter the rotation of 45° (135°) represents right (left) handed polarization (R and L, respectively). Far-field angle θ corresponds to the tilting angle of the sample, and the azimuthal angle φ in the experiments takes values of 0 and 180° (note that φ=180° means that the sample is tilted in the negative θ direction, as in Fig. 3a in the manuscript).

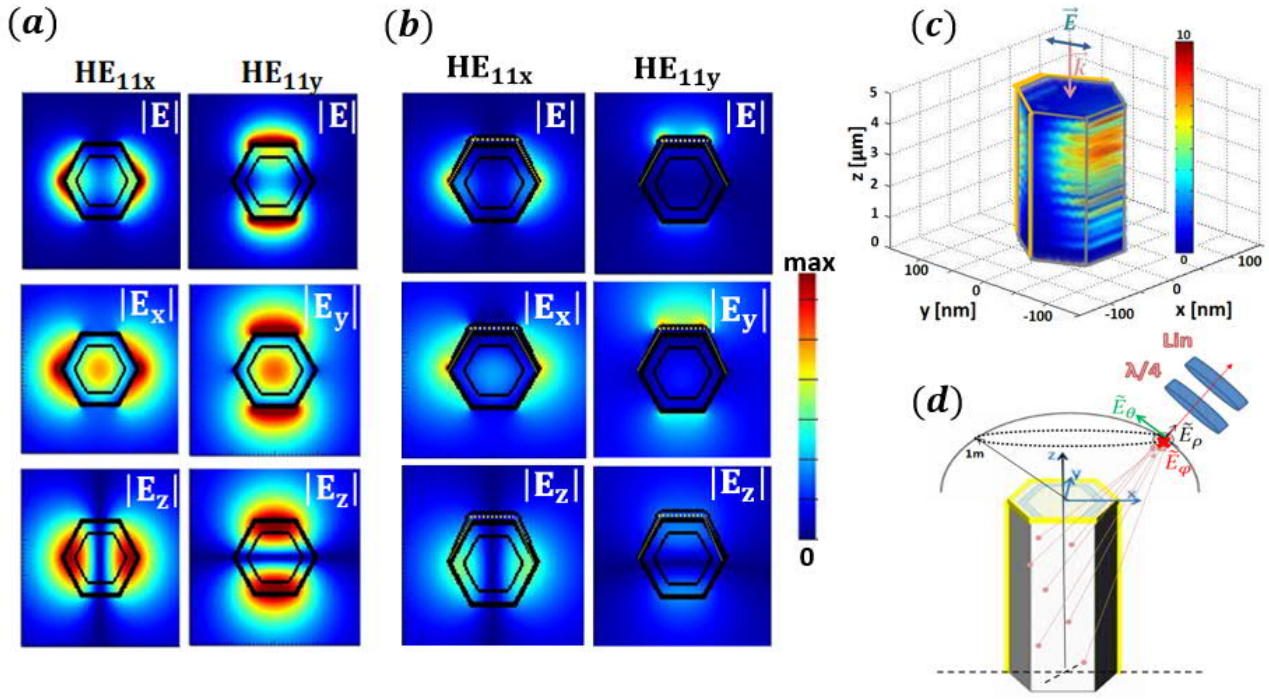

Figure S7. Electric field distribution for HE_{11x} and HE_{11y} modes for (a) the NW without Au, (b) the NW with Au. (c) 3D distribution of electric field intensity in the GaAs core. (d) Sketch of the simulation set-up with the far-field hemisphere.

Conventionally, the source of PL in the NW is modelled by placing a single point electric dipole as a radiation source at a position (*x*,*y*,*z*) inside GaAs core, and averaging the simulations over the dipole position and orientation. In Fig. S8 we show the integrated far field intensity across the whole hemisphere above the NW, as a dependence on the NW length. We see that *x*-oriented dipole has shorter oscillation wavelength than *y*-oriented dipole, in agreement with $\lambda_{HE11x} < \lambda_{HE11y}$. Further, more power give *z*-oriented, off-centered dipoles as they see stronger fields in *z*-direction; moreover, E_z is stronger closer to Au, that is why *z* dipole at (*x*=0nm, *y*=40nm) radiates more than at (*x*=0nm, *y*=-40nm). Finally, oscillations are longer for the *z*-oriented dipole when placed at (x=0nm, *y*=±40nm), than at (*x*=40nm, *y*=0nm); the first are similar to the ones of y-dipole (coupling to HE_{11y}), and the latter are similar similar to the ones of *x*-dipole (coupling to HE_{11x}). Intensity decreases due to the higher losses for longer NWs. Therefore, coupling to these different modes is highly dependent on the orientation and position of the dipoles in *xy* cross-section. Moreover, as the possible excited modes have longer propagation length than the NW length[2], one must take into account different *z* positions as they lead to the enhancement/decrease in the emission depending on the position of the antinodes/nodes of the modal field. Finally, to resolve their contribution to L or R polarization in the far field, one would need to perform high number of simulations to account for all these properties.

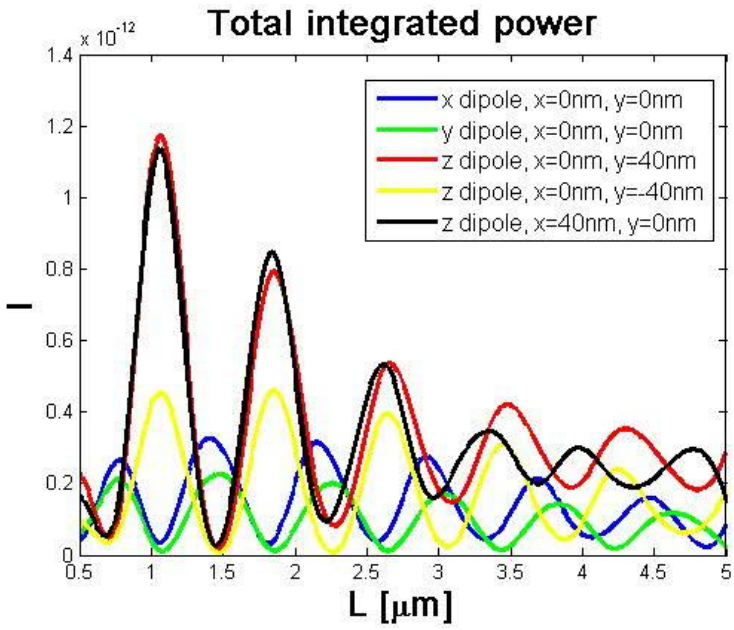

Figure S8. Total integrated far-field intensity as the function of NW length.

In the manuscript, instead, we use the complex modal fields saved from MODE simulations to import them as sources for FDTD simulations. Such fields contain field distributions of all three electric field components across the NW cross section, and propagation properties in *z*-direction. The first simplifies the issue of averaging over different dipole orientations, and the latter simplifies the averaging of the dipole positions in *z*-direction. Therefore, only two simulations are needed to account for the far-field properties when the NW is excited with HE_{11x} or HE_{11y} mode. Without Au, these modes have no losses and lead to similar emission in the far-field, as shown in Fig. S9. By applying the Jones matrices to the complex fields at each point in the far-field, we calculate the contribution to L or R polarization of the mode. As expected, for such symmetric case the difference between L and R cancels out for both modes everywhere at φ=0°, 90°, 180° and 270°, giving small differences in regions between these angles. These differences are of the opposite sign for HE_{11x} and HE_{11y}; as the emission is a result of the coupling to the both modes, we finally consider the intensity emitted to L and R from the both modes. Finally, the difference between L and R for the sum of the modes gives no chiral behavior at all far-field points.

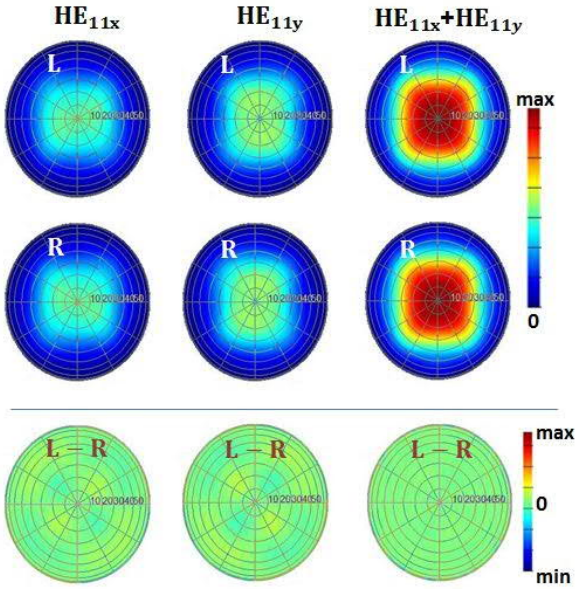

Figure S9. Simulated left-handed (L) and right-handed (R) polarizations of the far-field intensities emitted from HE_{11x} and HE_{11y} modes emitted from the NW without Au. The tilt axis θ in ranges from 0° to 90° with 10° steps while the azimuthal axis φ presents a full rotation around the NW axis.

The modes are strongly affected by the introduction of the asymmetric Au layer: HE_{11x} has higher losses and symmetric electric field intensity in the core, while for HE_{11y} the field is stronger closer to the Au layer. This directly influences the far-field polarization, as shown in Fig. S10. HE_{11x} mode gives lower overall intensity for both L and R polarizations, and their difference shows no chiral behavior for all θ at φ=0°, 90°, 180° and 270°, while there is a negligible chirality elsewhere. HE_{11y} mode has lower losses and gives higher intensity in both polarizations; the difference between these components that leads to CD is anti-symmetric for φ=0° and φ=180°, and 0 for φ=90° and φ=270°, which is characteristic for extrinsic chirality. Finally, the overall intensity of two modes is governed by the asymmetry of HE_{11y} mode, and the difference maximum exactly matches the experimentally observed angle of maximum CD, i.e. θ=20° (φ=0°).

In order to fit experimental CD, we consider contributions from both modes as well as the uncoupled part of the emission that behaves as a Lambertian source:

$$CD = 100 \cdot \frac{(I_{HE_{11x},L} + I_{HE_{11y},L} + I_{Lam}cos\theta) - (I_{HE_{11x},R} + I_{HE_{11y},R} + I_{Lam}cos\theta)}{I_{HE_{11x},L} + I_{HE_{11y},L} + I_{HE_{11x},R} + I_{HE_{11y},R} + 2I_{Lam}cos\theta}, \quad \text{(S3)}$$

where $I_{HE11i,j}$ stands for the intensity emitted from HE_{11i} mode to j polarization, i=(x,y), j=(L,R), and I_{Lam} is the maximum intensity of the Lambertian source. I_{Lam} is used as the only fitting parameter to obtain CD value from the experiment, and calculate the coupling efficiency as explained in the main manuscript.

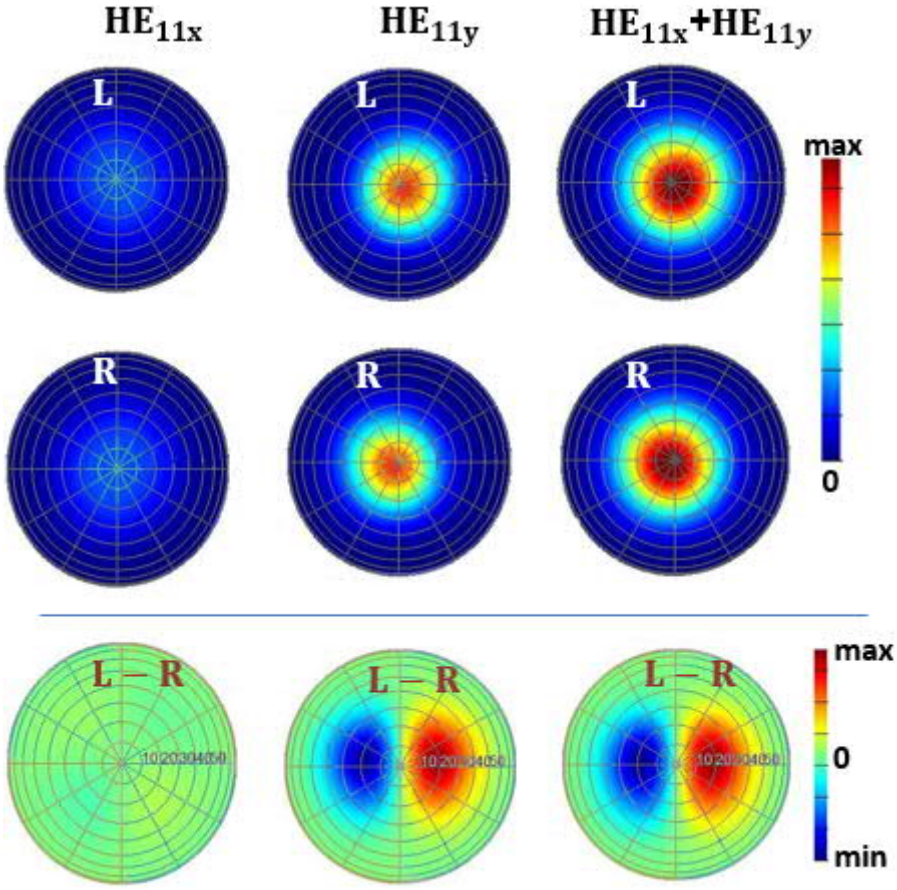

Figure S10. Simulated left-handed (L) and right-handed (R) polarizations of the far-field intensities emitted from HE_{11x} and HE_{11y} modes emitted from the NW with Au. The tilt axis θ ranges from 0° to 90° with 10° steps while the azimuthal axis φ presents a full rotation around the NW axis.

From previous dipole source simulations we noted that single point dipoles can provide higher CD, that is lowered by averaging the contributions from the various dipoles across the volume. In Fig. S11 we show the results averaged over three dipole orientations for dipoles placed in the NW center, that gives three times higher CD at the angle θ=12° (note that high CD on the borders of the graph is due to numerical errors, and should not be considered as there is no intensity emitted at these angles). Therefore, confining the emitters to a small volume can enhance CD and change its angular behavior.

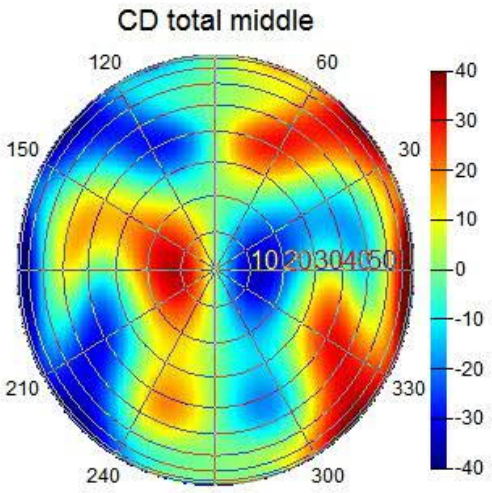

Figure S11. CD of the dipole placed at the NW center and averaged over three directions.

References

1. Wilhelm, C., Larrue, A., Dai, X., Migas, D. & Soci, C. Anisotropic photonic properties of III–V nanowires in the zinc-blende and wurtzite phase. *Nanoscale* **4,** 1446 (2012).

2. Paniagua-Domínguez, R., Grzela, G., Rivas, J. G., & Sánchez-Gil, J. A. Enhanced and directional emission of semiconductor nanowires tailored through leaky/guided modes. *Nanoscale* **5**, 10582 (2013).

3. Abujetas, D. R., Paniagua-Domíguez, R. & Sanchez-Gil, J. A. Unraveling the janus role of mie resonances and leaky/guided modes in semiconductor nanowire absorption for enhanced light harvesting. *ACS Photonics* **2**, 921 (2015).

4. Leahu *et al*. Evidence of optical circular dichroism in GaAs-based nanowires partially covered with gold. *Adv. Opt. Mater*. **5**, 1601063 (2017).